

**DYNAMIC HEAT CAPACITY OF THE EAST ISING
MODEL**

by

Jonathan Robert Brown

Submitted in Partial Fulfillment
of the Requirements for the Degree of
Master of Science in Mathematics
with Specialization in Industrial Mathematics

New Mexico Institute of Mining and Technology
Socorro, New Mexico
November 20, 2009

ABSTRACT

It has been shown in experiment that the heat capacity of glass formers has a frequency dependence, this is called the dynamic heat capacity. The dynamic heat capacity for a simple spin model known to be a glass former, the east Ising model, is measured by simulation. The result shows stretched exponential decay like relaxation, and the data is fit to the appropriate form. For low temperatures, the relaxation time grows proportionally to exponential inverse temperature squared, which is the theoretical low temperature limit. Another model is applied where the overall relaxation is made up of the relaxations of subdomains that each have their own characteristic times. Using Markov Chains, these times are computed numerically and symbolically, and the model is seen to match the simulations for low temperatures and high frequencies. The dynamics of the east model are tracked very well by this procedure, and we compare this to the parameters of the stretched exponential fits showing that a discrete number of relaxation times can give rise to stretched exponential like behavior.

ACKNOWLEDGMENT

I would like to thank my advisor Dr. Brian Borchers for his help and support on all aspects of this project.

I would also like to thank my committee: Dr. John McCoy for his help on the project and for his help on my defense presentation and Dr. Oleg Makhnin for useful discussions and comments on the manuscript.

Also, I thank my friends and family and especially my parents for their encouragement and support.

This thesis was typeset with L^AT_EX¹ by the author.

¹ L^AT_EX document preparation system was developed by Leslie Lamport as a special version of Donald Knuth's T_EX program for computer typesetting. T_EX is a trademark of the American Mathematical Society. The L^AT_EX macro package for the New Mexico Institute of Mining and Technology thesis format was adapted from Gerald Arnold's modification of the L^AT_EX macro package for The University of Texas at Austin by Khe-Sing The.

TABLE OF CONTENTS

LIST OF FIGURES	vi
1. INTRODUCTION	1
1.1 The Glass Transition	1
1.1.1 Relaxation Time	2
1.2 Linear Response and Relaxation	3
1.2.1 Storage and Loss Moduli	4
1.2.2 Relaxation Models	12
1.2.3 Summary	29
1.3 Dynamic Heat Capacity	31
1.3.1 Experiment	32
1.3.2 Simulation	33
1.4 The East Model	36
1.4.1 Kinetically Constrained Ising Models	37
1.4.2 Definition and Basic Properties	38
1.4.3 Spin Autocorrelation	42
1.4.4 Domains	45
1.4.5 Relaxation Time	48
1.5 Overview of this Work	48

2. METHODOLOGY	50
2.1 Dynamic Heat Capacity Simulation	50
2.1.1 Simulation	50
2.1.2 Dynamic Heat Capacity Computation	51
2.2 Nonlinear Least Squares Fitting Procedure	53
2.2.1 Converting a complex problem to a real one	54
2.2.2 Bounded parameters	56
2.2.3 Multistart	59
2.2.4 Cropped data	59
2.3 Domain Model	59
2.3.1 Markov Chains	60
2.3.2 Markov Chain Multiexponential Model	62
2.3.3 Truncated Markov Chain Multiexponential Model	63
3. RESULTS	65
3.1 Simulation	65
3.2 HN and KWW fits	65
3.3 Markov Chain Model	73
3.3.1 Symbolic Results	73
3.3.2 Numerical Results	75
4. DISCUSSION	87
4.1 Simulation	87
4.2 KWW and HN	87
4.3 Markov Chain	89
4.4 Summary	91

A. RAW SIMULATION DATA	94
Bibliography	109

LIST OF FIGURES

1.1	Contour path used in the proof of the Kramers-Kronig relations. The outer semicircle has radius R which is going to infinity, and the smaller semicircle has radius ϵ which is approaching zero. . .	7
1.2	$\rho(\tau/\tau_{KWW})$ vs. τ/τ_{KWW} for a for a β of 0.9 to 0.1 in 0.1 step increments [54]	15
1.3	Log-log plot of the imaginary part of equation (1.54)	17
1.4	Log-log plots of the real (left) and imaginary (right) parts of a DFT of the KWW function for $\beta = 1, 0.75,$ and 0.5 as labeled. The vertical axes have been normalized to put the maximum of the Debye function at one, and the horizontal axis has been normalized with $\tau = 1.$	18
1.5	Log-log plots of the real (left) and imaginary (right) parts of equation (1.60) with $\tau = 1,$ or equivalently, the horizontal axis is $\omega\tau.$ The solid, dashed, dash-dotted, and dotted lines correspond to $\alpha = 1, 0.75, 0.5,$ and 0.25 respectively.	19
1.6	Log-log plots of the real (left) and imaginary (right) parts of equation (1.61) with $\tau = 1,$ or equivalently, the horizontal axis is $\omega\tau.$ The solid, dashed, dash-dotted, and dotted lines correspond to $\gamma = 1, 0.75, 0.5,$ and 0.25 respectively.	20

1.7	Cole-Cole plots for the HN function with $\alpha = \gamma = 1$ (top left), $\alpha = 0.75$ and $\gamma = 1$ (top right), $\alpha = 1$ and $\gamma = 0.5$ (bottom left), and $\alpha = 0.75$ and $\gamma = 0.5$ (bottom right). The tangent lines are drawn in with angles of $\alpha\gamma\pi/2$ on the left hand side and $\alpha\pi/2$ on the right hand side of each plot.	25
1.8	Cole-Cole plots for the DFT of the normalized KWW function with $\beta = 1, 0.75,$ and 0.5 as labeled.	27
1.9	Sample specific heat capacity spectrum for the bead-spring system. The real part (storage) is on the left, and the imaginary part (loss) is on the right. The top is the full spectrum, and the bottom is a zoom in of the configurational part of the spectrum. The system is at a fixed mean temperature, volume, and number of particles.	34
1.10	Sample energy autocorrelation for the east model. The left plots are for $T = 0.35$ and the right two plots are for $T = 0.2$. The top two plots are log autocorrelation vs. log time. The bottom two are -loglog autocorrelation vs. log time, and on this type of plot a stretched exponential function would be a straight line.	44
2.1	Sample output from an oscillatory experiment on the east model with $T=0.5$ at a period of 1000 MC steps. Top: the input temperature variation. Middle: the raw total energy output. Bottom: the average period of the total energy. The vertical line has been added to emphasize the phase lag between the temperature and energy.	52

2.2	Example specific heat for $T = 0.4$ (left) and $T = 1.0$ (right) against frequency. The real part are the squares and the imaginary part are the circles.	53
2.3	Example data for for $T = 0.4$ (left) and $T = 1.0$ (right), the solid line shows where data was cropped off.	60
3.1	Dynamic heat capacity spectrum from simulation with $T_0 = 0.5$ and $N = 100,000$, where $\Delta T = 0.05T_0$ are squares for storage and inverted triangles for loss and $\Delta T = 0.01T_0$ are diamonds for storage and triangles for loss.	66
3.2	Dynamic heat capacity spectrum from simulation with $T_0 = 0.5$ and $\Delta T = 0.05T_0$, where $N = 100,000$ are squares for storage and inverted triangles for loss, $N = 33,001$ are circles for storage and right triangles for loss, and $N = 10,000$ are diamonds for storage and triangles for loss.	67
3.3	Sample nonlinear regression fits for $T = 0.42$ (left) and $T = 1.0$ (right). The KWW fits are on the top and the HN fits are on the bottom. The plot scale is log-log.	68
3.4	Shifting C_1 and scaling C_2 parameters from the HN fits in units of specific heat against temperature. The inverted triangles are the shift factor, the diamonds are the scale factors, and the squares are the sum of those two. The theoretical specific heat, equation (1.113), is the solid line. Inset: zoomed in on the peak with just the sum and equation (1.113) plotted	69

3.5	Plot of the peak height G_p'' from equation (1.94) in units of specific heat against temperature.	70
3.6	Shape parameters α (inverted triangles), γ (diamonds), and b (squares) plotted against temperature (left) and $\log(\tau)$ from the same type of fit (right) with fitting error bars.	71
3.7	Plot of log relaxation time τ against inverse temperature squared for the KWW fits (squares). The dashed lines are the fits to the EITS form discussed in the text. The solid lines are for comparison to the theoretical slopes of $1/\ln 2$ and $1/2 \ln 2$	72
3.8	Sample Markov chain model (lines) compared to the MC data for $T = 0.2$. The top (squares) is the real part and the middle (inverted triangles) is the imaginary part of the dynamic heat capacity. The bottom is the phase lag δ . The model was computed with τ_d 's for domains with sizes up to $d = 14$	76
3.9	Sample Markov chain model (lines) compared to the MC data for $T = 0.25$. The top (squares) is the real part and the middle (inverted triangles) is the imaginary part of the dynamic heat capacity. The bottom is the phase lag δ . The model was computed with τ_d 's for domains with sizes up to $d = 12$	77
3.10	Sample Markov chain model (lines) compared to the MC data for $T = 0.32$. The top (squares) is the real part and the middle (inverted triangles) is the imaginary part of the dynamic heat capacity. The bottom is the phase lag δ . The model was computed with τ_d 's for domains with sizes up to $d = 16$	78

3.11	Sample Markov chain model (lines) compared to the MC data for $T = 0.42$. The top (squares) is the real part and the middle (inverted triangles) is the imaginary part of the dynamic heat capacity. The bottom is the phase lag δ . The model was computed with τ_d 's for domains with sizes up to $d = 18$	79
3.12	Sample Markov chain model (lines) compared to the MC data for $T = 0.7$. The top (squares) is the real part and the middle (inverted triangles) is the imaginary part of the dynamic heat capacity. The bottom is the phase lag δ . The model was computed with τ_d 's for domains with sizes up to $d = 20$	80
3.13	Sample Markov chain model (lines) compared to the MC data for $T = 1.0$. The top (squares) is the real part and the middle (inverted triangles) is the imaginary part of the dynamic heat capacity. The bottom is the phase lag δ . The model was computed with τ_d 's for domains with sizes up to $d = 14$	81
3.14	Sample truncated Markov chain model (lines) compared to the MC data for $T = 0.42$ with $d_{\max} = 18$. The top (squares) is the real part and the middle (inverted triangles) is the imaginary part of the dynamic heat capacity. The bottom is the phase lag δ .	83
3.15	Sample truncated Markov chain model (lines) compared to the MC data for $T = 0.42$ with $d_{\max} = 8$. The top (squares) is the real part and the middle (inverted triangles) is the imaginary part of the dynamic heat capacity. The bottom is the phase lag δ .	84

3.16	Sample truncated Markov chain model (lines) compared to the MC data for $T = 0.42$ with $d_{\max} = 5$. The top (squares) is the real part and the middle (inverted triangles) is the imaginary part of the dynamic heat capacity. The bottom is the phase lag δ .	85
3.17	Plot of domain length vs. temperature. The squares are the best fit d_{\max} . The dotted line is the mean domain length.	86
A.1	C'_V (squares), C''_V (circles), and δ (points) from simulations at the marked temperatures.	95
A.2	C'_V (squares), C''_V (circles), and δ (points) from simulations at the marked temperatures.	96
A.3	C'_V (squares), C''_V (circles), and δ (points) from simulations at the marked temperatures.	97
A.4	C'_V (squares), C''_V (circles), and δ (points) from simulations at the marked temperatures.	98
A.5	C'_V (squares), C''_V (circles), and δ (points) from simulations at the marked temperatures.	99
A.6	C'_V (squares), C''_V (circles), and δ (points) from simulations at the marked temperatures.	100
A.7	C'_V (squares), C''_V (circles), and δ (points) from simulations at the marked temperatures.	101
A.8	C'_V (squares), C''_V (circles), and δ (points) from simulations at the marked temperatures.	102

A.9	C'_V (squares), C''_V (circles), and δ (points) from simulations at the marked temperatures.	103
A.10	C'_V (squares), C''_V (circles), and δ (points) from simulations at the marked temperatures.	104
A.11	C'_V (squares), C''_V (circles), and δ (points) from simulations at the marked temperatures.	105
A.12	C'_V (squares), C''_V (circles), and δ (points) from simulations at the marked temperatures.	106
A.13	C'_V (squares), C''_V (circles), and δ (points) from simulations at the marked temperatures.	107
A.14	C'_V (squares), C''_V (circles), and δ (points) from simulations at the marked temperature.	108

This thesis is accepted on behalf of the faculty of the Institute by the following committee:

Brian Borchers, Advisor

Jonathan Robert Brown

Date

CHAPTER 1

INTRODUCTION

1.1 The Glass Transition

Amorphous solids (specifically, glasses and polymers) have complicated viscoelastic properties, meaning that they act like both solids and liquids. For temperatures and timescales above their glass transition, they bend and reform shape without readily fracturing. This is because these materials can be viewed as a liquid with very high viscosity, so they flow very slowly. At the glass transition, the amount of time required for the material to flow outlasts the patience of the experimenter - that is, it takes too long for the material to relax into equilibrium.

One way of observing the glass transition is to track the heat capacity with temperature. The heat capacity typically drops off as temperature approaches the glass transition. This is because the material is unable to rearrange itself in experimental time to react to the change of heat or temperature. This type of experiment is called differential scanning calorimetry (DSC).

With the dynamic heat capacity one can track how long the relaxations take. The long time reconfigurations of the system are often called α -processes, and the short time collisions of the atoms are called β -processes [49]. On timescales shorter than that of the α -processes, the material is glassy, so when the timescale of an α -process becomes extremely long, the material is

considered a glass.

A subject of considerable debate is whether the timescale of the α -process, or relaxation time (commonly denoted τ), diverges to infinity at a nonzero temperature. If it does, then the glass transition is a true phase transition, and there are some good reasons for thinking it might be (e.g. the Kauzmann paradox [34]). Alternatively, τ could simply be diverging at absolute zero, but diverging very quickly so that the relaxation time is larger than is measurable.

1.1.1 Relaxation Time

There are a few standard models that are used to relate the relaxation time τ to the temperature T . The most basic one, and most commonly used to fit β -processes, is the Arrhenius law. Namely, treating it as an activated process: in order for the material to rearrange itself, it must go over some type of energy barrier.

$$\tau_{\text{Arrhenius}}(T) = \tau_0 \exp\left(\frac{B}{T}\right) \quad (1.1)$$

where τ_0 and B are fitting parameters, and τ diverges at absolute zero.

A non-Arrhenius form, which has a divergence at a critical temperature T_c is the Vogel-Fulcher-Tammann law [49], given by

$$\tau_{\text{Vogel}}(T) = \tau_0 \exp\left(\frac{B}{T - T_c}\right) \quad (1.2)$$

This is just a shifted form of equation (1.1) to put in a phase transition at a nonzero critical temperature.

An alternative non-Arrhenius form that has no divergence at nonzero temperature but has a faster increase of τ with lowering temperature is the exponential inverse temperature squared (EITS) form [14]. This is given by

$$\tau_{\text{EITS}}(T) = \tau_0 \exp\left(\frac{B}{T^2}\right) \quad (1.3)$$

Since all these forms have relaxation time growing very quickly with decreasing temperature, it is nearly impossible to tell the difference between them with experimental or simulation data. One of the advantages of the east model that we'll see later is that its τ is exactly solvable, and actually follows equation (1.3) EITS.

1.2 Linear Response and Relaxation

In the study of amorphous solids one can look at the dynamics of a system by perturbing it with a mechanical, electromagnetic, or thermodynamic sinusoidal force and observing how the system responds. Using Fourier theory, we can relate the dynamics to relaxation behavior in the time domain.

A common result is to get one or more peaks in the frequency domain data that correspond to exponential-like behavior in the time domain. Each describes a separate relaxation process, and when multiple peaks are observed, it is commonly interpreted as cooperative behavior decoupling from collision behavior. The cooperative behavior is what makes a viscoelastic material soft, so understanding these dynamics gives an idea of how the material acts on a macroscopic level.

This section will first discuss the general theory of the dynamic modulus and how it relates to the time domain, then move on to models commonly

used in the literature.

1.2.1 Storage and Loss Moduli

The storage and loss moduli are quantities used in the study of the dynamics of amorphous materials. There are, in general, mechanical, electromagnetic, and thermodynamic quantities that can be studied this way [36]. The basic idea is to perturb the material with some sort of sinusoidal driving force, and measure its reaction.

Definition

Let x be the driving “force”, the input. So, $x(t)$ takes the form

$$x(t) = A \sin(\omega t) \tag{1.4}$$

where ω is the frequency and A is the amplitude of the driving force. In order to be in the linear response regime, we choose the forcing amplitude A to be small enough (exactly how small depends on the application). Then, since we’re assuming linearity, the output (of whatever quantity we want to look at) is also sinusoidal, but perhaps phase shifted. That is, we measure the output $y(t)$ as

$$y(t) = B \sin(\omega t + \delta) \tag{1.5}$$

Since we’re assuming that this is a real system, it must be causal, so $\delta \geq 0$. Also, since we’re assuming linearity, the amplitude of the output, B , varies linearly with the amplitude of the input, A , and if A is zero, B must also be zero. In general, B and δ can depend on the frequency of the input signal ω ,

so equation (1.5) is really

$$y(t) = A\gamma(\omega) \sin(\omega t + \delta(\omega)) \quad (1.6)$$

where $A\gamma(\omega) \equiv B(\omega)$

From Fourier analysis, we know that the response of a linear system is the convolution of the input function and the impulse response of the system. Let $g(t)$ be the impulse response with Fourier transform $G(\omega)$. $G(\omega)$ in this context is called the dynamic modulus. Since we're considering a physical system, g must be a real valued function, and by using equation (1.4) the response constructed in this way gives

$$y(t) = x(t) * g(t) \quad (1.7)$$

$$= A \sin(\omega t) * g(t) \quad (1.8)$$

$$= A \int_{-\infty}^{\infty} g(\tau) \sin(\omega(t - \tau)) d\tau \quad (1.9)$$

$$= A \int_{-\infty}^{\infty} g(\tau) \Im \{ e^{i\omega(t-\tau)} \} d\tau \quad (1.10)$$

$$= A \Im \left\{ \int_{-\infty}^{\infty} g(\tau) e^{i\omega(t-\tau)} d\tau \right\} \quad (1.11)$$

$$= A \Im \left\{ e^{i\omega t} \int_{-\infty}^{\infty} g(\tau) e^{-i\omega\tau} d\tau \right\} \quad (1.12)$$

$$= A \Im \{ e^{i\omega t} G(\omega) \} \quad (1.13)$$

G is generally a complex valued function, so let $G(\omega) = G'(\omega) + iG''(\omega) = R(\omega)e^{i\phi(\omega)}$. Then,

$$y(t) = AR(\omega) \Im \{ e^{i(\omega t + \phi(\omega))} \} \quad (1.14)$$

or

$$y(t) = AR(\omega) \sin(\omega t + \phi(\omega)) \quad (1.15)$$

Equations (1.6) and (1.15) must be the same, so

$$R(\omega) = \gamma(\omega) \quad (1.16)$$

and

$$\phi(\omega) = \delta(\omega) \quad (1.17)$$

So, the dynamic modulus, in terms of the induced forcing function and observed response above, is

$$G^*(\omega) = \gamma(\omega) \cos(\delta(\omega)) + i\gamma(\omega) \sin(\delta(\omega)) \quad (1.18)$$

The real part of this is referred to as the storage because it quantifies how much the output signal is in phase with the input signal, i.e.

$$G'(\omega) = \gamma(\omega) \cos(\delta(\omega)) \quad (1.19)$$

Similarly, the imaginary part is called the loss, i.e.

$$G''(\omega) = \gamma(\omega) \sin(\delta(\omega)) \quad (1.20)$$

The dynamic modulus is often denoted with a * to indicate a complex value (not a complex conjugate) [15].

Kramers-Kronig Relations

As an aside that will be important later, if we have a complex valued function $F(z) = F_{re}(z) + iF_{im}(z)$, $z \in \mathbb{C}$, that is analytic in the upper half of the z -plane and such that $\lim_{|z| \rightarrow \infty} f(z) = 0$, then there is a relationship between the real and imaginary parts of the function given by

$$F_{re}(x) = \frac{1}{\pi} \int_{-\infty}^{\infty} \frac{F_{im}(\xi)}{\xi - x} d\xi \quad (1.21)$$

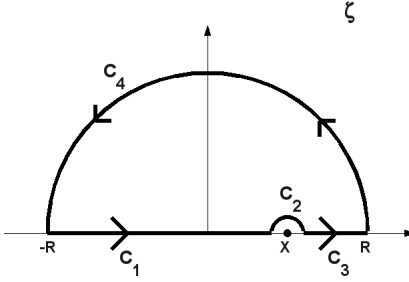


Figure 1.1: Contour path used in the proof of the Kramers-Kronig relations. The outer semicircle has radius R which is going to infinity, and the smaller semicircle has radius ϵ which is approaching zero.

$$F_{\text{im}}(x) = -\frac{1}{\pi} \mathcal{P} \int_{-\infty}^{\infty} \frac{F_{\text{re}}(\xi)}{\xi - x} d\xi \quad (1.22)$$

where $x \in \mathbb{R}$, and the integrals are taken in principal value. These are the Kramers-Kronig relations [37]. We can prove this using contour integration.

Proof. To get the above integral we consider integrating the function $F(\zeta)/(\zeta - x)$ on the contour C shown in figure 1.1 with $C = C_1 \cup C_2 \cup C_3 \cup C_4$, as $R \rightarrow \infty$ and the radius of the smaller inner circle $\epsilon \rightarrow 0$. Since the function is analytic in the upper half plane, this contour avoids the only pole at x , so by Cauchy's integral theorem from complex analysis we have

$$\int_C \frac{F(\zeta)}{\zeta - x} d\zeta = 0 \quad (1.23)$$

Splitting the integral into the four subsections from Figure 1.1, this is

$$\int_{C_1} \frac{F(\zeta)}{\zeta - x} d\zeta + \int_{C_2} \frac{F(\zeta)}{\zeta - x} d\zeta + \int_{C_3} \frac{F(\zeta)}{\zeta - x} d\zeta + \int_{C_4} \frac{F(\zeta)}{\zeta - x} d\zeta = 0 \quad (1.24)$$

The large semicircle part of this, C_4 , can be evaluated by using the substitution $\zeta = Re^{i\theta}$,

$$\int_{C_4} \frac{F(\zeta)}{\zeta - x} d\zeta = \int_0^\pi \frac{iRe^{i\theta}}{Re^{i\theta} - x} F(Re^{i\theta}) d\theta \quad (1.25)$$

Therefore,

$$\left| \int_{C_4} \frac{F(\zeta)}{\zeta - x} d\zeta \right| \leq \int_0^\pi \left| \frac{Re^{i\theta}}{Re^{i\theta} - x} \right| |F(Re^{i\theta})| d\theta \quad (1.26)$$

$$= \int_0^\pi \left| \frac{1}{1 - \frac{x}{R \exp(i\theta)}} \right| |F(Re^{i\theta})| d\theta \quad (1.27)$$

$$\xrightarrow{R \rightarrow \infty} 0 \quad (1.28)$$

this follows from the assumption that $\lim_{|z| \rightarrow \infty} F(z) = 0$.

We can do a similar substitution for the smaller semicircle. Let $\zeta = x + \epsilon e^{i\theta}$ so $d\zeta = i\epsilon e^{i\theta} d\theta$, then the second integral in equation (1.24) is evaluated,

$$\int_{C_2} \frac{F(\zeta)}{\zeta - x} d\zeta = \int_\pi^0 \frac{i\epsilon e^{i\theta}}{x + \epsilon e^{i\theta} - x} F(x + \epsilon e^{i\theta}) d\theta \quad (1.29)$$

$$= -i \int_0^\pi F(x + \epsilon e^{i\theta}) d\theta \quad (1.30)$$

$$\xrightarrow{\epsilon \rightarrow 0} -i\pi F(x) \quad (1.31)$$

which follows from F being analytic at x .

The two remaining terms of equation (1.24) are simplified by the substitution $\zeta = \xi$, $\xi \in \mathbb{R}$. That is,

$$\int_{C_1} \frac{F(\zeta)}{\zeta - x} d\zeta + \int_{C_3} \frac{F(\zeta)}{\zeta - x} d\zeta = \int_{-R}^{x-\epsilon} \frac{F(\xi)}{\xi - x} d\xi + \int_{x+\epsilon}^R \frac{F(\xi)}{\xi - x} d\xi \quad (1.32)$$

Since we're letting $\epsilon \rightarrow 0$, we can combine these into a single integral from $-R$ to R , but we are approaching the pole symmetrically from both sides, so this is actually the Cauchy principal value. We also let $R \rightarrow \infty$, meaning that the bounds of the combined integral approach $\pm\infty$; these symmetries both ensure the convergence of the integral but only in the principal value.

That is,

$$\int_{C_1} \frac{F(\zeta)}{\zeta - x} d\zeta + \int_{C_3} \frac{F(\zeta)}{\zeta - x} d\zeta \xrightarrow[R \rightarrow \infty]{\epsilon \rightarrow 0} \int_{-\infty}^{\infty} \frac{F(\xi)}{\xi - x} d\xi \quad (1.33)$$

Therefore, equation (1.24) simplifies to

$$\int_{-\infty}^{\infty} \frac{F(\xi)}{\xi - x} d\xi = i\pi F(x) \quad (1.34)$$

The imaginary part of equation (1.34) is equation (1.21) and the real part is equation (1.22). \square

Toll [55] showed that in any causal linear system the frequency domain output function is analytic in the upper half of the ω -plane, and since causality must hold true for any real signal, we can therefore readily apply equations (1.21) and (1.22) to any physical system. The consequence of this is that the dynamic modulus $G^*(\omega)$ is determined entirely by either one of its real or imaginary parts alone.

Transforming from the Time Domain

The impulse response of the system is something that is difficult to measure. A more physically significant and easier to measure function is a relaxation function, i.e. how the system moves into equilibrium from a non-equilibrium state. This is the (negative) step response of the system, where we “push” on the system in some way out of equilibrium at time $t = 0$ and watch what it does. Assuming an input of $x(t) = -u(t)$ a negative unit step function, the step response f and the impulse response g are related by

$$f(t) = g(t) * (-u(t)) = - \int_{-\infty}^{\infty} g(\tau) u(t - \tau) d\tau = - \int_{-\infty}^t g(\tau) d\tau \quad (1.35)$$

Taking the derivative, we have the impulse response in terms of the more easily measurable step response:

$$g(t) = - \frac{df(t)}{dt} \quad (1.36)$$

Of course we are assuming that a real system's impulse response is causal, so $f(t)$ is zero for $t < 0$. So, to move into the frequency domain from a relaxation function we plug equation (1.36) into $G^*(\omega) = \mathcal{F}(g(t))$

$$G^*(\omega) = \int_0^\infty -\frac{df}{dt} e^{-i\omega t} dt \quad (1.37)$$

This is a one sided Fourier transform, or equivalently, a pure imaginary Laplace transform [39]. The inverse transform is [36]

$$\frac{df(t)}{dt} = \frac{1}{2\pi} \int_0^\infty (G^*(\omega) - G_\infty) e^{i\omega t} d\omega \quad (1.38)$$

Applications

In the derivation of the dynamic modulus and the related time domain relaxation function, the input and output were left generic. In general, there are mechanical, electromagnetic, and thermodynamic applications of this theory. The different applications can result in somewhat different results even on the same material, but they all are ways to investigate fundamentally the same dynamics.

Mechanical One way to characterize a viscoelastic material is to consider how it reacts to strain, or deformation. If a strain is applied to a solid, the solid will “push back”. Whereas, if a strain is applied to a perfect Newtonian liquid, it will simply flow, not pushing back. So, if the strain is applied sinusoidally, the stress, or force per unit area, from the solid will be in phase, but with a liquid the stress does not start to kick in until you try to reverse the flow, so the stress will then be out of phase with the strain. For viscoelastic materials,

the behavior is somewhere in between, and it depends on the frequency [15]. How close it is to being solid-like is quantified by the storage modulus, and how much it is liquid-like is quantified by the loss modulus.

This can be done with a shear instead of a strain or a pressure variation resulting in a shear or compression modulus, respectively, with a similar meaning [36].

Electromagnetic When an electric field is applied to a dielectric material, poles in the material feel a torque to align with that field. By applying a sinusoidally varying electric field and looking at the polarization, the analogous dynamic modulus is the complex dielectric susceptibility, which is related linearly to the permittivity [36]. Unfortunately, there is also a dielectric modulus, which is the multiplicative inverse of the permittivity, but the dielectric modulus is not directly analogous to the dynamic modulus defined above [33]. The lag (if any) of the polarization relative to the electric field is due to individual dipoles in the material not being able to move freely because they are crowded together.

The magnetic analogy is to induce a magnetic field and look at the magnetization of the material to measure the analogous quantity: magnetic susceptibility, which is then linearly related to the magnetic permeability [36].

Thermodynamic The application that is the focus here, dynamic heat capacity, was first invented independently by Birge and Nagel [5] and by Christensen [10]. The driving function is temperature (or energy), and we are looking for response in the total energy (temperature) of the system. In this case, if ΔT

is the amplitude of the temperature, and ΔE is the amplitude of the energy, then $\frac{B}{A} = \frac{\Delta E}{\Delta T}$, i.e. how much energy changes per unit change in temperature. This is the heat capacity, and the complex modulus is a frequency dependent heat capacity. Experimentally, what is actually measured is the temperature of the system with a sinusoidally varying heater, but it is more natural in simulation to vary the temperature because it is more easily controlled [5,21]. The next major section has further details about the dynamic heat capacity.

1.2.2 Relaxation Models

Time Domain Relaxation

The simplest model for relaxation was proposed by Peter Debye in 1912. He was working on dielectric relaxation, and in his ideal model of spherical non-interacting molecules in a viscous medium predicted that the rate of depolarization was proportional to the polarization [27,41,39]. In the general notation used above, this is

$$\frac{df}{dt} = -\frac{f - f_\infty}{\tau} \quad (1.39)$$

This differential equation has the solution

$$f(t) = f_0 e^{-t/\tau} + f_\infty \quad (1.40)$$

Where f_0 is the initial state of the system, f_∞ is the equilibrium state, and τ is the single characteristic decay time.

The parameters f_0 and f_∞ do not tell us anything about the decay function itself, only the initial and final states, which is a separate issue. So, it is common to leave these parameters off in the analysis of decay functions and

consider rather the normalized decay function [2]. The normalized version of equation (1.40) is

$$f_n(t) = e^{-t/\tau} \quad (1.41)$$

However, a single exponential quickly fails to work for more complicated systems.

Multiple exponential An easy extension of equation (1.41) is to assume that there are multiple Debye processes occurring in the material. If there are two, the relaxation function is

$$f_n(t) = B_1 e^{-t/\tau_1} + B_2 e^{-t/\tau_2} \quad (1.42)$$

We now have two decay times, τ_1 and τ_2 each from a different Debye process. Again, I've removed the initial condition parameter, so $B_1 + B_2 = 1$ making B_1 and B_2 the relative “strengths” or distribution of the relaxation times τ_1 and τ_2 , respectively.

Generalizing on this idea further, if we want to study something that has multiple simultaneous relaxations, we add as many exponential functions as needed to fit the data. That is,

$$f_n(t) = \sum_{n=1}^N B_n e^{-t/\tau_n} \quad (1.43)$$

In this case we have a discrete distribution of relaxation times τ_n . The B 's have a similar meaning to above. This gives a very good fit to data where you'd expect the complexity of the system to result in multiple relaxations. For example, for a glass under strain you might expect multiple relaxation times

from the different molecule components of the material, i.e. small molecules can more easily rearrange themselves than larger ones. The problem with this approach is that there are simply too many parameters; it is so general with many terms that it becomes meaningless.

Kohlrausch-Williams-Watts An alternative generalization of simple exponential decay is the stretched exponential decay function.

$$f_n(t) = e^{-(t/\tau_{KWW})^\beta} \quad (1.44)$$

where once again, τ_{KWW} is a characteristic decay time, and β is a parameter between zero and one. This equation was first studied in 1854 by Rudolf Kohlrausch to describe the discharge of a Leiden jar [35] and was later used by Williams and Watts to describe decay of a dielectric [56], so it is often referred to as the Kohlrausch-Williams-Watts or KWW function. It is a popular function because it fits a wide variety of relaxation data with very few parameters.

Distribution of Relaxation Times

It is now instructive to define the notion of a distribution of relaxation times. We've already seen the discrete version of this, but it is also possible to define a continuous distribution of relaxation times to describe the KWW function, for example, as a superposition of Debye processes [39, 2].

$$f_n(t) = \int_0^\infty e^{-t/\tau} \rho(\tau) d\tau \quad (1.45)$$

Lindsey and Patterson [39] showed that by plugging the KWW function (1.44) into (1.45),

$$e^{-(t/\tau_{KWW})^\beta} = \int_0^\infty e^{-t/\tau} \rho(\tau) d\tau \quad (1.46)$$

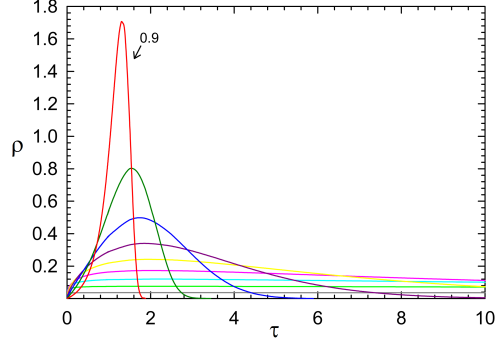


Figure 1.2: $\rho(\tau/\tau_{KWW})$ vs. τ/τ_{KWW} for a for a β of 0.9 to 0.1 in 0.1 step increments [54]

we get

$$\rho(\tau) = -\frac{\tau_{KWW}}{\pi\tau^2} \sum_{k=0}^{\infty} \frac{(-1)^k}{k!} \sin(k\pi\beta)\Gamma(k\beta + 1) \left(\frac{\tau}{\tau_{KWW}}\right)^{k\beta+1} \quad (1.47)$$

In the limit that β goes to one, this function approaches the delta function, and as β goes to zero $\rho(\tau)$ spreads out, that is covering more varieties of relaxation times. See Figure 1.2. Therefore β is interpreted as a measure of the spread of relaxation times are occurring for a given data set, which characterizes the system in question. In terms of molecular dynamics, the different relaxation times are attributed to the time it takes for molecules to hit each other and move past each other in different ways (that is different shapes and sizes of molecules and translational vs. rotational movement all have an effect) [20].

Frequency Domain Relaxation

Debye Relaxation The simplest form of relaxation, a Debye process, can be moved into the frequency domain plugging (1.41) into (1.37)

$$G^*(\omega) = \int_0^\infty -\left(-\frac{1}{\tau}e^{-t/\tau}\right) dt \quad (1.48)$$

$$= \frac{1}{\tau} \int_0^\infty e^{-i\omega t - t/\tau} dt \quad (1.49)$$

$$= -\frac{e^{-i\omega t - t/\tau}}{\tau(i\omega + 1/\tau)} \Big|_0^\infty \quad (1.50)$$

$$= \frac{1}{1 + i\omega\tau} \quad (1.51)$$

If we had used equation (1.40) instead the f_0 term would have just carried through the transform, adding a scaling parameter to the result. Also, since the full dynamic modulus might be the superposition of multiple behaviors, we can also add a shifting parameter (that would have to be subtracted off to transform into the time domain). The resulting general frequency domain Debye function is

$$G^*(\omega) = G_\infty + \frac{G_0 - G_\infty}{1 + i\omega\tau} \quad (1.52)$$

But again, those parameters are not important to the shape of the decay function, so a normalized decay function is often constructed:

$$G_n^*(\omega) = \frac{G^*(\omega) - G_\infty}{G_0 - G_\infty} \quad (1.53)$$

which gives the normalized Debye function

$$G_{\text{Debye}}^*(\omega) = \frac{1}{1 + i\omega\tau} \quad (1.54)$$

For the rest of this section I will use the notation G_{name}^* to denote the normalized version of the frequency domain relaxation function for convenience. Of course,

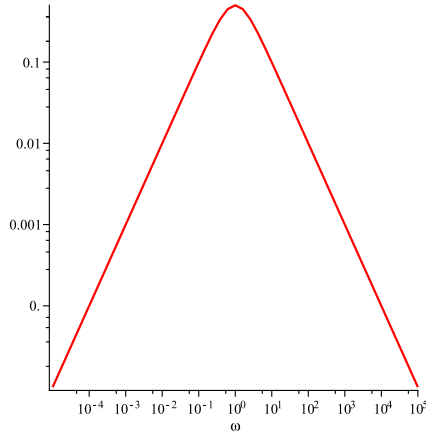


Figure 1.3: Log-log plot of the imaginary part of equation (1.54) with $\tau = 1$, or equivalently, the horizontal axis is $\omega\tau$.

in practice, we have to add the G_0 and G_∞ parameters back in to actually fit to these functions, but they are not relevant to the discussion at this point.

The normalized Debye function is easily split into real and imaginary parts

$$G'_{\text{Debye}}(\omega) = \frac{1}{1 + (\omega\tau)^2} \quad (1.55)$$

$$G''_{\text{Debye}}(\omega) = \frac{\omega\tau}{1 + (\omega\tau)^2} \quad (1.56)$$

Also, it's easily seen by using (1.37) that the frequency domain version of the distribution of Debye processes (1.45) is [2]

$$G^*(\omega) = \int_{-\infty}^{\infty} \frac{\tau\rho(\tau)}{1 + i\omega\tau} d\tau \quad (1.57)$$

As seen in figure 1.3, the log-log plot of Debye relaxation is symmetric with a slope of one on each side of the peak.

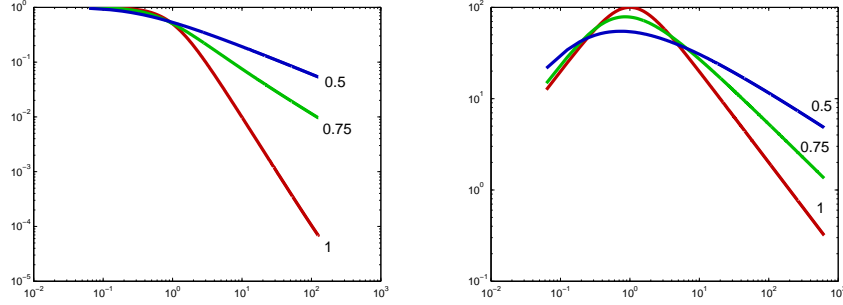


Figure 1.4: Log-log plots of the real (left) and imaginary (right) parts of a DFT of the KWW function for $\beta = 1, 0.75,$ and 0.5 as labeled. The vertical axes have been normalized to put the maximum of the Debye function at one, and the horizontal axis has been normalized with $\tau = 1$.

von Schweidler Law Near the turn of the century von Schweidler discovered that for the frequency band $\omega \gg 1/\tau$ relaxation functions follow the law [20]

$$G'_{vS}(\omega) = \frac{\cos(b_{vS}\frac{\pi}{2})\Gamma(1 + b_v S)}{(\omega\tau)^{b_{vS}}} \quad (1.58)$$

$$G''_{vS}(\omega) = \frac{\sin(b_{vS}\frac{\pi}{2})\Gamma(1 + b_v S)}{(\omega\tau)^{b_{vS}}} \quad (1.59)$$

where $0 < b_{vS} \leq 1$. Plotting the imaginary part on a log-log scale gives a constant slope of $-b_{vS}$. This gives the general high frequency non-Debye relaxation behavior.

Frequency Domain KWW As stated above, the KWW function (1.44) does not have a analytic Fourier transform, but we can estimate it by discretizing the function and taking the discrete Fourier transform. The log-log slopes on the imaginary peak are no longer symmetric, the low frequency side remains about one, but the high frequency side has a slope of $-\beta$ (see Figure 1.4).

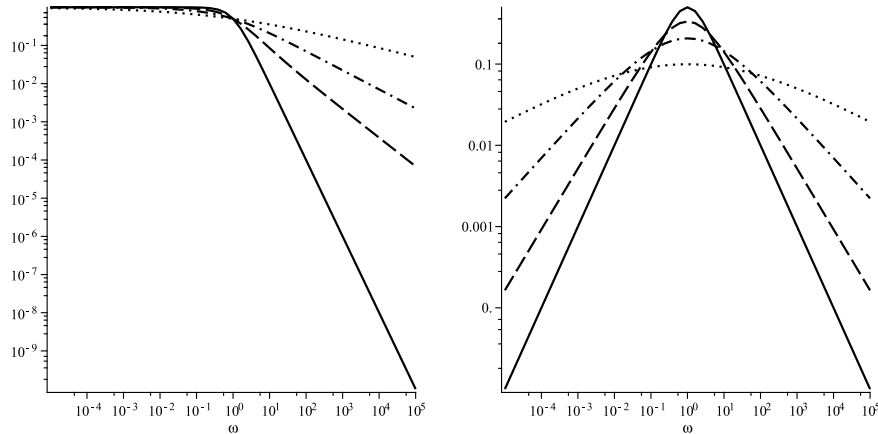


Figure 1.5: Log-log plots of the real (left) and imaginary (right) parts of equation (1.60) with $\tau = 1$, or equivalently, the horizontal axis is $\omega\tau$. The solid, dashed, dash-dotted, and dotted lines correspond to $\alpha = 1, 0.75, 0.5,$ and 0.25 respectively.

Generalizations of the Debye Model

In the applications described above, the simple symmetry and slope of Debye relaxation are not observed in experimental data, and a considerable amount of work has been done trying to generalize equation (1.54) with as few parameters as possible to fit experimental data [12, 11, 24, 18]. The KWW function has no analytical Fourier transform but fits to time-domain data very well and has a physically meaningful parameters τ_{KWW} and β . These generalizations of the Debye relaxation are often approximations of the DFT of the KWW function, and their parameters are related to τ_{KWW} and β [2, 56, 39, 20]

In 1941, K.S. Cole and R.H. Cole proposed the following generalization of equation (1.54) to describe the dielectric properties of various materi-

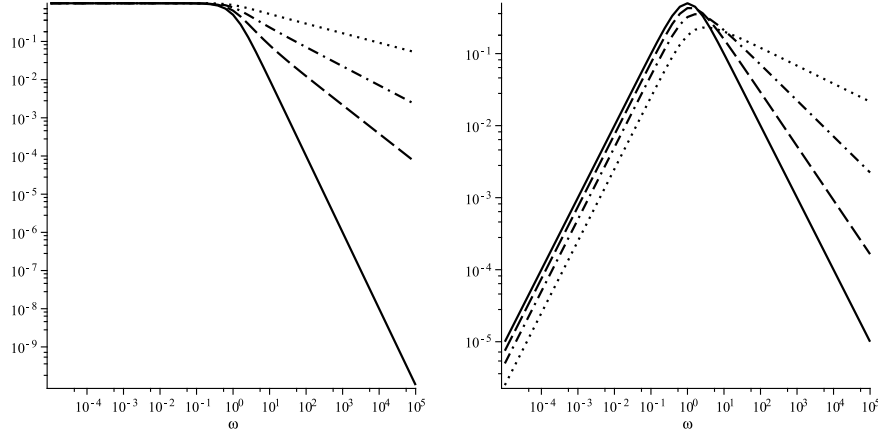


Figure 1.6: Log-log plots of the real (left) and imaginary (right) parts of equation (1.61) with $\tau = 1$, or equivalently, the horizontal axis is $\omega\tau$. The solid, dashed, dash-dotted, and dotted lines correspond to $\gamma = 1, 0.75, 0.5,$ and 0.25 respectively.

als [11]

$$G_{CC}^*(\omega) = \frac{1}{1 + (i\omega\tau)^\alpha} \quad (1.60)$$

where $0 < \alpha \leq 1$. This creates a wider imaginary peak (see Figure 1.5). In the literature, it is often referred to as the Cole-Cole (CC) function.

Ten years later, D.W. Davidson and R.H. Cole proposed an alternative generalization, also to describe dielectric relaxation, as follows [12]

$$G_{CD}^*(\omega) = \frac{1}{(1 + i\omega\tau)^\gamma} \quad (1.61)$$

where $0 < \gamma \leq 1$. This equation has an asymmetric peak in the imaginary part (see Figure 1.6). In the literature, it is often referred to as the Cole-Davidson (CD) function.

Combining equations (1.60) and (1.61), Havriliak and Negami used

used the following equation to describe dielectric and mechanical relaxation [24]

$$G_{\text{HN}}^*(\omega) = \frac{1}{(1 + (i\omega\tau)^\alpha)^\gamma} \quad (1.62)$$

where α and γ are defined as above. In the literature, it is often referred to as the Havriliak-Negami (HN) function. α and γ are shape parameters with γ being a symmetry parameter and α a spreading parameter. The Debye, CC, and CD functions are all special cases of the HN function, by setting one or both of the parameters to one. The HN equation is more general, and in some cases can provide a better fit, but at the cost of an additional parameter.

It can be shown that the associated distribution of relaxation times is [2]

$$\rho(\tau') = \frac{1}{\pi} \frac{(\tau'/\tau)^{\alpha\gamma} \sin(\gamma\psi)}{(1 + 2(\tau'/\tau)^\alpha \cos(\alpha\pi) + (\tau'/\tau)^{2\alpha})^{\gamma/2}} \quad (1.63)$$

with

$$\psi = \arctan \left| \frac{\sin(\alpha\pi)}{(\tau'/\tau)^\alpha + \cos(\alpha\pi)} \right| \quad (1.64)$$

For the CD function, this simplifies to [39]

$$\rho(\tau') = \begin{cases} \frac{\sin(\gamma\pi)}{\pi\tau'} \left(\frac{\tau'}{\tau-\tau'}\right)^\gamma & , \quad \tau' < \tau \\ \infty & , \quad \text{otherwise} \end{cases} \quad (1.65)$$

In practice, we need the real and imaginary parts of equation (1.62).

First, we want to express the denominator as a complex exponential.

$$1 + (i\omega\tau)^\alpha = 1 + e^{i\alpha\pi/2} (\omega\tau)^\alpha \quad (1.66)$$

$$= 1 + (\omega\tau)^\alpha \cos\left(\alpha\frac{\pi}{2}\right) + i(\omega\tau)^\alpha \sin\left(\alpha\frac{\pi}{2}\right) \quad (1.67)$$

$$= \sqrt{\left(1 + (\omega\tau)^\alpha \cos\left(\alpha\frac{\pi}{2}\right)\right)^2 + \left((\omega\tau)^\alpha \sin\left(\alpha\frac{\pi}{2}\right)\right)^2} \\ \times \exp\left(i \arctan\left(\frac{(\omega\tau)^\alpha \sin(\alpha\pi/2)}{1 + (\omega\tau)^\alpha \cos(\alpha\pi/2)}\right)\right) \quad (1.68)$$

or

$$1 + (i\omega\tau)^\alpha = \left(1 + 2(\omega\tau)^\alpha \cos\left(\alpha\frac{\pi}{2}\right) + (\omega\tau)^{2\alpha}\right)^{1/2} e^{i\theta_{\text{HN}}} \quad (1.69)$$

where

$$\theta_{\text{HN}} = \arctan\left(\frac{(\omega\tau)^\alpha \sin(\alpha\pi/2)}{1 + (\omega\tau)^\alpha \cos(\alpha\pi/2)}\right) \quad (1.70)$$

substituting (1.69) and (1.70) into (1.62) gives

$$G_{\text{HN}}^*(\omega) = \left(1 + 2(\omega\tau)^\alpha \cos\left(\alpha\frac{\pi}{2}\right) + (\omega\tau)^{2\alpha}\right)^{-\gamma/2} e^{-i\gamma\theta_{\text{HN}}} \quad (1.71)$$

which is easily split into real and imaginary parts

$$G'_{\text{HN}}(\omega) = \frac{\cos(\gamma\theta_{\text{HN}})}{\left(1 + 2(\omega\tau)^\alpha \cos\left(\alpha\frac{\pi}{2}\right) + (\omega\tau)^{2\alpha}\right)^{\gamma/2}} \quad (1.72)$$

$$G''_{\text{HN}}(\omega) = \frac{\sin(\gamma\theta_{\text{HN}})}{\left(1 + 2(\omega\tau)^\alpha \cos\left(\alpha\frac{\pi}{2}\right) + (\omega\tau)^{2\alpha}\right)^{\gamma/2}} \quad (1.73)$$

The Cole-Cole ($\gamma = 1$) version of this is easily derived from equations (1.60) and (1.67)

$$G'_{\text{CC}}(\omega) = \frac{1 + (\omega\tau)^\alpha \cos\left(\alpha\frac{\pi}{2}\right)}{1 + 2(\omega\tau)^\alpha \cos\left(\alpha\frac{\pi}{2}\right) + (\omega\tau)^{2\alpha}} \quad (1.74)$$

$$G''_{\text{CC}}(\omega) = \frac{(\omega\tau)^\alpha \sin\left(\alpha\frac{\pi}{2}\right)}{1 + 2(\omega\tau)^\alpha \cos\left(\alpha\frac{\pi}{2}\right) + (\omega\tau)^{2\alpha}} \quad (1.75)$$

The Cole-Davidson ($\alpha = 1$) equation has a simple form. First, θ simplifies to

$$\theta_{\text{CD}} = \arctan(\omega\tau) \quad (1.76)$$

So, equation (1.71) becomes

$$G_{\text{CD}}^*(\omega) = \left(1 + \tan^2(\theta_{\text{CD}})\right)^{-\gamma/2} e^{-i\gamma\theta_{\text{CD}}} \quad (1.77)$$

$$= \cos^\gamma(\theta_{\text{CD}}) e^{-i\gamma\theta_{\text{CD}}} \quad (1.78)$$

which has real and imaginary parts

$$G'_{\text{CD}}(\omega) = \cos^\gamma(\theta_{\text{CD}}) \cos(\gamma\theta_{\text{CD}}) \quad (1.79)$$

$$G''_{\text{CD}}(\omega) = \cos^\gamma(\theta_{\text{CD}}) \sin(\gamma\theta_{\text{CD}}) \quad (1.80)$$

Cole-Cole Plots Also in their 1941 paper, K.S. Cole and R.H. Cole introduced a method of visualizing and fitting data that doesn't make an explicit assumption as to which model is being used [11, 36]. By plotting the real part of the dynamic modulus against the imaginary part, we can take advantage of the common terms in the above equations and cancel them out in high and low frequency limits. These are so-called Cole-Cole plots [36]. Of course, we have to assume we're in a frequency band where there is only one imaginary peak. For high frequencies $\omega \gg 1/\tau$, $G'_{\text{HN}}(\omega) \rightarrow 0$ and $G''_{\text{HN}}(\omega) \rightarrow 0$ by (1.62), and $\theta_{\text{HN}} \approx \alpha\frac{\pi}{2}$ by (1.70), so

$$\frac{G''_{\text{HN}}}{G'_{\text{HN}}} \approx \tan\left(\alpha\gamma\frac{\pi}{2}\right) \quad (1.81)$$

which indicates that parametrically near the $G'G''$ origin, the HN function has a constant slope of $\tan\left(\alpha\gamma\frac{\pi}{2}\right)$. Which means that the angle the HN function makes with the G' axis near the origin is $\alpha\gamma\frac{\pi}{2}$.

For low frequencies $\omega \ll 1/\tau$, $G'_{\text{HN}}(\omega) \rightarrow 1$ and $G''_{\text{HN}}(\omega) \rightarrow 0$ by (1.62), and $\theta_{\text{HN}} \approx (\omega\tau)^\alpha \sin(\alpha\pi/2) \approx 0$ by the first term in the Taylor series of equation (1.70). So, without any approximations

$$\frac{G''_{\text{HN}}}{G'_{\text{HN}} - 1} = \frac{\sin(\gamma\theta_{\text{HN}})}{\cos(\gamma\theta_{\text{HN}}) - (1 + 2(\omega\tau)^\alpha \cos(\alpha\frac{\pi}{2}) + (\omega\tau)^{2\alpha})^{\gamma/2}} \quad (1.82)$$

Since ω is small, $(\omega\tau)^{2\alpha}$ is small compared to $2(\omega\tau)^\alpha \cos(\alpha\frac{\pi}{2})$, so we drop the former. Then, using the binomial approximation, we have

$$\frac{G''_{\text{HN}}}{G'_{\text{HN}} - 1} \approx \frac{\sin(\gamma\theta_{\text{HN}})}{\cos(\gamma\theta_{\text{HN}}) - 1 - \gamma(\omega\tau)^\alpha \cos(\alpha\frac{\pi}{2})} \quad (1.83)$$

And since $\theta_{\text{HN}} \approx 0$, we approximate $\sin(\gamma\theta_{\text{HN}}) \approx \gamma\theta_{\text{HN}}$ and $\cos(\gamma\theta_{\text{HN}}) \approx 1$ by taking the first terms of their Taylor series'. Therefore, we have

$$\frac{G''_{\text{HN}}}{G'_{\text{HN}} - 1} \approx \frac{\gamma\theta_{\text{HN}}}{1 - 1 - \gamma(\omega\tau)^\alpha \cos(\alpha\frac{\pi}{2})} \quad (1.84)$$

or

$$\frac{G''_{\text{HN}}}{G'_{\text{HN}} - 1} \approx -\frac{\gamma(\omega\tau)^\alpha \sin(\alpha\frac{\pi}{2})}{\gamma(\omega\tau)^\alpha \cos(\alpha\frac{\pi}{2})} \quad (1.85)$$

$$\approx -\tan\left(\alpha\frac{\pi}{2}\right) \quad (1.86)$$

which indicates that near (1,0) on the $G'G''$ -plane, the HN function has a constant slope of $-\tan(\alpha\frac{\pi}{2})$, meaning the (acute) angle made on that end is $\alpha\frac{\pi}{2}$.

This method of fitting α and γ independently of τ is referred to as Davidson's method in the literature because he used it to fit γ in the 1951 paper [12, 39]. See Figure 1.7 for a synthetic example of this method for the Debye, CC, CD, and HN functions.

We can use this fitting method even if the relaxation function is not a form of the HN equation. As noted earlier, the high and low frequency log-log slopes of the HN function are $\alpha\gamma$ and α , respectively. This corresponds to the angles of $\alpha\gamma\pi/2$ and $\alpha\pi/2$ found above. So, regardless of the relaxation function used, if it has slopes of $-b$ for low frequencies and a for high frequencies, then in

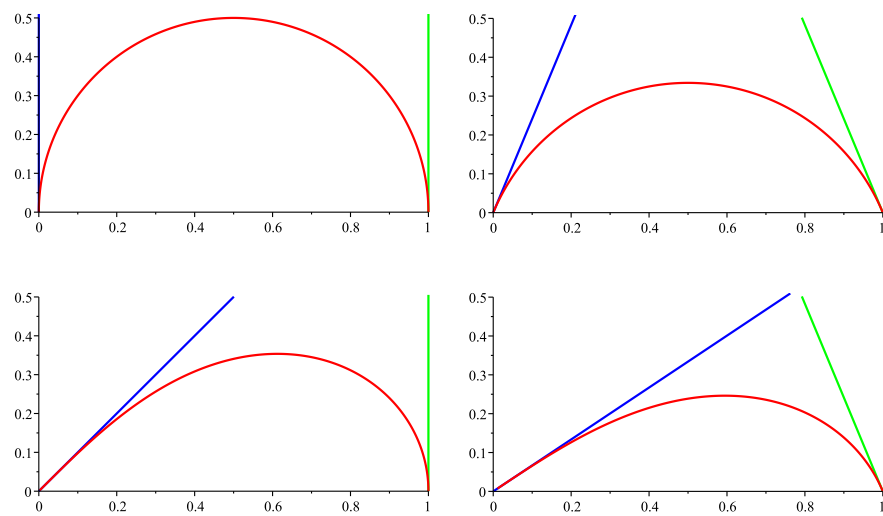


Figure 1.7: Cole-Cole plots for the HN function with $\alpha = \gamma = 1$ (top left), $\alpha = 0.75$ and $\gamma = 1$ (top right), $\alpha = 1$ and $\gamma = 0.5$ (bottom left), and $\alpha = 0.75$ and $\gamma = 0.5$ (bottom right). The tangent lines are drawn in with angles of $\alpha\gamma\pi/2$ on the left hand side and $\alpha\pi/2$ on the right hand side of each plot.

the Cole-Cole plot it will approach straight lines with angles $b\pi/2$ at $(0, 0)$ and $a\pi/2$ at $(1, 0)$. The rest of the shape could be different, but those parameters can be fit even without knowing the functional form.

We can see this in the context of the von Schweidler law (1.58) and (1.59). Its ratio of imaginary to real parts is

$$\frac{G''_{\text{vS}}}{G'_{\text{vS}}} = \tan\left(b_{\text{vS}} \frac{\pi}{2}\right) \quad (1.87)$$

Comparing to equation (1.81), we have

$$b_{\text{vS}} = \alpha\gamma \quad (1.88)$$

Therefore, any equation that follows the von Schweidler law at high frequencies with log log slope b_{vS} can have that parameter fit with a Cole-Cole plot.

For example, we can fit the parameter β from the KWW function in this manner. As noted earlier, the low and high log-log slopes are 1 and $-\beta$, so the angles made with the G' axis are $\beta\pi/2$ and $\pi/2$, respectively (see Figure 1.8). Therefore, the parameters for the HN and KWW functions are related by

$$\alpha\gamma = \beta \quad (1.89)$$

when fit in this manner.

Another Approach: Defining Only the Imaginary Part As mentioned above, the Kramers-Kronig relations imply that G' and G'' are Hilbert transforms of one another, so just the imaginary part, the loss, contains as much information as the full dynamic modulus.

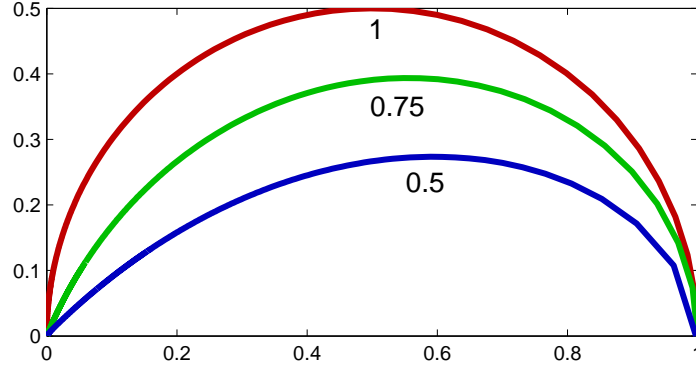


Figure 1.8: Cole-Cole plots for the DFT of the normalized KWW function with $\beta = 1, 0.75,$ and 0.5 as labeled.

In 1941, Fuoss and Kirkwood [18] used the equation

$$G''_{\text{FK}}(\omega) = \frac{2G_p''(\omega\tau)^m}{1 + (\omega\tau)^{2m}} \quad (1.90)$$

which is a generalization of the imaginary part of the Debye equation (1.56) that gives the symmetric log-log slopes of $\pm m$. Note that the form here is no longer normalized, but includes a fit parameter for the peak height G_p'' . This is the Fuoss-Kirkwood (FK) equation.

A more general version of this is the Jonscher equation [32]

$$G''_{\text{Jonscher}}(\omega) = \frac{K}{(\omega/\omega_1)^{-m} + (\omega/\omega_2)^n} \quad (1.91)$$

which has low and high frequency log-log slopes of m and $-n$, respectively. The parameter K is proportional to the peak height.

The FK and Jonscher's equation are similar in behavior at low and high frequencies to the CC and HN equations, respectively. But, comparing

equations (1.74) and (1.72) to the above, it's clear that they are not the same. The difference is the shape at the peak itself.

A simple frequency domain relaxation function was proposed by R. Bergman [4]. As discussed previously, because of causality, the entire complex modulus is determined completely by the loss. And, exponential decay appears as a peak in the loss with in general two different slopes on a log-log plot. So, starting with that very general idea

$$\frac{G_p''}{G''(\omega)} = A\omega^{-a} + B\omega^b + C \quad (1.92)$$

where G_p'' is the loss at the peak. Then, with some simple manipulation assuming there to be a peak at ω_p Bergman obtains a very general five parameter equation,

$$G''(\omega) = \frac{G_p''}{\frac{1-C}{a+b}[b(\omega/\omega_p)^{-a} + a(\omega/\omega_p)^b] + C} \quad (1.93)$$

It can be shown [4] that with the correct choices of the parameters, equations (1.75), (1.90), and (1.91) are special cases of (1.93). To approximate a KWW function, he sets $a = 1$ and $C = 1 - b$, resulting in

$$G''(\omega) = \frac{G_p''}{1 - b + \frac{b}{b+1}[b(\omega_p/\omega) + (\omega/\omega_p)^b]} \quad (1.94)$$

A log-log plot of this function produces a line with slope 1 for low frequencies, and slope b for high frequencies, which is similar in behavior to the DFT of the KWW function. Also, except for relatively small $\beta < 0.3$ or so, $b \approx \beta$. An inverted KWW function (one that has the variable slope in the low frequencies) is similarly constructed,

$$G''(\omega) = \frac{G_p''}{1 - a + \frac{a}{a+1}[(\omega/\omega_p)^{-a} + a(\omega/\omega_p)]} \quad (1.95)$$

Overview

Following the discussion about Cole-Cole plots and the von Schweidler law above, we can relate all the shape parameters described above by

$$b_{\text{vS}} = \beta = \alpha\gamma = n = b \quad (1.96)$$

and analogously

$$\alpha = m = a \quad (1.97)$$

The peak location on the frequency axis has been described in two equivalent ways

$$\omega \propto 1/\tau \quad (1.98)$$

The peak height has also been describe in two equivalent ways

$$G_p'' \propto G_0 - G_\infty \quad (1.99)$$

the exact proportions here depend on the units used for ω .

1.2.3 Summary

In the study of amorphous solids, working in the linear response regime opens up a broad, powerful mathematical tool-set, Fourier theory. Using this we can relate how a material relaxes into equilibrium to how a material reacts to a sinusoidal “force” applied to it. So, looking at frequency domain data, which is sometimes more convenient, is equivalent to looking at time domain data.

The specific models used to fit the resultant transfer function are curve fits initially designed to fit specific data sets but were found to be generally useful. All the models described in this chapter were initially used to

describe electromagnetic phenomena, but were later used to fit mechanical and thermodynamic data as well, which speaks to the power of the theory.

However, there is no theoretical basis for the models presented, and it is a common practice in the literature to simply use whichever form best fits the data with the fewest number of parameters.

Also, we have seen that the similarity in the low and high frequency limits leads to the shape parameters in the models actually being the same, and the remaining scale and location parameters are easily related. With the use of Cole-Cole plots, we can then fit the shape parameters without need of a functional form. All of this suggests that the shape parameters are intrinsic to the system. However, once one makes an assumption about which model to use, then after doing a least squares fit, one can often get drastically different (as much as a 50% difference) results for the shape parameters [39]. This is because by choosing one model or another, one makes an assumption for the form of the data, which it might not follow exactly.

There is some debate about the usefulness of the distribution of relaxation times; some view it purely as a mathematical tool [39,2,4]. But it does seem plausible that some sort of distribution of relaxation times is the root cause of the observed phenomena, given the success of the models described above. The problem with this idea is that the distributions vary drastically between models. For example, the CD and KWW functions have the same number of parameters, similar Cole-Cole plots at the far ends, and even somewhat similar looking frequency domain forms, but the distributions of their relaxation times are very different. The KWW distribution is spread smoothly

over a range of times, whereas the CD distribution function is suddenly cut off at τ .

Quite simply, the major problem in this field is too many models that seem plausible and fit the data.

1.3 Dynamic Heat Capacity

As mentioned above, the dynamic heat capacity is a linear response function that tracks the relationship between energy, temperature, and frequency (or time). As such, all the tools described in the previous section are applicable and are widely used.

Specifically, the connection between the time and frequency domain is given by the fluctuation dissipation theorem [7, 43]. This states that

$$C_V(\omega) = -\frac{1}{k_B T^2} \int_0^\infty \left(\frac{d}{dt} \langle \Delta E(t) \Delta E(0) \rangle \right) e^{-i\omega t} dt \quad (1.100)$$

at constant volume, where E is the energy, $\Delta E = E - E_{\text{eq}}$ is the energy fluctuation from equilibrium, and $\langle \rangle$ denotes an average. This has the equivalent, more convenient, form

$$C_V(\omega) = \frac{\langle \Delta E^2 \rangle}{k_B T^2} - \frac{i\omega}{k_B T^2} \int_0^\infty \langle \Delta E(t) \Delta E(0) \rangle e^{-i\omega t} dt \quad (1.101)$$

At constant pressure this is

$$C_V(\omega) = \frac{\langle \Delta H^2 \rangle}{k_B T^2} - \frac{i\omega}{k_B T^2} \int_0^\infty \langle \Delta H(t) \Delta H(0) \rangle e^{-i\omega t} dt \quad (1.102)$$

where H is the enthalpy.

Also, as mentioned previously, a major advantage of looking at dynamic specific heat spectra is that all the modes of the system should be probed. It is probing the system at a fundamental thermodynamic level [5].

1.3.1 Experiment

The experimental work in this area is very large, so only a brief overview of the main points is presented here.

As mentioned above, the technique was first introduced by Birge and Nagel [5] and by Christensen [10] in 1985. Both papers considered the dynamic heat capacity of glycerol, and measured the dynamic heat capacity using a modulating thermostat. Birge and Nagel fit the spectrum with the KWW function, equation (1.44), and tracked the relaxation time with the Vogel-Fulcher law (1.2). They observe similarity to other types of susceptibility functions (mechanical and dielectric) but also note that their peaks in the loss were wider because the dynamic specific heat probes all modes in the system, which is not necessarily the case for other susceptibilities (e.g. the dielectric susceptibility only sees motions tied to electric fields). This universality of the technique makes it useful in the study of any glass forming system.

Another similar experimental methodology is where the frequency of the modulating thermostat is held fixed, but the mean temperature is varied instead. The peak in the loss and the drop in the storage of the dynamic heat capacity move to lower frequencies for lower temperatures and higher frequencies for higher temperatures, so one is able to trace out the relaxation function by fixing the frequency and varying the temperature. If the shape of the function does not vary with temperature, then you can reconstruct the relaxation behavior. In any case, you can define a glass transition at that frequency by the temperature at which the storage part of the dynamic heat capacity drops. This technique is primarily utilized in experiment because temperature is rel-

actively easily changed, whereas to fully measure the dynamic heat capacity in frequency space might take many orders of magnitude of frequencies beyond the capabilities of a modulated calorimeter [28]. For example, a study of glucose and fructose by Ike, Seshimo, and Kojima uses Cole-Cole plots and fits with the Havriliak-Negami and KWW functions [28]. (See for example Figures 2 and 3 from reference [28].)

1.3.2 Simulation

Dynamic heat capacity has not been explored as thoroughly in simulation as it has in experiment. The author is only aware of a few studies other than the present one. Some molecular dynamic studies include Grest and Nagel on a binary Lennard-Jones mixture with parameters selected to model glycerol [22]; Scheidler, Kob, Latz, Horbach, and Binder on a binary Buckingham plus Columbic mixture with parameters selected for silica [51]; Yu and Carruzzo on a binary, repulsive, soft-sphere mixture [57]; and Brown (this author), McCoy, and Adolf on a bead spring Lennard-Jones mixture [6].

A typical result of most of the above works is similar to the one in Figure 1.9. The low frequency limit of the storage is the standard thermodynamic heat capacity. For somewhat higher frequencies, the storage drops to another plateau, and there is a peak in the loss. This is indicative of relaxation behavior as discussed above. The change in the specific heat capacity at these timescales is associated with a configurational contribution. The next major drops in the storage and peaks in the loss are on timescales that correspond to unbonded and bonded interactions and appear to be about a 10 times more significant contribution to the heat capacity. These peaks are associated with

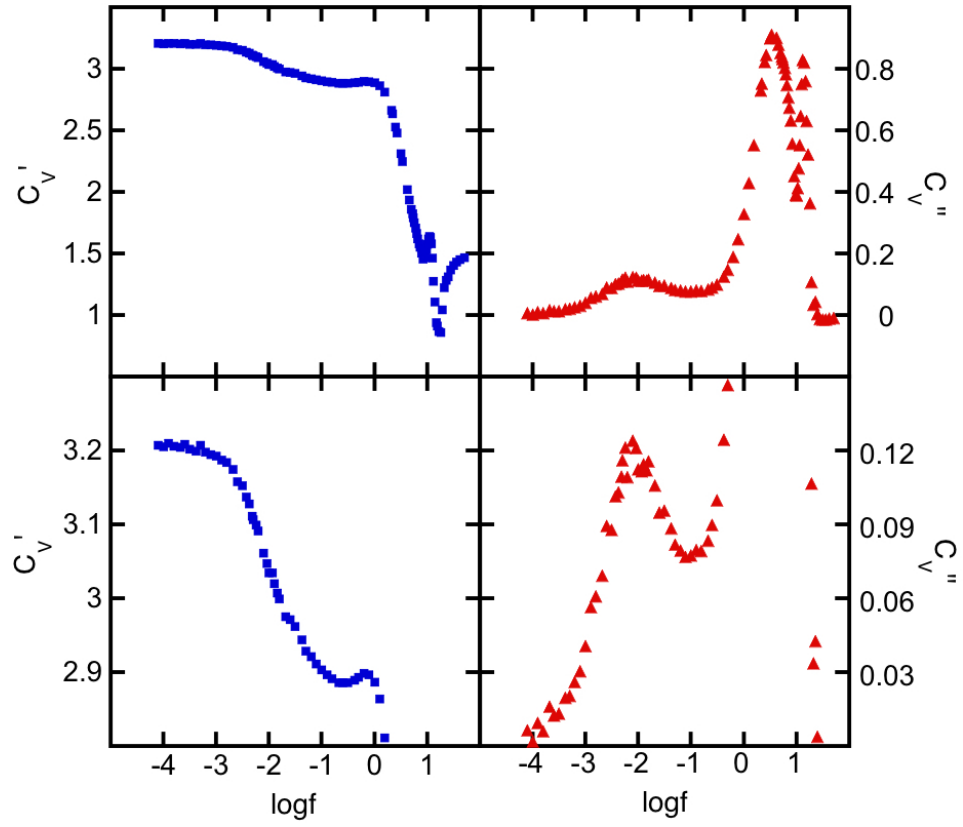


Figure 1.9: Sample specific heat capacity spectrum for the bead-spring system. The real part (storage) is on the left, and the imaginary part (loss) is on the right. The top is the full spectrum, and the bottom is a zoom in of the configurational part of the spectrum. The system is at a fixed mean temperature, volume, and number of particles.

exciting the bonds as harmonic oscillators, and appear fairly spread out due to the disorder of the system [51]. In the high frequency limit, the loss decays to zero, and the storage approaches a value of $3/2$, which is the ideal gas limit. That is, on those timescales, the interactions of the particles are not important and the fluctuations in the energy are just in the kinetic energy, or temperature. Further, as temperature is decreased (or density is increased) the peaks move farther from one another, potentially diverging. And, as temperature is increased (or density is decreased) the peaks move together, eventually merging at the caging transition [6].

Also worth mentioning is the work of Hentschel et. al. [25, 26]. They compute the thermodynamic heat capacity of a two dimensional simulated binary mixture (i.e. a mixture of two sized of particles) of repulsive soft spheres and note two peaks in the heat capacity at different temperatures. The peaks, they say, are associated with the formation of close packed clusters of like particles. They extend this idea to dynamic heat capacity by assigning a cluster size a lifetime and working out the contribution of such clusters to the total dynamic heat capacity by saying that each cluster size gives rise to a Debye process. Their analysis, however, does not account for the large high frequency peak in the loss due to fast time processes, and it is unclear the amount of predictive power the idea has, other than looking approximately correct for well chosen lifetimes because measuring those lifetimes is difficult. See for example Figures 8 and 9 in reference [26], where appropriately chosen parameters approximate the response of glycerol.

Another interesting simulation study is the energy landscape model

of Chakrabarti and Bagchi [9]. They consider two potential energy meta basins that are made up of independent two level systems, where transfers between the meta basins are only allowed if all the constituent two level systems are excited. Despite the huge difference between this model and the MD studies above, the results are quite similar to Figure 1.9 (see for example Figures 3 and 4 from reference [9]). They see two distinct peaks in the loss that move apart for decreasing temperature, and merge for increasing temperature. Also, the fast-time process (the two level systems) contributes about ten times more to the specific heat than the long time process (moving between meta basins). However, because of the simplicity of the model, fitting these peaks showed that they were both due to Debye (i.e. single exponential) processes [9].

Also of interest is a study on the dynamic heat capacity of a Ising spin system by Li et. al. [38]. They noted that the mean field approximation did not fully represent the dynamics, but as expected did not see evidence of a phase transition at nonzero temperature for a one dimensional system.

The east model, as we will see in the next section, lacks explicitly defined β -processes, so we don't expect to see the double peak, only the single configurational peak.

1.4 The East Model

The Ising model was initially created in 1924 as a model of magnetization with interaction between particles. In one dimension, we have a line or loop of spins (up or down) that interact ferromagnetically or antiferromagnetically. That is, high and low energy states are defined by whether adjacent

spins are aligned or antialigned [29].

It is notable because the statistical mechanics and thermodynamics of it is exactly solvable in one and two dimensions, and there is a phase transition in two dimensions but none in one dimension [45, 29]. A generalization of the Ising model to add time so as to apply to glassy systems was put forth in the mid 1980s [16, 17, 46]. The east model, proposed later, is the simplest of such systems in terms of analysis, and its total relaxation time has been solved. These models have thermodynamics identical to the standard Ising model but complex dynamics.

1.4.1 Kinetically Constrained Ising Models

One theory of the glass transition, why the dynamics of a system become extremely slowed down, has to do with a local constraint on the motion of individual parts (atoms/molecules) of the system. In this way of thinking, when a liquid is supercooled parts of the material get stuck in some local potential energy well, unable to rearrange themselves into a crystal, and there are high energy defects in the structure that are mobile. For the system to react to some outside force, the stuck places may only move if they interact with a defect. The defects, in effect, sweep through the system equilibrating it. For lower temperatures, the defects become slower and/or more rare leading to a slowing of the dynamics [14]. We can take advantage of the simplicity of the Ising model to model these defect/stuck systems by adding dynamical rules.

The initial kinetically constrained model, the Fredrickson and Andersen model, took the one dimensional Ising model and added time with the

constraint that spins were only mobile if they were adjacent to a high energy juncture on either side [16, 17]. More generally, in higher dimensions, sites are mobile if adjacent to a specific number of high energy junctures. Since these become sparse for lower temperatures, and since flips that put the system into a higher energy state also become less likely for lower temperature, the dynamics of the system slow down very quickly for low temperature. This model is usually classified as a strong glass former because the relaxation time follows the Arrhenius equation (1.1) [14]. The east model is similarly defined, but the constraint is only in one direction [31].

In the same year as the Fredrickson and Andersen paper, a more general class of models were defined by Palmer et. al. called hierarchically constrained models [46]. Here, spins are only mobile if a specific set of neighbors are active, as opposed to a specific number of neighbors. They find that in the long and continuous time limit, these models show KWW relaxation. This is a remarkable result, since a stretched exponential like relaxation function is practically universally seen in experimental work on glasses and this is a simple model. However, they don't believe that relaxation times are discrete, or that the distribution of relaxation times necessarily has meaning [46]. Rather, they were showing that a hierarchical constraint can give rise to a KWW relaxation, and that a continuous analogue could be the underlying mechanism. The east model is one of the simplest in the class of models defined by Palmer et. al. [31].

1.4.2 Definition and Basic Properties

In the standard one dimensional Ising model, we have a lattice of spins α_i , $i = 1, 2, \dots, N$ that can take either one of two states, up or down, 1

or -1 [40]. The initial purpose is to model particle interactions by magnetic dipoles, so the energy or Hamiltonian of the system is given by

$$E = - \sum_{i=1}^N \alpha_i \alpha_{i+1} \quad (1.103)$$

where we generally have periodic boundary condition so that $\alpha_1 \equiv \alpha_{N+1}$. That is, the energy contribution of the adjacent aligned spins is -1, and the energy contribution of anti-aligned spins is +1. We could also make aligned the high energy state and anti aligned the low energy state (i.e. antiferromagnetic instead of ferromagnetic), but it doesn't matter much here.

The East model reinterprets the interactions somewhat [31]. The aligned spins, areas of low energy, become a region where the system has no mobility. The exact interpretation is unclear, this is considered to be a region with low temperature or perhaps a localized potential energy well, where the atoms are just jammed together in some way that is hard to break out of [19]. Such structures, areas where there are high and low mobility are called dynamic heterogeneities in the literature, and how they evolve is a way to characterize the glass transition [30, 19, 42]. What becomes important, then are the interfaces. Instead of the standard lattice of spins, we define a new lattice of “spins” (representing interfaces) s_i , $i = 1, 2, \dots, N$ that take values of up or down (with associated occupation numbers 1 or 0) for an interface with or without a change in direction, respectively. The energy is now (up to some constant shift),

$$E = \sum_{i=1}^N s_i \quad (1.104)$$

It is useful now to frame the analysis of this system in the canonical ensemble, that is fixed temperature, number of particles/sites, and volume. Under these conditions, it can be shown by statistical mechanics that the probability distribution of the microstates of the system follows a Boltzmann distribution [40]. Namely, the probability that the system is at state i with energy E_i is

$$p_i = \frac{1}{Z} e^{-\beta E_i} \quad (1.105)$$

where $\beta = \frac{1}{k_B T}$, k_B is the Boltzmann constant, and Z is the normalization constant. The normalization constant Z is also referred to as the canonical partition function.

We can solve for the canonical partition function in the usual way:

$$Z = \sum_{\text{states}} e^{-\beta E_{\text{state}}} \quad (1.106)$$

Since the energy of each site is independent of the other sites, this sum can be factored as

$$Z = \left(\sum_{s_1=0,1} e^{-\beta s_1} \right) \left(\sum_{s_2=0,1} e^{-\beta s_2} \right) \dots \left(\sum_{s_N=0,1} e^{-\beta s_N} \right) \quad (1.107)$$

or

$$Z = (1 + e^{-\beta})^N \quad (1.108)$$

The ensemble average or expected value of the energy is

$$\langle E \rangle = \sum_{\text{states}} E_{\text{state}} p_{\text{state}} \quad (1.109)$$

plugging in equation (1.105), this is

$$\langle E \rangle = - \frac{d \ln Z}{d\beta} \quad (1.110)$$

Specifically, using equation (1.108) this is

$$\langle E \rangle = \frac{N}{1 + e^\beta} \quad (1.111)$$

The energy per site $\langle E \rangle$ is just the concentration of up spins c . That is,

$$c = \frac{\langle E \rangle}{N} = \frac{1}{1 + e^\beta} \quad (1.112)$$

The thermodynamic specific heat per site $C_V = d\langle E \rangle/dT$ is easily computed to be [40]

$$C_V = \frac{1}{4k_B T^2 \cosh^2\left(\frac{1}{2k_B T}\right)} \quad (1.113)$$

The above discussion is just for the one dimensional Ising model, whose statistical mechanics are exactly solvable. Making this a model for a glass forming system is done by incorporating time and evolving the system using Monte Carlo. We enforce the mobility interpretation by only allowing spins whose neighbor to the left is up to flip [31]. The one sided constraint is incorporated to put in cooperative behavior; up spins are free to move right, but to move left, another up spin to its left has to move over and flip it [31]. If flipping decreases energy (that is, we have an up to the left of an up), then we perform the flip and move on. If flipping would increase energy (that is an up to the left of a down), then we only perform the flip with probability $p = \exp(-1/T)$, where T is the temperature. The probability comes from the Boltzmann distribution with $k_B = 1$ (this essentially just sets the units of temperature), and the fact that we are working in the canonical ensemble. That is,

$$\mathcal{P}(11 \rightarrow 10) = 1 \tag{1.114}$$

$$\mathcal{P}(10 \rightarrow 11) = \exp(-1/T) \equiv p \tag{1.115}$$

where I've used the occupation numbers for the spin states for clarity and convenience. Note that, by substituting $k_B = 1$ into equation (1.112), the probability of a site being up is

$$c = \frac{1}{1 + e^{1/T}} = \frac{p}{p + 1} \tag{1.116}$$

An alternative, and in fact original, definition is where the probability of an active up flip relaxing is $1 - p$ instead of just 1, this occasionally condenses two of the above steps into one [31]. However, in the low temperature limit $p \ll 1$ and the two versions become identical; they differ mainly for high temperatures where the version in equations (1.114) and (1.115) gives the $1/2$ concentration of up spins for infinite temperature like in equation (1.116) and in the other version that concentration is one. Further, one could chop up the time scale by introducing a time step Δt and multiply the flip probabilities by that, so in the definition shown above, that will be used throughout this work, $\Delta t = 1$. The version of the east model used here is due to Sollich and Evans and is also used in other recent work [14, 53, 30, 19].

1.4.3 Spin Autocorrelation

Much of the work on the east model has focused on finding a model for the spin autocorrelation function. That is, for a generic state s starting at

time $t = 0$ the spin autocorrelation is

$$C(t) = \frac{\langle \Delta s(t) \Delta s(0) \rangle}{\langle (\Delta s(0))^2 \rangle} \quad (1.117)$$

where the zero time point is arbitrary, the averages are taken in equilibrium, and the fluctuations are given by $\Delta s = s - c$, where c is the probability a site is up from equation (1.116).

Recall from equation (1.100) and the definition of energy in the east model equation (1.104), that the Laplace transform of the derivative of this equation is related to the dynamic heat capacity, so working with the spin autocorrelation is mathematically equivalent to working with the dynamic heat capacity.

See Figure 1.10 for an example of the energy autocorrelation function simulated for the east model. This plot is similar in shape to ones in the literature of the spin autocorrelation and spin persistence (fraction of up spins still up after a given time) functions.

The initial paper on the east model fit this to a KWW (1.44) form with limited success [31]. At early timescales the autocorrelation function appears exponential, only switching to a stretched exponential form for limited timescales later (see Figures 4, 5, and 6 from reference [31]).

A later study by Pitts, Young, and Andersen also employed Monte Carlo to investigate the spin autocorrelation of the east model [48]. They, too, found that the KWW form only works in certain timescales. The autocorrelation function seems to jump suddenly from one β_{KWW} to another (see Figure 2 in reference [48]).

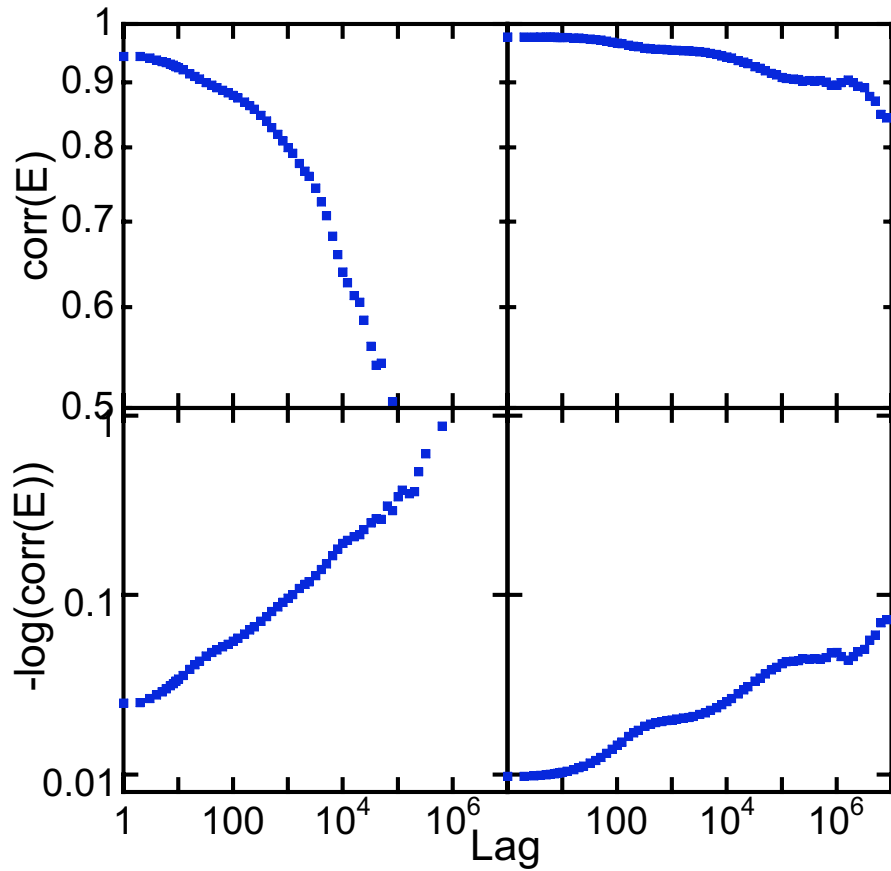


Figure 1.10: Sample energy autocorrelation for the east model. The left plots are for $T = 0.35$ and the right two plots are for $T = 0.2$. The top two plots are log autocorrelation vs. log time. The bottom two are $-\log\log$ autocorrelation vs. log time, and on this type of plot a stretched exponential function would be a straight line.

The explanation for this behavior initially arose from mode coupling approximations and effective medium approximations, but those proved ultimately inadequate to explain the behavior at all time scales [13, 47, 48]. For example, see Figure 10 from reference [47].

1.4.4 Domains

A better method for modeling the relaxation is by a so-called cluster approximation [13, 14, 53]. Here, we take a larger view of the system, instead of looking at an average spin in an average environment, we consider the local structure. The basic structures are domains of continuous down spins that are between two up spins. That is, we chop up the domain every time we see an up spin. Schematically,

$$110000101000101 \rightarrow 1|1|00001|01|0001|01$$

Let D be the number of spins in a domain, including the terminating up spin on the right hand side. It is implicitly assumed that each domain is immediately adjacent to the next, so immediately to the left of any domain is an up spin that terminates the previous domain. In equilibrium the distribution of the up spins is random since no configuration is preferred. Therefore, starting from an up spin and moving right, the probability of each site being up is c from (1.116) - this can be thought of as independent Bernoulli trials - so the number of sites you visit before coming to an up spin (the domain length) has a geometric distribution with Bernoulli parameter c . Specifically, the probability that a domain has a length d is

$$\mathcal{P}(D = d) = c(1 - c)^{d-1} = \frac{p}{(1 + p)^d} \quad (1.118)$$

The average domain length is the expected value of the geometric distribution.

i.e.

$$d_{\text{avg}} = \frac{1}{c} = 1 + \frac{1}{p} \quad (1.119)$$

The independence of the state of each spin in equilibrium also implies that the lengths of any two domains are uncorrelated.

Now we can consider the dynamics of a domain as if we can pick it out of a hat and treat it independently. This is at least approximately true because from equations (1.114) and (1.115) we can completely disregard anything to the right of the domain. Also, in the low temperature limit, up spins tend to be very isolated, so we can treat the up spin to the left of the domain as being fixed.

The insight of Sollich and Evans with regard to these dynamics was to consider the energy barrier that a domain has to go over in order to relax [14,53]. The simplest cases are where we have $d = 2^n$ for some n . In order to make the transition,

$$1 \cdots 1 \rightarrow 1 \cdots 0$$

(where the dots indicate some string of down spins) one can flip the site halfway across up and use that as a way of accessing the sites on the right half of the domain. i.e.

$$1 \cdots 0 \cdots 1 \rightarrow 1 \cdots 1 \cdots 1 \rightarrow 1 \cdots 1 \cdots 0 \rightarrow 1 \cdots 0 \cdots 0$$

To accomplish each of the transitions above, you must at least flip up the spin halfway in between each of the subdomains (but not necessarily at the same time). Continuing in this manner, one eventually reaches a subdomain length

of one, and we're done. Not counting the terminal up spins on the right and left hand sides of the domain, the minimum number of spins that have to be up at a particular time in the process of the domain relaxing is n . We can think of this as a recurrence relation, with $E_n = E_{n-1} + 1$ and $E_1 = 0$, which has solution $E_n = n$.

More generally, if $2^{n-1} < d \leq 2^n$, the first up spin we have to place is still in the 2^{n-1} place, and the rest of the analysis proceeds as above (on the left hand subdomain) to get from totally unrelaxed to that first up spin. Thus, the minimum energy barrier is

$$E_{\text{barrier}}(d) = n \quad (1.120)$$

Treating this as an activated process, the rate of removal of a domain is given by an Arrhenius law. That is,

$$\Gamma(d) \propto \exp\left(-\frac{E_{\text{barrier}}(d)}{k_B T}\right) = \exp(-n/T) \quad (1.121)$$

The inverse of this is the relaxation time, and plugging in $p = \exp(-1/T)$, we have

$$\tau_d \propto \exp(n/T) = p^{-n} \quad (1.122)$$

where $2^{n-1} < d \leq 2^n$.

Noting that $n - 1 < \log_2 d \leq n$, Sollich and Evans approximate the energy barrier as

$$E_{\text{barrier}}(d) \approx \frac{\ln d}{\ln 2} \quad (1.123)$$

That is, their approximation of the lifetime of a domain, τ_d , is

$$\tau_d \approx d^{\frac{1}{T \ln 2}} \quad (1.124)$$

1.4.5 Relaxation Time

A simple consequence of the above discussion of the dynamics of a particular domain, is that we can now approximate the average equilibration/relaxation time of the east model.

Combining equations (1.119) and (1.124), we have $d_{\text{avg}} \approx \exp(1/T)$ and $\tau_d \propto d^{1/(T \ln 2)}$, so

$$\tau_{\text{avg}} \propto \exp\left(\frac{1}{T^2 \ln 2}\right) \quad (1.125)$$

More rigorous work on the relaxation time keeps the EITS form, but the factor B from equation (1.3) becomes less clear. This was first done by Aldous and Diaconis and they derived the form

$$\ln \tau \leq \left(\frac{1}{\ln 2} + o(1)\right) \frac{1}{T^2} \quad (1.126)$$

and

$$\ln \tau \geq \left(\frac{1}{2 \ln 2} + o(1)\right) \frac{1}{T^2} \quad (1.127)$$

in the low temperature limit [1]. Their methodology was specific to the east model. A later proof of this fact was done by Cancrini et. al. and was based on more general techniques and they get that

$$\ln \tau = \frac{1}{T^2 2 \ln 2} \quad (1.128)$$

in the low temperature limit. This, they say, disproves equation (1.125) [8].

1.5 Overview of this Work

The primary focus of this work is to find and model the dynamic heat capacity of the east Ising model. First the east model is simulated with Monte

Carlo techniques. The temperature is modulated sinusoidally, and the energy is monitored. From that, the dynamic heat capacity is computed.

We apply common frequency domain relaxation models, namely the HN (1.62) and KWW (1.44) functions and a series of Debye relaxations (1.43). Because the KWW function lacks a closed form frequency domain version, we instead apply the approximation due to Bergman (1.94). The b , τ , and C''_{peak} parameters from equation (1.43) are fit to simulation data.

Next, expanding on the work of Sollich and Evans, we model the relaxation process as a series of Debye relaxations, each due to the relaxation of a different length domain. We hone the relaxation time predicted in equation (1.122) by equating τ_d to the mean first passage time from an unrelaxed state to the completely relaxed state. We do this by computing the Markov Chain transition matrix on a restriction of the model to the domain length d . Then, τ_d can be computed symbolically and numerically from this matrix. The resultant model for the dynamic heat capacity fits the Monte Carlo simulations very well.

One of the major advantages of this technique is that small wobbles in the time domain spin autocorrelation function, are seen to become distinct peaks in the dynamic heat capacity for low enough temperatures. The separate relaxation times computed with the Markov Chain techniques explain this behavior perfectly. This model is also useful for comparing with the KWW fits, to give an underlying reason for the behavior of those parameters. We are able, to a good degree of precision, to solve for the dynamics of a known glass former.

CHAPTER 2

METHODOLOGY

2.1 Dynamic Heat Capacity Simulation

In order to fit the HN and KWW functions and the Markov Chain model to the East Ising Model, we performed a Monte Carlo simulation.

2.1.1 Simulation

The simulation itself is just an application of the rules of the game, equations (1.114) and (1.115). A random starting configuration was chosen for all the sites, with the correct frequency of up spins, then time was iterated. At each step, frozen sites were skipped over and active sites were flipped with the correct probabilities. At each step, after an equilibration period, the temperature was recomputed to follow a sinusoidal form $T(t) = T_0 + \Delta T \sin(\omega t)$, and the flip probability was computed as in equation (1.115), i.e. $p = \exp(-1/T)$. The state of the system (step, temperature, and energy per site) was dumped and saved for post processing at regular intervals.

The Monte Carlo scheme was run for a range of 39 temperatures between 0.2 and 10, and for each temperature, runs for logarithmically spaced (twelve per order of magnitude) periods of 10 to at most 10^9 were done as needed. From this we are able to compute a dynamic heat capacity spectrum by post processing.

The amplitude of oscillations used were $\Delta T = 0.05T_0$, and the number of sites used was $N = 100,000$. However, in order to check that the results were not just an anomaly of these chosen parameters, both ΔT and N were varied for a more limited range of temperatures.

2.1.2 Dynamic Heat Capacity Computation

Returning to the general case, assuming the output function of equation (1.5) at a particular frequency ω , a simple computation shows

$$\int_0^{\frac{2\pi}{\omega}} g(t) \sin(\omega t) dt = \frac{\pi B \cos(\delta)}{\omega} \quad (2.1)$$

But by equation (1.19), $B \cos \delta = AG'$, which gives us a way to compute G' from $y(t)$,

$$G' = \frac{\omega}{A\pi} \int_0^{\frac{2\pi}{\omega}} y(t) \sin(\omega t) dt \quad (2.2)$$

Similarly,

$$G'' = \frac{\omega}{A\pi} \int_0^{\frac{2\pi}{\omega}} y(t) \cos(\omega t) dt \quad (2.3)$$

As discussed earlier, the results from actual simulation are not as clean. The actual energy is quite noisy, so to clean it up, we take an average over many periods. See Figure 2.1 for an example. And since the model is inherently in discrete time, instead of setting the frequency of oscillation, the period N is varied, and equations (2.2) and (2.3) have to be evaluated numerically. That is,

$$C'_V(N) = \frac{2}{AN} \sum_{n=1}^N (E_n - \bar{E}) \sin\left(\frac{2\pi}{N}n\right) \quad (2.4)$$

$$C''_V(N) = \frac{2}{AN} \sum_{n=1}^N (E_n - \bar{E}) \cos\left(\frac{2\pi}{N}n\right) \quad (2.5)$$

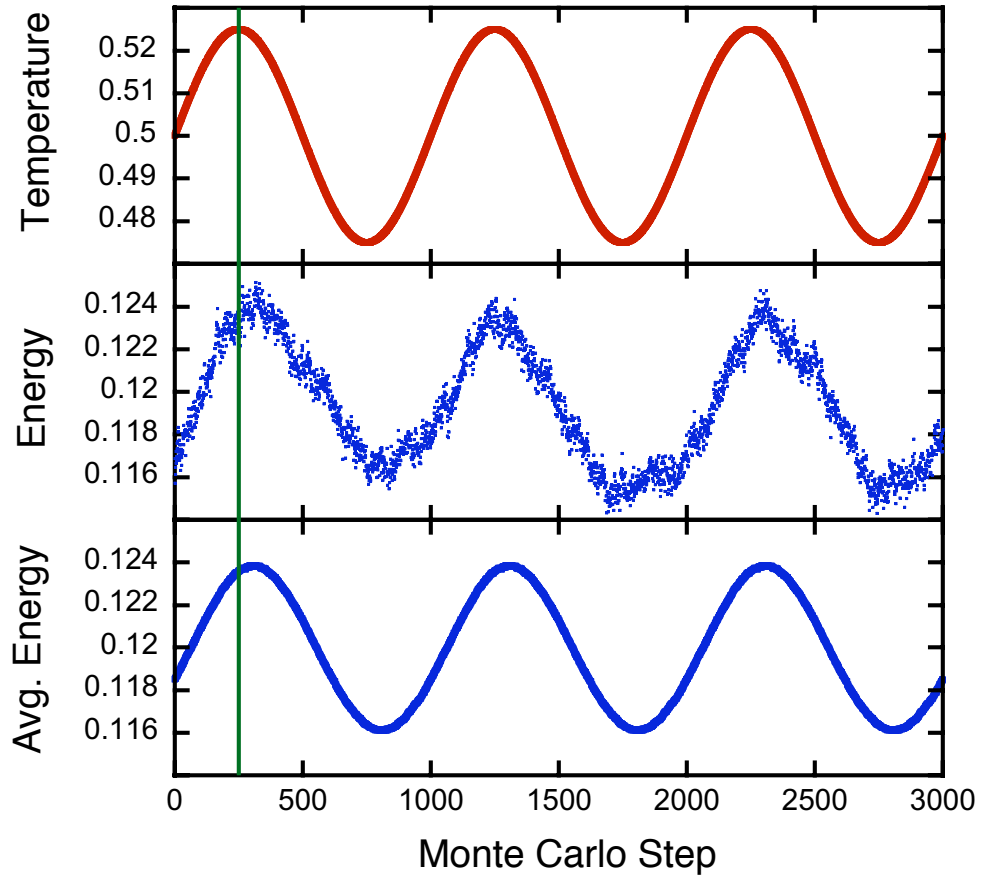


Figure 2.1: Sample output from an oscillatory experiment on the east model with $T=0.5$ at a period of 1000 MC steps. Top: the input temperature variation. Middle: the raw total energy output. Bottom: the average period of the total energy. The vertical line has been added to emphasize the phase lag between the temperature and energy.

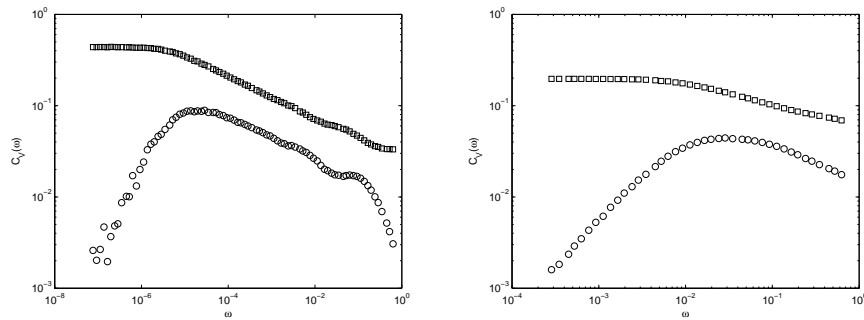


Figure 2.2: Example specific heat for $T = 0.4$ (left) and $T = 1.0$ (right) against frequency. The real part are the squares and the imaginary part are the circles.

where E_n is the sequence of averaged energy terms, and \bar{E} is the overall average energy. The average energy, i.e. the DC component, is removed for accuracy since it should cancel out anyway in the integration.

It is worth noting that equations (2.4) and (2.5) are just one of the discrete Fourier transform (DFT) terms for the time series E_n , but it's unnecessary to compute the full DFT because the rest of it should just be zero or noise.

See Figure 2.2 for an example of spectra for the east model obtained from this procedure.

2.2 Nonlinear Least Squares Fitting Procedure

We fit the dynamic specific heat data generated from the east model as described above to the HN and KWW forms using nonlinear least squares procedures. Specifically, to minimize the square residuals and find the optimal parameters, a Levenberg-Marquardt routine was implemented with a

few modifications [3, 44]. The following sections detail how complex-valued data, bounded parameters, widely varying parameters, and an only approximate functional form were dealt with.

2.2.1 Converting a complex problem to a real one

In general, if we want to fit complex data $y_i \in \mathbb{C}$, $i = 1, 2, \dots, m$ with associated real independent variables $x_i \in \mathbb{R}$ and errors $\sigma_i \in \mathbb{C}$ to a function $\phi(\mathbf{m}) : \mathbb{R} \rightarrow \mathbb{C}$ where $\mathbf{m} \in \mathbb{R}^n$ is the vector of parameters of ϕ , the least squares solution is the one that minimizes the l^2 -norm of the residuals. The weighted residuals $r_i(\mathbf{m})$, $i = 1, 2, \dots, m$ are given by

$$r_i(\mathbf{m}) = \frac{\Re(y_i - \phi(\mathbf{m}; x_i))}{\Re\sigma_i} + i \frac{\Im(y_i - \phi(\mathbf{m}; x_i))}{\Im\sigma_i} \quad (2.6)$$

Minimizing the l^2 -norm is the same as minimizing the function [52],

$$f(\mathbf{m}) = \frac{1}{2} \sum_{i=1}^m |r_i(\mathbf{m})|^2 \quad (2.7)$$

This can be written as,

$$f(\mathbf{m}) = \frac{1}{2} \sum_{i=1}^m [\Re(r_i(\mathbf{m}))^2 + \Im(r_i(\mathbf{m}))^2] \quad (2.8)$$

So, if we can find a function $\psi(\mathbf{m}) : \mathbb{R} \rightarrow \mathbb{R}$ and bijective mappings $g_1, g_2 : \mathbb{R} \rightarrow \mathbb{R}$ such that

$$\phi(\mathbf{m}; x) = \psi(\mathbf{m}; g_1(x)) + i\psi(\mathbf{m}; g_2(x)) \quad (2.9)$$

for all x in the domain of ϕ , then we can map this problem to a real nonlinear least squares problem with $2m$ data points. The new data is

$$\tilde{y}_i = \begin{cases} \Re(y_i) & , \quad i = 1, 2, \dots, m \\ \Im(y_i) & , \quad i = m + 1, m + 2, \dots, 2m \end{cases} \quad (2.10)$$

with associated real independent variables

$$\tilde{x}_i = \begin{cases} g_1(x_i) & , \quad i = 1, 2, \dots, m \\ g_2(x_i) & , \quad i = m + 1, m + 2, \dots, 2m \end{cases} \quad (2.11)$$

and errors

$$\tilde{\sigma}_i = \begin{cases} \Re(\sigma_i) & , \quad i = 1, 2, \dots, m \\ \Im(\sigma_i) & , \quad i = m + 1, m + 2, \dots, 2m \end{cases} \quad (2.12)$$

The residuals are now

$$\tilde{r}_i(\mathbf{m}) = \frac{\tilde{y}_i - \psi(\mathbf{m}; \tilde{x}_i)}{\tilde{\sigma}_i} \quad (2.13)$$

Therefore, by combining equations (2.7), (2.9) and (2.13), we have

$$f(\mathbf{m}) = \frac{1}{2} \sum_{i=1}^{2m} (\tilde{r}_i(\mathbf{m}))^2 \quad (2.14)$$

This f is exactly the same as the one above, so solving the modified real-valued nonlinear regression is identical to solving the complex valued one that we started out with.

Modified HN

Finding modified versions of the HN function is simple. The domain is restricted to the positive reals, so if we define

$$g_1(x) = x \quad (2.15)$$

and

$$g_2(x) = -x \quad (2.16)$$

Then the ψ functions can be defined on the whole real line by

$$\psi(x) = \begin{cases} \Re(\phi(x)) & , \quad T > 0 \\ \Im(\phi(-x)) & , \quad T < 0 \end{cases} \quad (2.17)$$

This is accomplished by directly using equations (1.72) and (1.73).

The gradient vectors that are needed depend only on the gradients with respect to \mathbf{m} of ϕ , and were derived from the equations for the real and imaginary parts of the HN function using Maple. The explicit form is complicated and not instructive to the discussion here.

A modified version of the KWW function is unnecessary because the approximation that we have is only defined for the imaginary part, so we will only need to fit that using the standard Levenberg-Marquardt method.

2.2.2 Bounded parameters

The parameters of both the HN and the KWW functions have to meet some physical constraints. Namely,

$$1 \geq \alpha, \gamma, b \geq 0 \quad (2.18)$$

since if these parameters were greater than one, this would correspond to faster than exponential decay. And

$$C_1, C_2, \tau \geq 0 \quad (2.19)$$

since specific heat and time cannot be negative, and where $C_1 \equiv G_\infty$ and $C_2 \equiv G_0 - G_\infty$.

To deal with this, we implement an active set method [44], with the constraints

$$\begin{bmatrix} I \\ -I \end{bmatrix} \mathbf{m} \geq \begin{bmatrix} \mathbf{l} \\ -\mathbf{u} \end{bmatrix} \quad (2.20)$$

where \mathbf{l} and \mathbf{u} are the lower and upper bounds, with elements in $\mathbb{R} \cup \{\infty\}$. In an active set method, we turn on or turn off equality constraints as necessary to keep the parameters in the feasible region. Let $A(\mathbf{m})$ be the set of active constraints, that is which variable are already at their limit and cannot be increased/decreased any further. The null space of unconstrained variable, in this case is simply

$$Z = [\mathbf{e}_{j_1}, \mathbf{e}_{j_2}, \dots, \mathbf{e}_{j_l}] \quad (2.21)$$

where

$$j_1, j_2, \dots, j_l \in \overline{A(\mathbf{m}^k)} \quad (2.22)$$

where $\overline{A(\mathbf{m}^k)}$ is the complement of the active set at \mathbf{m}^k .

When computing the LM steps, we use the effective gradient

$$\nabla_{\text{eff}} f(\mathbf{m}) = Z^T J(\mathbf{m})^T \tilde{\mathbf{r}}(\mathbf{m}) \quad (2.23)$$

where $J(\mathbf{m})$ denotes the Jacobian of $f(\mathbf{m})$. And the effective Gauss-Newton approximate Hessian is

$$\nabla_{\text{eff}}^2 f(\mathbf{m}) = Z^T J(\mathbf{m})^T J(\mathbf{m}) Z \quad (2.24)$$

That is, we simply turn on/off variables, the structure of Z is such that the LM step is computed in the same way as if the active constraint variables were not even present.

To add constraints to the active set, compute an LM step \mathbf{p}^k with the effective gradient and Hessian and let

$$I_l = \{i | m_i^k + p_i^k < l_i\} \quad (2.25)$$

and

$$I_u = \{i | m_i^k + p_i^k > u_i\} \quad (2.26)$$

then take

$$\alpha_k = \min \left(\min_{i \in I_l} \frac{l_i - m_i^k}{p_i^k}, \min_{i \in I_u} \frac{m_i^k - u_i}{p_i^k}, 1 \right) \quad (2.27)$$

then add the minimizing index, if any, to the active set, and update $\mathbf{m}^{k+1} = \mathbf{m}^k + \alpha_k Z \mathbf{p}^k$, where multiplying by Z correctly formats the step so it can be added to all of the parameters.

Also, we drop an active constraint j if moving into the feasible region is downhill, that is

$$m_j^k = l_j \quad (2.28)$$

and

$$\frac{\partial f(\mathbf{m}^k)}{\partial m_j} < 0 \quad (2.29)$$

or if

$$m_j^k = u_j \quad (2.30)$$

and

$$\frac{\partial f(\mathbf{m}^k)}{\partial m_j} > 0 \quad (2.31)$$

2.2.3 Multistart

As can be seen in Figure 2.2, the peak in the loss, which directly gives the value for τ , varies over many orders of magnitude for different temperatures, so a single good initial guess for τ that will be close enough to miss any potential local minima does not exist. The solution to this problem is multistart; we run the described modified LM algorithm with several starting values for τ logarithmically equally spaced from $\tau = 10$ to $\tau = 10^8$ and simply take the lowest residual result as the optimal solution. The other parameters do not vary as widely over the dataset, so multistart was found to be unnecessary for those parameters.

2.2.4 Cropped data

The high frequency side of that data shows some wobbly features that cannot be represented by the KWW or HN functions. These features are within error bars and so cannot be ignored as just random noise. Instead, to get a reasonable fit to the data, we cut off the worst of the high frequency data. An example of this is shown in Figure 2.3.

2.3 Domain Model

The other method that we will be considering is to consider the system to be a series of domains of down spins with an up spin on either side.

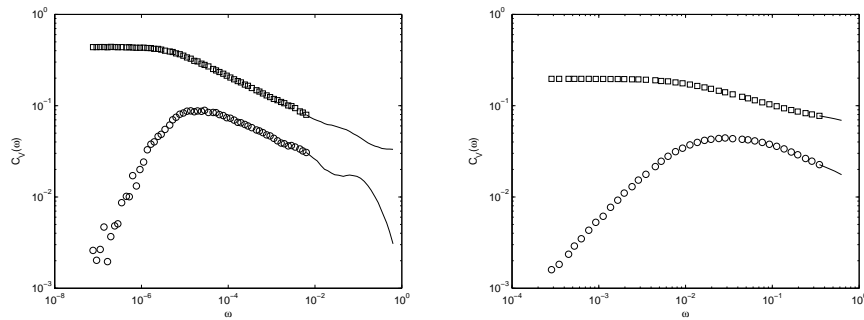


Figure 2.3: Example data for for $T = 0.4$ (left) and $T = 1.0$ (right), the solid line shows where data was cropped off.

2.3.1 Markov Chains

Each domain length will have a specific relaxation time associated with it. That is, we are looking for the mean first passage time for

$$10 \dots 01 \rightarrow 10 \dots 00$$

where the dots represent some chain of down spins. This is done with Markov Chain analysis [23]. Fix a domain of length d , and let P be the transition matrix, where we have implicitly assumed that there is an up spin to the left of the domain that does not relax and we use the convention that P_{ij} is the probability that state i transitions to state j . Notice that this matrix is $2^d \times 2^d$ and sparse since each row can have only as many as $2^{\lfloor d/2 \rfloor}$ nonzero elements, typically much less.

To measure the mean first passage time in question, we make the relaxed state of the system an absorbing state and calculate the mean absorbing time. We can do this because equation (1.125) implies that the real chain is ergodic and this would make the relaxed state the only absorbing state and

connected to all the others, the transient states. We can rewrite the transition matrix P in block form as

$$P = \begin{bmatrix} 1 & 0 \\ R & Q \end{bmatrix} \quad (2.32)$$

where R is a $(2^d - 1) \times 1$ matrix and Q is a $(2^d - 1) \times (2^d - 1)$ ergodic matrix.

It follows that

$$P^n = \begin{bmatrix} 1 & 0 \\ * & Q^n \end{bmatrix} \quad (2.33)$$

where $*$ denotes some nonzero function of Q and R . Since the elements of P^n are the transition probabilities in n steps, and the chain must eventually be absorbed, $Q^n \xrightarrow[n \rightarrow \infty]{} 0$. From this fact, and since $(I + Q + Q^2 + \dots + Q^n)(I - Q) = I - Q^{n+1}$, we have

$$(I - Q)^{-1} = I + Q + Q^2 + \dots \quad (2.34)$$

But it can be shown by equation (2.33) that the elements $(I - Q)^{-1}_{ij}$ are the mean number of times the chain passes through state j before being absorbed given that it starts at state i . Therefore, the mean first passage time is the sum of the elements on the appropriate row of $(I - Q)^{-1}$. Equivalently, it is the appropriate element of the vector $\vec{\tau}$ that is the solution of the linear system

$$(I - Q)\vec{\tau} = \vec{v} \quad (2.35)$$

where \vec{v} is a vector of all ones.

Methods for Solving the system of equations

Again, by simple application of equations (1.114) and (1.115), we can compute P_d , for relatively small values of d . By the Symbolic package in MATLAB, the mean passage time was computed as above for an arbitrary

temperature. Since it is extremely computationally intensive to solve large symbolic systems, the same problem was solved numerically at the specific temperatures that were run in the MC simulations. For moderate length chains, this was done directly, but for larger chains this was done with the GMRES iterative solver up to an accuracy of 10^{-3} or better [50]. This allows us to, for the most part cover at least the same time range that is accessible through MC simulation. The $I - Q$ matrices are in general ill conditioned, so the Jacobi preconditioner was used to speed up the iterative solver.

2.3.2 Markov Chain Multiexponential Model

Next, under the approximation that the up spins are isolated enough that the up spin on the left hand side of the domain does not relax, we can treat the system as if it were a population of independent domains. Let $N(d)$ be the number of sites of length d . By equation (1.118), in equilibrium, $N_{\text{eq}}(d) = Nc(1 - c)^{d-1}$.

In the time domain, what we are interested in is the average fluctuations of the energy from equilibrium, ΔE . Focusing on a single domain length, d , the contribution to ΔE is just $\Delta N(d) = N(d) - N_{\text{eq}}(d)$. The mean time for a domain to relax is τ_d , and since the time rate of change of the number of domains is proportional to how many such domains there are, we can reasonably model this with Debye relaxation for domains of at least size two. For the $d = 1$ case, the relaxation always happens in a single step, so there is no imaginary/loss part to it. Also, for the $d = 2$ case, the relaxation happens in exactly two steps with probability p , there is no loss part in this case either. The individual Debye forms are weighted by how many domains there should

be in equilibrium.

The above argument is summarized as

$$C_V(\omega) = \frac{1}{4T^2 \cosh(1/(2T))} \left(c + pc(1-c) + \frac{(1-p)c(1-c)}{1+i\omega\tau_2} + \sum_{d=3}^{\infty} \frac{c(1-c)^{d-1}}{1+i\omega\tau_d} \right) \quad (2.36)$$

2.3.3 Truncated Markov Chain Multiexponential Model

Equation (2.36) has the advantage of being based only on numerically accurate calculations instead of fitting parameters, but its weakness is that it ignores domain-domain interactions. A simple modification to try to solve this problem is to suppose that there is some maximum relaxation time τ_{\max} and all domains that have an isolated relaxation time longer than the maximum will relax at the maximum time. This happens because domains that are long enough to relax slower than the maximum will be necessarily nonisolated. Therefore, the far left up spin will tend to be relaxed by the adjacent domain in about time τ_{\max} , this will often have the effect of shrinking the domain in question because it will likely have flipped up an intermediate spin, which will become the new terminal left spin for the domain. The exact process of how this happens is complicated, but we can modify the above to incorporate a maximum relaxation time by adding the fitting parameter d_{\max} , the maximum effective domain length, and forcing all domains larger than d_{\max} to relax at its relaxation time.

That is,

$$C_V(\omega) = C_V \left(c + pc(1-c) + \frac{(1-p)c(1-c)}{1+i\omega\tau_2} + \sum_{d=3}^{d_{\max}} \frac{c(1-c)^{d-1}}{1+i\omega\tau_d} + \frac{(1-c)^{d_{\max}}}{1+i\omega\tau_{d_{\max}}} \right) \quad (2.37)$$

where $C_V = 1/(4T^2 \cosh(1/(2T)))$ as in equation (1.113).

For clarity, I will refer to equation (2.36) as the Markov chain model, and equation (2.37) as the truncated Markov chain model.

CHAPTER 3

RESULTS

This chapter presents the raw results of the KWW and HN fits using the method described above as well as the results for the symbolic and numerical versions of the Markov Chain model. The raw dynamic specific heat data from simulation are in Appendix A, this chapter will focus on the fit and model results.

3.1 Simulation

Some general examples of the simulation results have already been shown in the previous chapter's discussion of fitting procedures (see Figure 2.2). The chosen simulation temperature amplitude ΔT and number of sites N did not affect the results of the simulation. The simulations with varying amplitudes were within error bars of each other, but the lower amplitude simulation had considerably more noise in the data (see Figure 3.1). The simulations with varying number of sites were indistinguishable (see Figure 3.2).

3.2 HN and KWW fits

The fits for the example spectra from the previous chapter are shown in Figure 3.3. Both fit the data reasonably well in the low frequency range, but the KWW fit seems to track the high frequency data (that was ignored in the

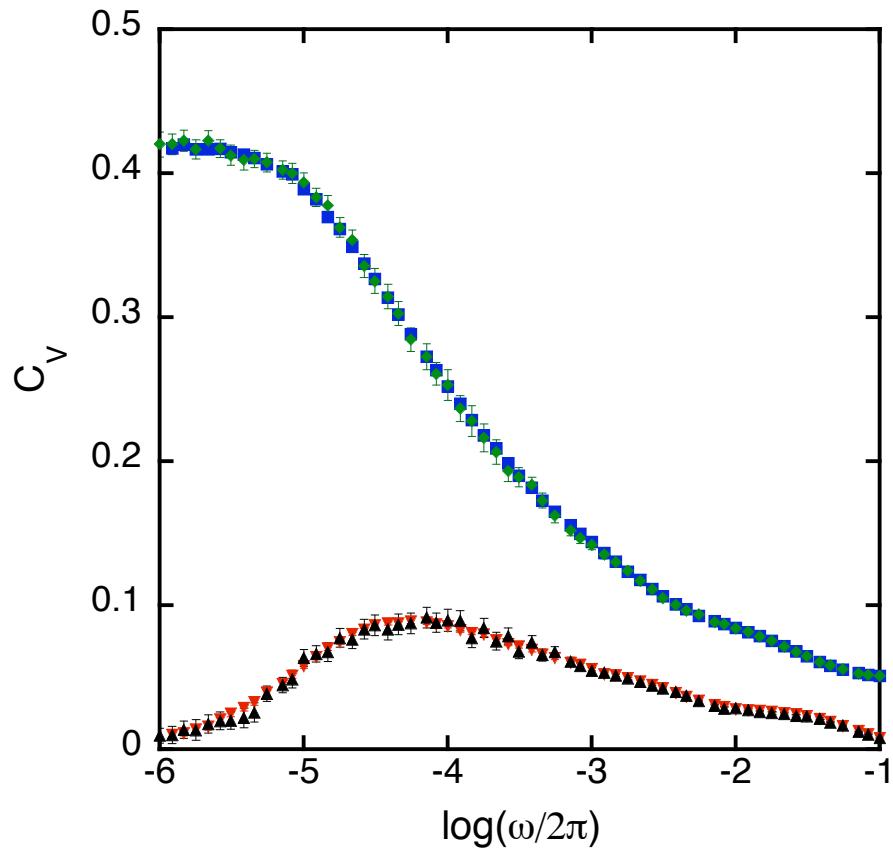


Figure 3.1: Dynamic heat capacity spectrum from simulation with $T_0 = 0.5$ and $N = 100,000$, where $\Delta T = 0.05T_0$ are squares for storage and inverted triangles for loss and $\Delta T = 0.01T_0$ are diamonds for storage and triangles for loss.

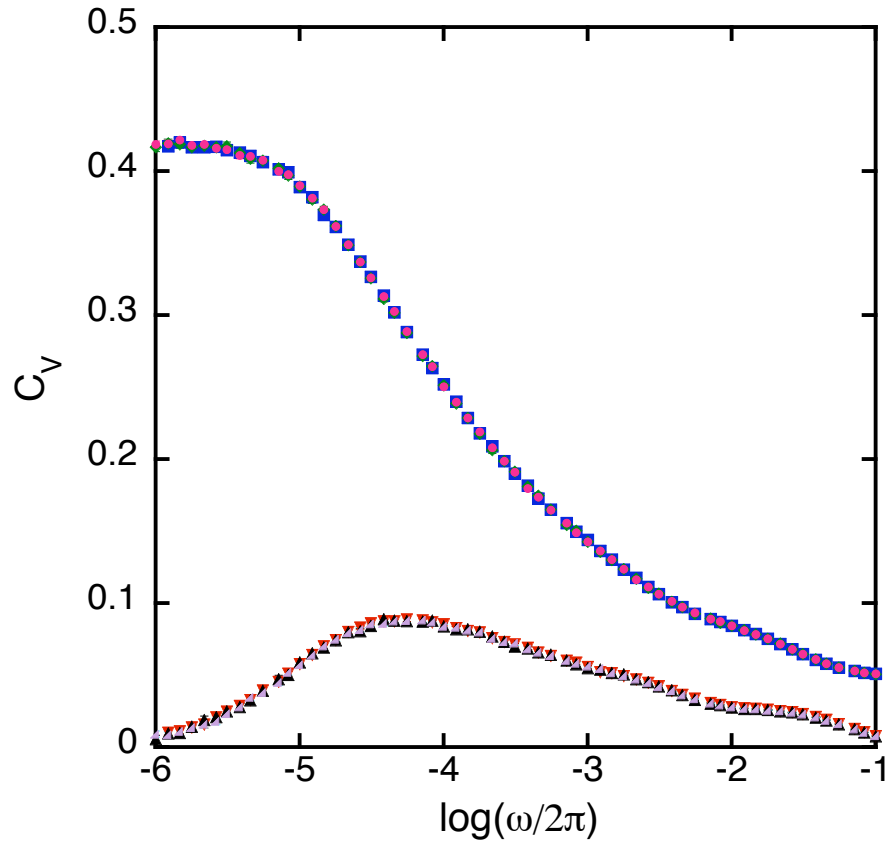


Figure 3.2: Dynamic heat capacity spectrum from simulation with $T_0 = 0.5$ and $\Delta T = 0.05T_0$, where $N = 100,000$ are squares for storage and inverted triangles for loss, $N = 33,001$ are circles for storage and right triangles for loss, and $N = 10,000$ are diamonds for storage and triangles for loss.

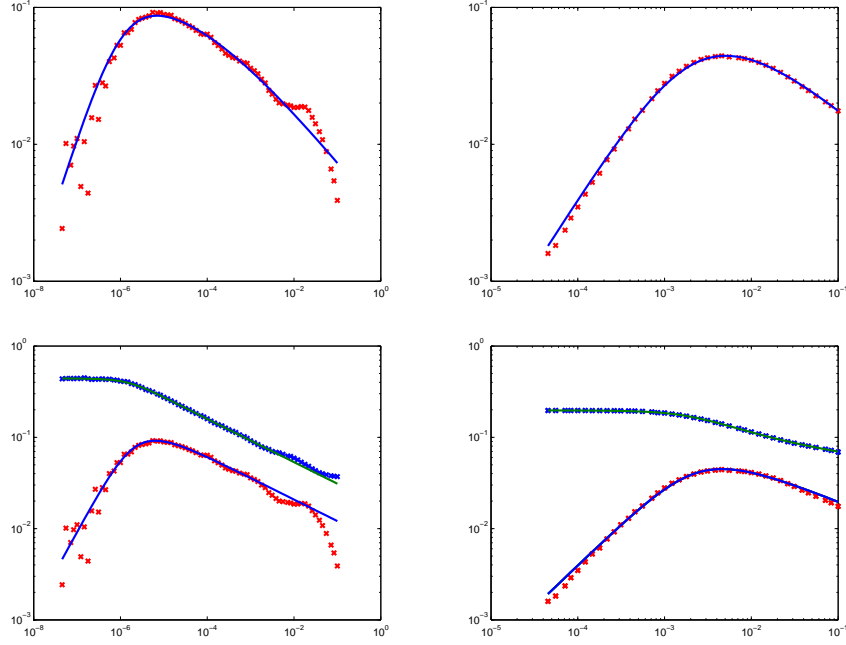


Figure 3.3: Sample nonlinear regression fits for $T = 0.42$ (left) and $T = 1.0$ (right). The KWW fits are on the top and the HN fits are on the bottom. The plot scale is log-log.

actual fitting procedure) better than the HN version.

In analogy to equation (1.52) with equation (1.62), the thermodynamic or zero frequency specific heat is found by summing the shifting C_1 and scaling C_2 parameters. That is,

$$C_{V,0} = C_1 + C_2 \equiv G_0 \quad (3.1)$$

This is a reasonable sanity check on the fits performed, and the result of this can be seen in Figure 3.4. There is good agreement between the theoretical and measured thermodynamic specific heat, with a larger amount of error at low temperatures, where the data is not quite as good due to the large timescales

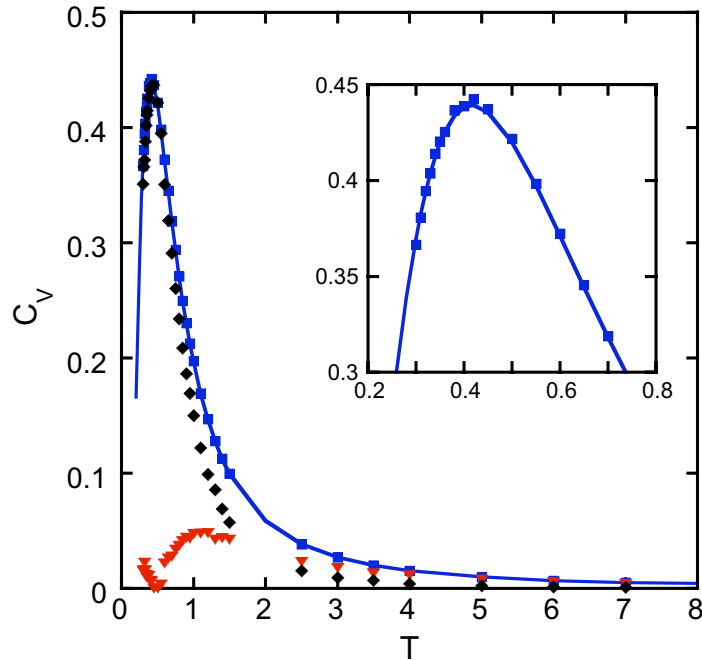


Figure 3.4: Shifting C_1 and scaling C_2 parameters from the HN fits in units of specific heat against temperature. The inverted triangles are the shift factor, the diamonds are the scale factors, and the squares are the sum of those two. The theoretical specific heat, equation (1.113), is the solid line. Inset: zoomed in on the peak with just the sum and equation (1.113) plotted

involved to see the full spectrum. It's also interesting to note that the shifting parameter peaks and then dies off as the shortest relaxation time moves into testable frequencies. The only reason why the shifting factor is necessary is because for the lowest period experiments (10 MC steps per cycle), for higher temperatures, some domains will have relaxed in less time, so we move up the real part of the specific heat to adjust for that.

A similar plot for the KWW fits is the peak height shown in Figure 3.5, but since we have not fit the real part at all, the thermodynamic specific

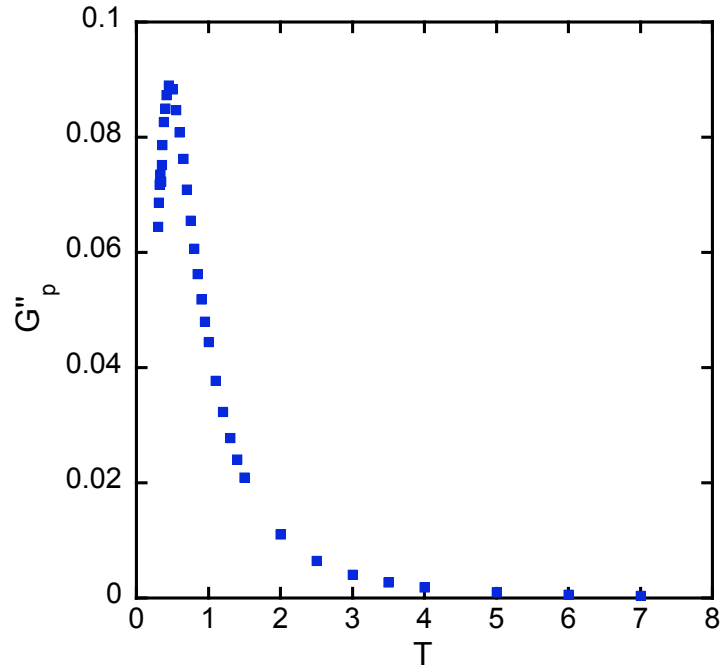


Figure 3.5: Plot of the peak height G''_p from equation (1.94) in units of specific heat against temperature.

heat cannot be recovered from this data, specifically the shifting factor on the real part is missing. The peak height follows the same general shape as the thermodynamic specific heat has a lower value and peaks somewhat earlier, at about $T = 0.45$ instead of about $T = 0.42$.

Next, the fitted shape parameters are shown in Figure 3.6. For either fitting procedure, we see two plateaus and a relatively smooth transition between them. For high temperatures, all three parameters are approximately one, meaning the relaxation is nearly Debye. Then for low temperature, high τ , b and γ decrease and plateau to a somewhat low value, indicating non-Debye relaxation stretched over more and more timescales. γ seems to have reached

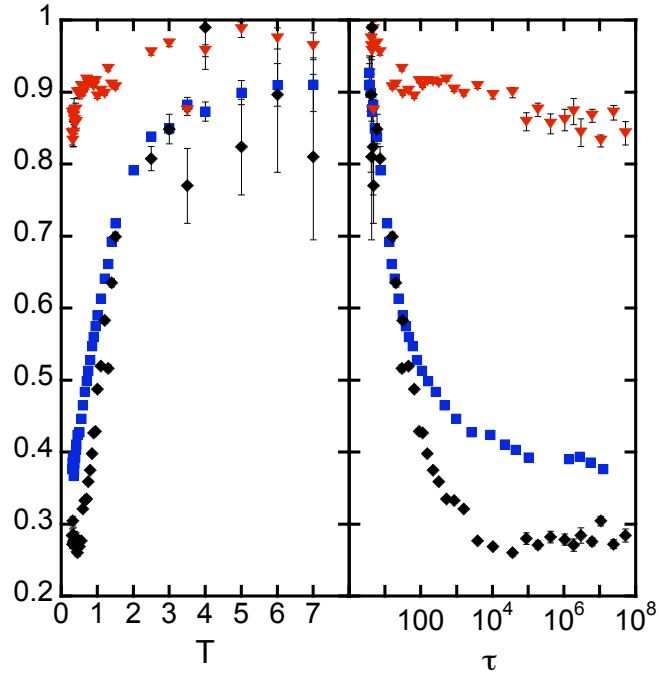


Figure 3.6: Shape parameters α (inverted triangles), γ (diamonds), and b (squares) plotted against temperature (left) and $\log(\tau)$ from the same type of fit (right) with fitting error bars.

a plateau of a bit under 0.3 in the temperatures studied, but it is unclear what the KWW b 's eventual behavior is.

Finally, comparing \log time against inverse temperature squared (see Figure 3.7), for low temperatures, the data seems to be approaching a straight line, as is expected from equation (1.125). Note that we only expect agreement for low temperatures since the theories of Sollich and Evans, Aldous and Diaconis, and Cancrini et. al. only apply in the low temperature limit (see Chapter 1). Therefore, we fit the relaxation time at low temperature with equation (1.3). For HN this results in $\tau_0 = 171.47 \pm 21.906$ and $B = 1.136 \pm 0.013045$,

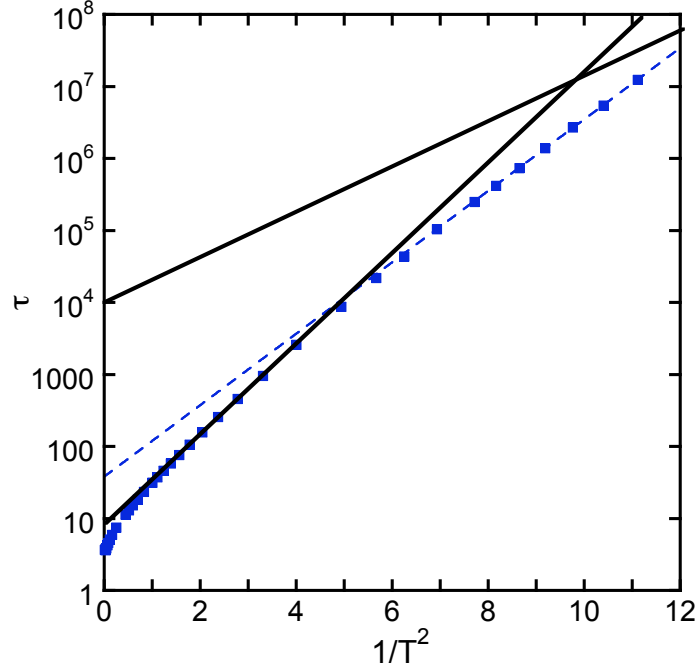


Figure 3.7: Plot of log relaxation time τ against inverse temperature squared for the KWW fits (squares). The dashed lines are the fits to the EITS form discussed in the text. The solid lines are for comparison to the theoretical slopes of $1/\ln 2$ and $1/2 \ln 2$.

and for KWW $\tau_0 = 38.094 \pm 3.0373$ and $B = 1.1425 \pm 0.0081525$. This is statistically significantly smaller than the Sollich and Evans value of $B = 1/\ln 2 \approx 1.4427$ from equation (1.125) and larger than the Cancrini et. al. value of $B = 1/2 \ln 2 \approx 0.7213$ from equation (1.128). The large difference between the τ 's from the HN and KWW, especially at low temperatures, comes from the fact that the shape parameters (α , γ , and b) in this range are low; this changes the relative peak location and τ value for both functions and is a well known property of these functions [2]. Although the exact numerical value for τ is different, both methods have similar asymptotic behavior for low temperature.

3.3 Markov Chain Model

The two parts discussed are the symbolic and numerical values for τ_d and the resulting specific heat spectra.

3.3.1 Symbolic Results

The first four symbolic τ_d 's as a function of flip probability p , in full form are

$$\tau_1 = 1 \tag{3.2}$$

$$\tau_2 = \frac{p+1}{p} \tag{3.3}$$

$$\tau_3 = \frac{-2p + p^3 - 1}{p^2(-1+p)} \tag{3.4}$$

$$\tau_4 = \frac{p^9 - 2p^7 + 5p^6 + 8p^5 - 5p^4 - 9p^3 + 2p^2 + 6p + 2}{p^2(p^7 - p^6 - p^5 + 3p^4 - 3p^2 + p + 1)} \tag{3.5}$$

It gets much more complicated from there, so the truncated series representation for the first eight are

$$\tau_1 = 1 \tag{3.6}$$

$$\tau_2 = p^{-1} + 1 \tag{3.7}$$

$$\tau_3 = p^{-2} + 3p^{-1} + 3 + \mathcal{O}(p) \tag{3.8}$$

$$\tau_4 = 2p^{-2} + 4p^{-1} + 4 + \mathcal{O}(p) \quad (3.9)$$

$$\tau_5 = \frac{1}{2}p^{-3} + \frac{15}{4}p^{-2} + \frac{71}{8}p^{-1} + \frac{163}{16} + \mathcal{O}(p) \quad (3.10)$$

$$\tau_6 = \frac{6}{7}p^{-3} + \frac{37}{7}p^{-2} + \frac{90}{7}p^{-1} + \frac{818}{49} + \mathcal{O}(p) \quad (3.11)$$

$$\tau_7 = \frac{3}{2}p^{-3} + \frac{27}{4}p^{-2} + \frac{289}{12}p^{-1} + \frac{751}{144} + \mathcal{O}(p) \quad (3.12)$$

$$\tau_8 = 4p^{-3} - 40p^{-2} + \frac{2509}{2}p^{-1} - \frac{477655}{16} + \mathcal{O}(p) \quad (3.13)$$

Unfortunately, this as far as could be computed in a reasonable time frame. This does, however, give strong evidence for the truth of the approximation by Evans in equation (1.122) [14]. There is no obvious pattern for even the leading coefficient, and solving that problem, if there is a solution, for the p^{-n} terms would essentially completely determine the dynamics of the east model.

Interestingly, running the Markov Chain analysis in the reverse direction, that is the mean first passage time from relaxed to two isolated up spins of a specific domain size d , yields that the creation time for a domain of size d is

$$\tau_{\text{create},d} = \frac{\tau_d}{p} \quad (3.14)$$

for all the domain lengths probed symbolically.

3.3.2 Numerical Results

Examples of the results of the Markov Chain model are shown in Figures 3.8, 3.9, 3.11, 3.12, and 3.13. Where the primary result of this model is that we are able to fit the wobbles on the high frequency side that were impossible to treat with just the HN or KWW functions.

For low temperatures (below $T = 0.3$), such as $T = 0.2$ and 0.25 in Figures 3.8 and 3.9, the Markov Chain model is able to capture the entire behavior of the dynamic specific heat that was possible to simulate with Monte Carlo. Computing the full spectrum with Monte Carlo at these temperatures is well beyond what is possible to do with today's computers, so we cannot compare this model with simulation any further than that. Note how far from equilibrium frequencies these cases are: for $T = 0.2$, $C_V \approx 0.166$ by equation (1.113), but the real part of the simulation results only goes as high as 0.01; and for $T = 0.25$, $C_V \approx 0.283$, but the real part only gets as high as 0.07 in the simulation.

Next, in the intermediate cases (temperatures between $T = 0.3$ and $T = 0.5$ or so), such as $T = 0.32$ and $T = 0.42$ in Figures 3.11 and 3.11, the full spectrum can be simulated, and the problem here is the number of Markov Chain τ_d 's that can be computed. For the range that it is possible to compute enough τ_d 's the agreement is very good, but there are diminishing returns from equation (2.36), where each successive term matters less but is several times harder to compute. The result is promising, and explains the high frequency structure, but is incomplete. A near-infinite number of terms would be required to fill this out.

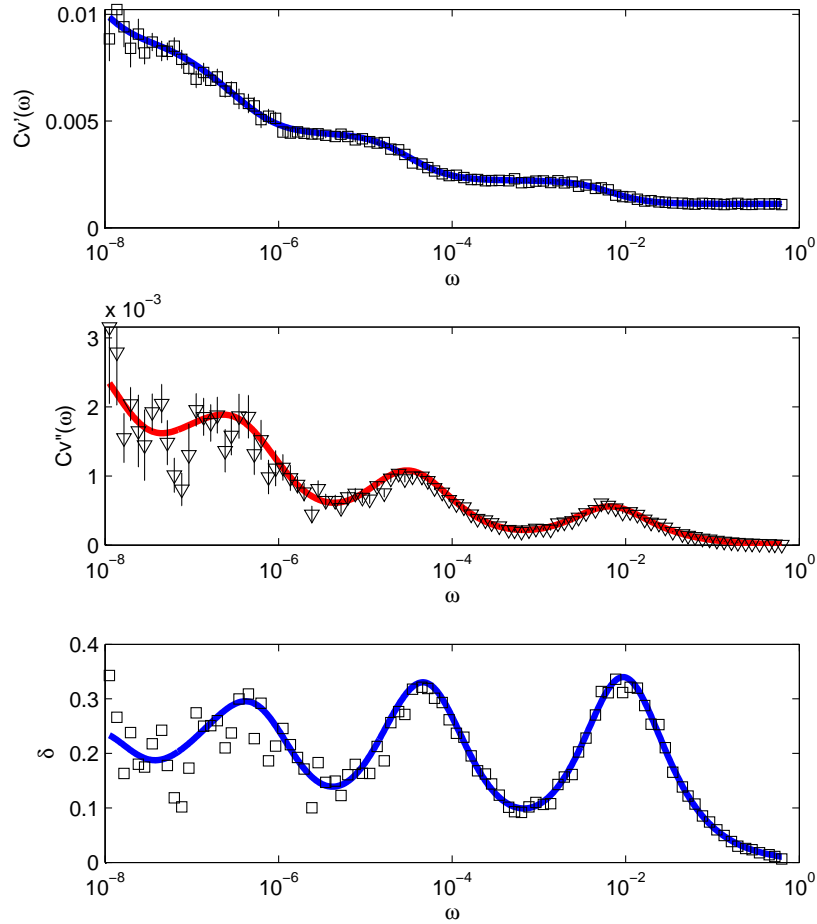


Figure 3.8: Sample Markov chain model (lines) compared to the MC data for $T = 0.2$. The top (squares) is the real part and the middle (inverted triangles) is the imaginary part of the dynamic heat capacity. The bottom is the phase lag δ . The model was computed with τ_d 's for domains with sizes up to $d = 14$.

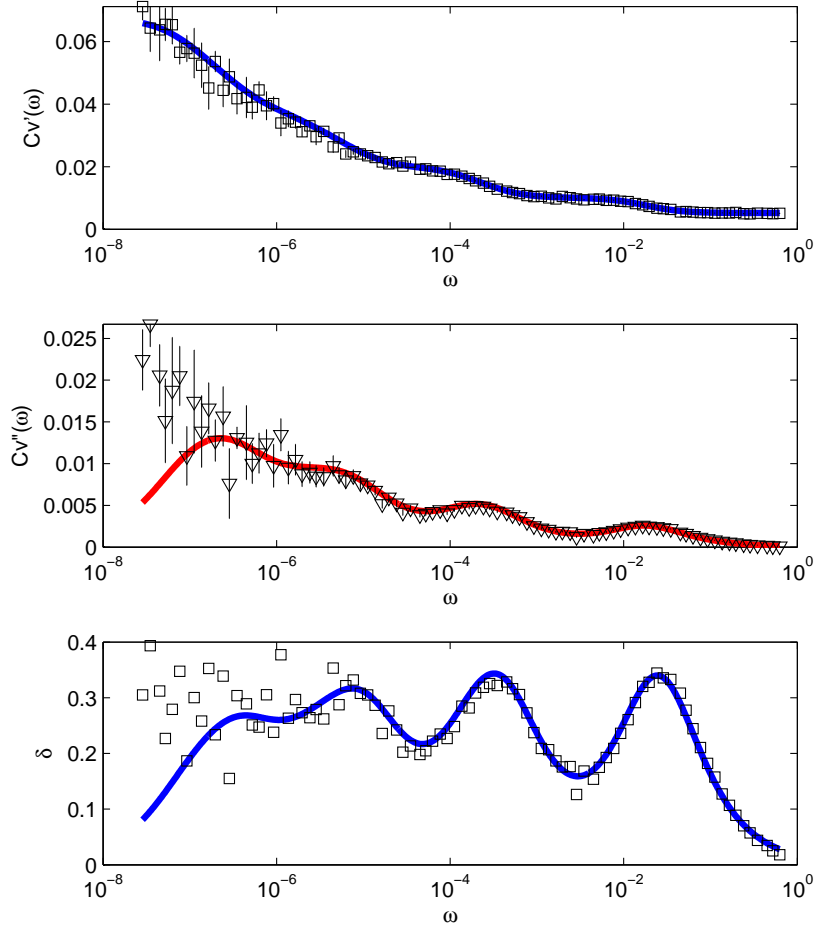


Figure 3.9: Sample Markov chain model (lines) compared to the MC data for $T = 0.25$. The top (squares) is the real part and the middle (inverted triangles) is the imaginary part of the dynamic heat capacity. The bottom is the phase lag δ . The model was computed with τ_d 's for domains with sizes up to $d = 12$.

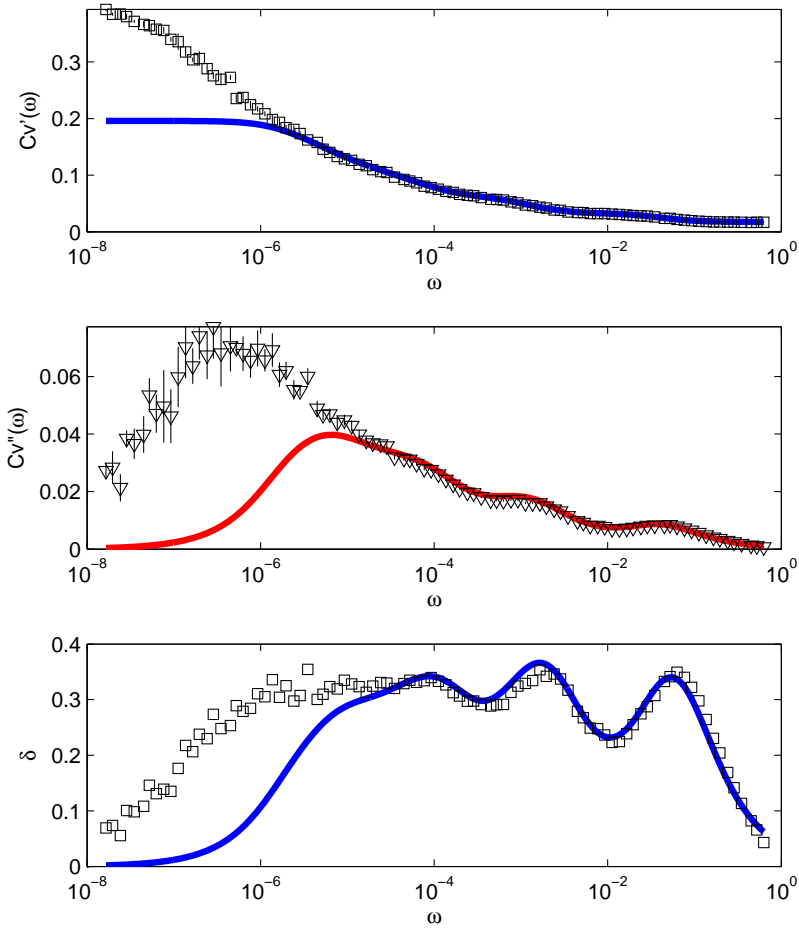


Figure 3.10: Sample Markov chain model (lines) compared to the MC data for $T = 0.32$. The top (squares) is the real part and the middle (inverted triangles) is the imaginary part of the dynamic heat capacity. The bottom is the phase lag δ . The model was computed with τ_d 's for domains with sizes up to $d = 16$.

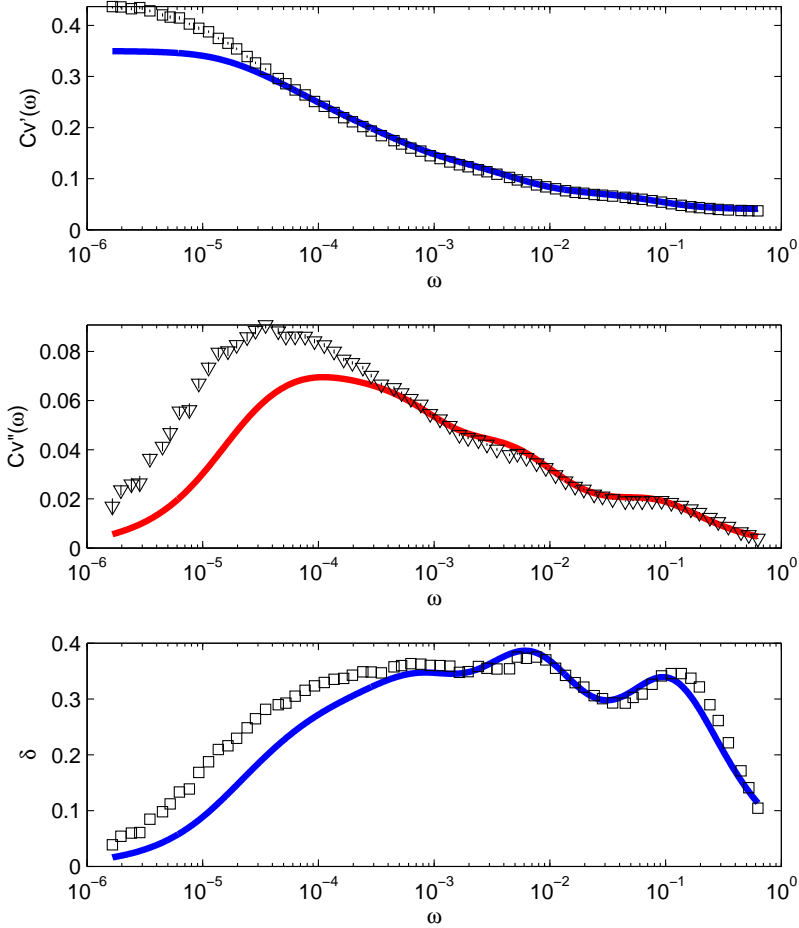


Figure 3.11: Sample Markov chain model (lines) compared to the MC data for $T = 0.42$. The top (squares) is the real part and the middle (inverted triangles) is the imaginary part of the dynamic heat capacity. The bottom is the phase lag δ . The model was computed with τ_d 's for domains with sizes up to $d = 18$.

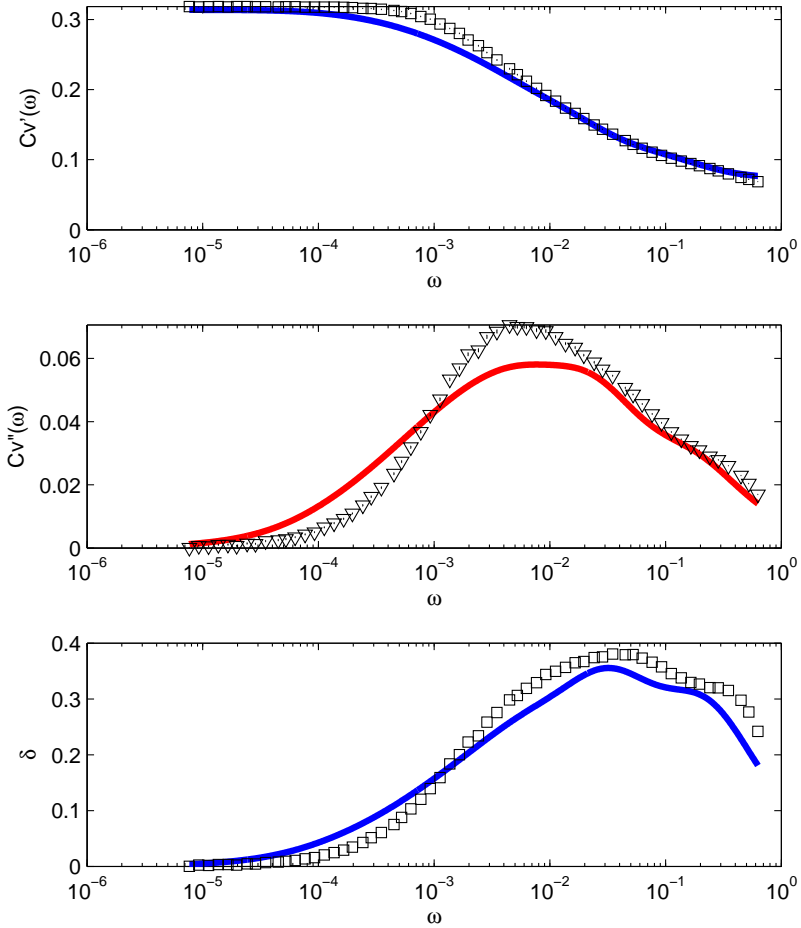


Figure 3.12: Sample Markov chain model (lines) compared to the MC data for $T = 0.7$. The top (squares) is the real part and the middle (inverted triangles) is the imaginary part of the dynamic heat capacity. The bottom is the phase lag δ . The model was computed with τ_d 's for domains with sizes up to $d = 20$.

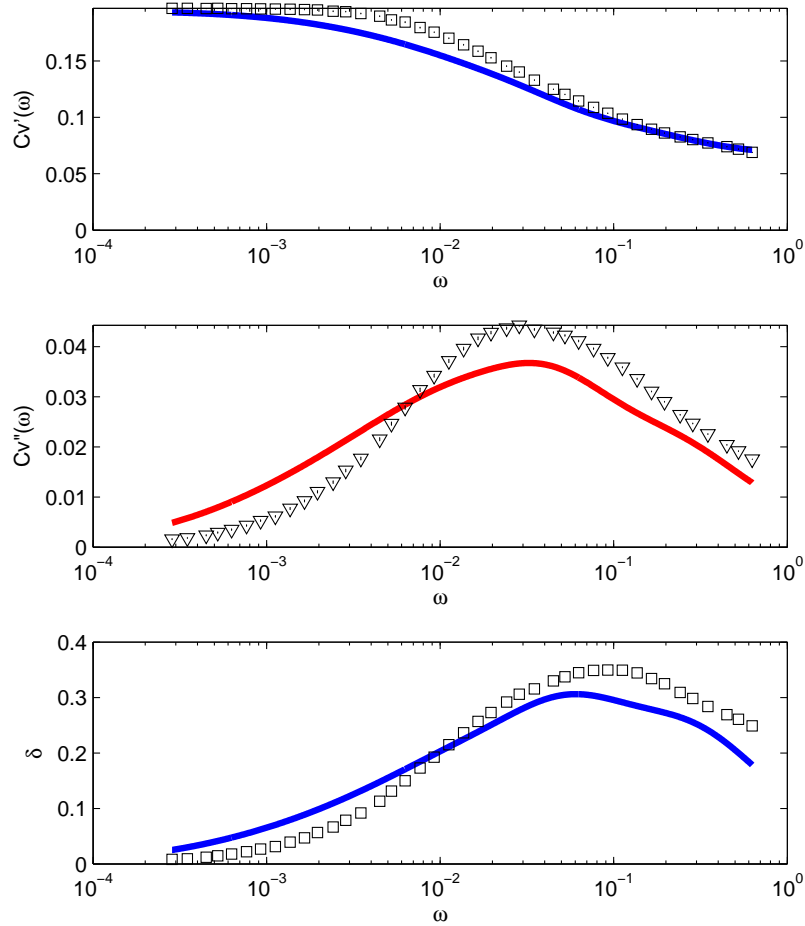


Figure 3.13: Sample Markov chain model (lines) compared to the MC data for $T = 1.0$. The top (squares) is the real part and the middle (inverted triangles) is the imaginary part of the dynamic heat capacity. The bottom is the phase lag δ . The model was computed with τ_d 's for domains with sizes up to $d = 14$.

Finally for high temperatures (above about $T = 0.5$), such as $T = 0.7$ and 1 in Figures 3.12 and 3.13, both the full dynamic heat capacity spectrum is able to be simulated and enough τ_d 's are able to be computed to cover the full range of dynamics. Here, however, there is not as much of a good fit. The prediction of the Markov Chain model shows a C_V spectrum that is too spread out, as a result of the domains actually being completely nonisolated for higher temperatures.

Truncated Markov Chain Numerical Results

We can do better with the truncated Markov chain version, equation (2.37). This fills out the relaxation for domains too large to compute the relaxation for directly, and crops off any relaxation times that are too long by forcing them down to the best fit d_{\max} . Figures 3.14, 3.15, and 3.16 are the truncated Markov chain model fits for $T = 0.42$, 0.7, and 1. Again, we are limited by the number of terms that can be computed, and it was only possible to do this analysis in the temperature range $0.42 \leq T \leq 1$.

Since d_{\max} is a fitting parameter, tracking it tells us something about the system as well, See Figure 3.17. d_{\max} seems to grow approximately proportionately to the mean domain length.

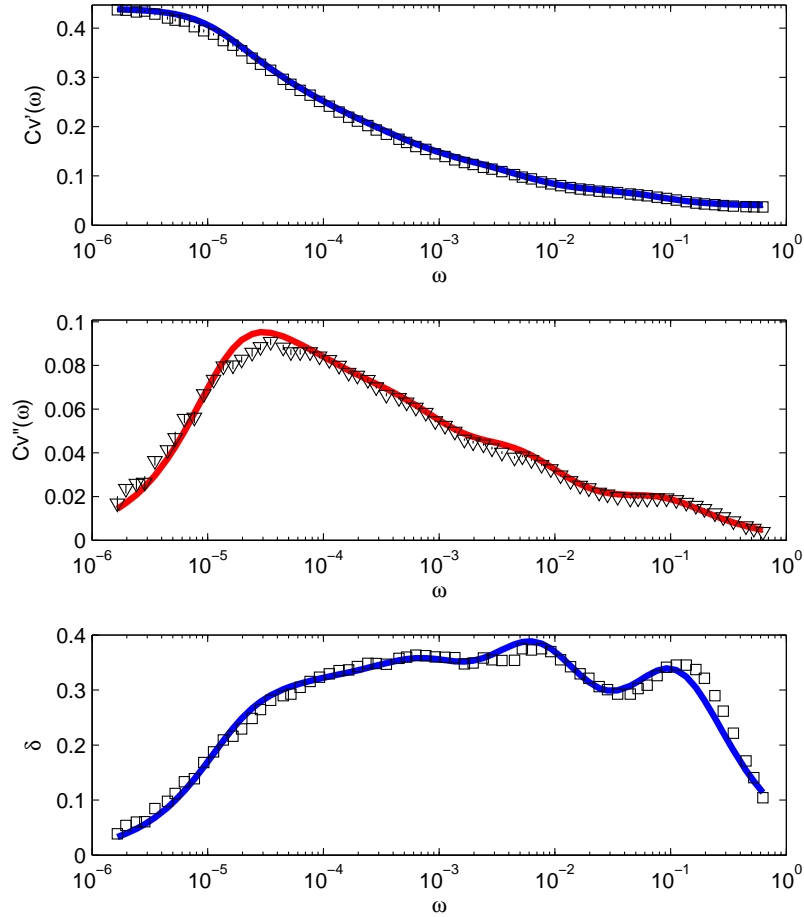


Figure 3.14: Sample truncated Markov chain model (lines) compared to the MC data for $T = 0.42$ with $d_{\max} = 18$. The top (squares) is the real part and the middle (inverted triangles) is the imaginary part of the dynamic heat capacity. The bottom is the phase lag δ .

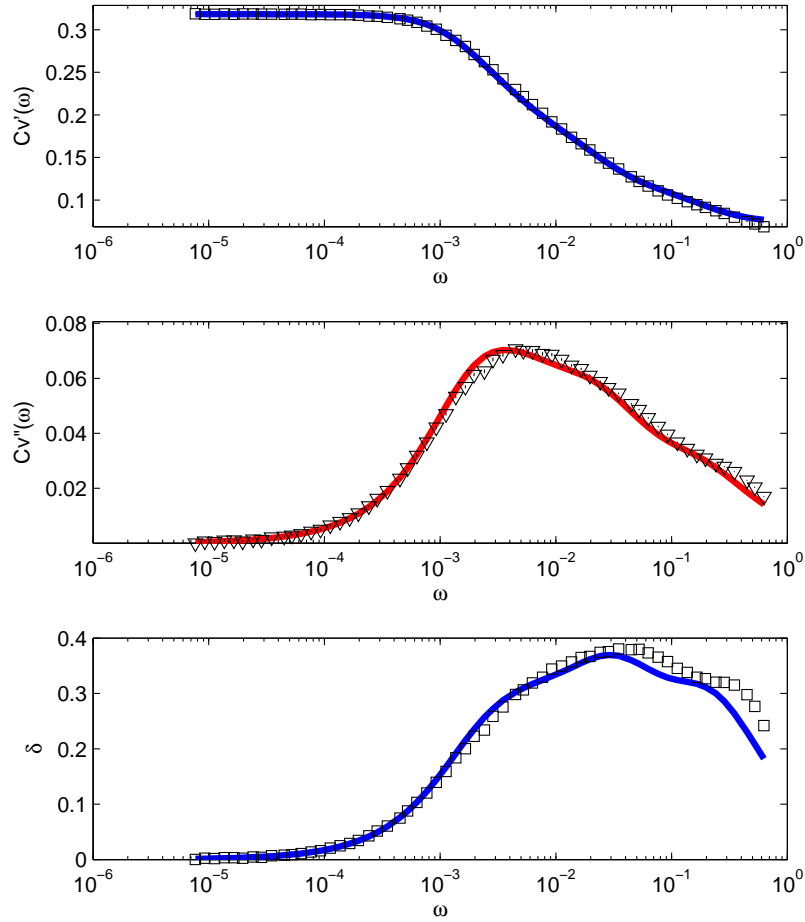


Figure 3.15: Sample truncated Markov chain model (lines) compared to the MC data for $T = 0.42$ with $d_{\max} = 8$. The top (squares) is the real part and the middle (inverted triangles) is the imaginary part of the dynamic heat capacity. The bottom is the phase lag δ .

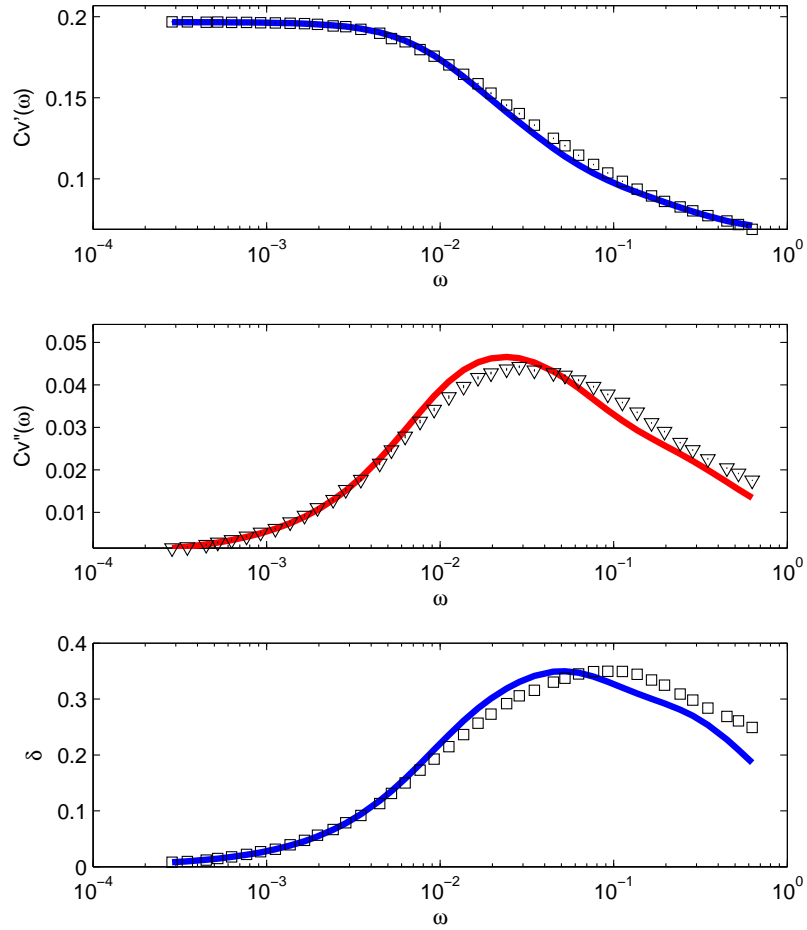


Figure 3.16: Sample truncated Markov chain model (lines) compared to the MC data for $T = 0.42$ with $d_{\max} = 5$. The top (squares) is the real part and the middle (inverted triangles) is the imaginary part of the dynamic heat capacity. The bottom is the phase lag δ .

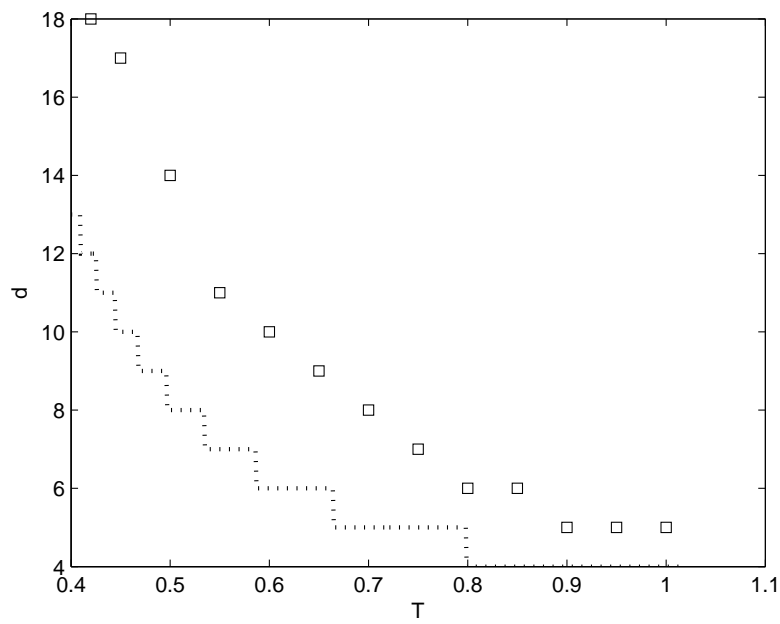


Figure 3.17: Plot of domain length vs. temperature. The squares are the best fit d_{\max} . The dotted line is the mean domain length.

CHAPTER 4

DISCUSSION

4.1 Simulation

In the previous chapters, we saw that the dynamic heat capacity of the east model could be measured using Monte Carlo simulation by comparing the sinusoidally varying temperature with the resultant sinusoidally varying energy. The resultant spectra for fixed temperatures and widely varying frequencies in and of themselves are somewhat of a new result for the east model. However, the mathematically equivalent time domain version of the dynamic heat capacity, spin autocorrelation functions, have been measured many times before and used as a primary tool for analyzing relaxation behavior in the model [31, 13, 53, 47, 48]. The wiggles in the short time spin autocorrelations in these papers correspond to the wiggles in the storage and peaks in the loss seen in this study for low temperatures. In neither case does a stretched exponential fully explain the behavior.

4.2 KWW and HN

As mentioned above, the fits of the simulation data to the KWW or HN forms are not strictly valid because there are features in the data that simply do not exist in the KWW or HN functional forms. However, by avoiding the trouble spots, we can come up with estimates for the relaxation time τ and

the shape parameters α , γ , and b give more information on how the system relaxes.

First, as mentioned in the previous chapter, for the HN fits, where we fit the real part of the dynamic heat capacity which asymptotically approaches the thermodynamic heat capacity, we confirm the validity of fits by recovering the thermodynamic specific heat (see Figure 3.4).

τ is a trickier subject. The fitted τ 's asymptotically approach the EITS form, which is agreed to be the theoretical limit. However, when the value for B in the EITS form, equation (1.3), is fit to the computed τ 's, the error is very large compared to what would be expected from the accuracy of the data and the fits. See Figure 3.7. There are several possible reasons for this difference. First and foremost, this could be approaching the more recently established value of $B = 1/2 \ln 2$, but the simulations were not done at cold enough temperatures to see this.

There is also the possibility that the lowest temperature fits are somewhat flawed. A large potential problem resides in the cropping step in the fit; for the coldest half of the temperatures that could be fit there is at least one high frequency peak that has to be cropped off, and for the coldest 9 temperatures there are two peaks that have to be cropped off. Cropping the high frequency side of things at somewhat arbitrary data points could greatly affect the shape parameters, which are determined by high frequency data (see Chapter 1), and this could have a very large effect on the eventually fitted τ 's since the parameters are related in a nontrivial matter [2]. For lower and lower temperatures, less and less of the high frequency data is reasonably fit

by these functions, leading to a potentially very large error that is not directly accounted for.

The shape parameters α , γ , and b drop with decreasing temperature; meaning a more spread out relaxation function. This supports the idea that the system does not have a single relaxation that gets slower with temperature (as in time temperature superposition), but potentially many relaxations that get slower with temperature at different rates. The Markov Chain model explains how and why this happens.

4.3 Markov Chain

The results of the Markov Chain model have two important consequences.

First, the symbolic solutions, to first order, agree with the approximation that gives rise to the form of the overall relaxation time of the system due to Sollich and Evans, namely that $\tau_d \propto p^{-n}$ where $2^{n-1} < d \leq 2^n$ [53, 14]. This relationship, in effect, explains the decrease we see in the shape parameters in the KWW and HN fits because for low temperatures, $p = \exp(-1/T)$ becomes very small making the difference between p^{-n} and $p^{-(n+1)}$ very large. However, it remains an open question as to a general form for the τ_d 's. The exact form is extraordinarily complicated; τ_8 is a ratio of two roughly 250 degree polynomials. But, the p^{-k} , $k \geq 0$, are the important terms in the low temperature limit, so finding a pattern in these terms would be enough to essentially nail down the entire relaxation function for low temperature and domain size.

Secondly, we see that the numerical Markov Chain results match the

simulation data very well for high frequencies, where the high frequency wiggles in the dynamic heat capacity (and therefore also the short time wiggles in the spin autocorrelation) are matched perfectly by this model. This model for the relaxation function relies only on the approximation that the relaxation of the individual domains is Debye, which is only approximately true. The biggest problems with that approximation will be in extremely short timescales, where the discrete nature of the model is more important, but especially at low temperatures when timescales become much larger, this approximation is valid for most of the dynamic heat capacity spectra.

Since these relaxation times for low temperature become significantly spread out as to become distinct in the C_V spectra, we are able to compute these times numerically and exactly and match this with simulation in a meaningful way. That is, if all relaxations were lost in a single peak, fitting relaxation time is an underdetermined problem greatly complicated by data noise, but since we see the peaks separate for low temperatures, we can tell that the model relaxation times work.

A weakness of this model for long timescales is the assumption of domain isolation. Short domains are essentially isolated since, especially for low temperatures, they have a considerable lower relaxation time than the average domain, so the local dynamics are as if no other up spins exist to the left of the terminal left spin. For very long domains, the terminal left up spin is likely to be flipped down by the adjacent domain at some point. Now, recalling that $\tau_d = \mathcal{O}(p^{-n})$ and $\tau_{\text{create},d} = \mathcal{O}(p^{-(n+1)})$, the interdomain dynamics are composed of slow creation and rapid collapse of small subdomains, which occasionally

extends out far enough to relax the terminal right up spin. So, when the left terminal up spin in a long domain relaxes, this speeds up the dynamics because the subdomains can not collapse as far back. This is complicated by the fact that if no subdomains exist or they are relaxed as well, the domain is absorbed into the domain to its left, increasing relaxation time. This is why the isolated model works great for short timescales (and thus small domains) at low temperature (see Figures 3.8 and 3.9), but for higher temperatures where we should be able to cover the entire simulation range with the Markov chain model, it is too spread out (see Figures 3.12 and 3.13).

The truncated version of the Markov chain model does a remarkably good job fitting the data and fixing the problems of the isolated domain model (see Figures 3.14, 3.15, and 3.16). However, it requires a fitting parameter, and rigidly cutting down the long relaxation times to a single value is unrealistic. To do this right, one would need to find a way to spread out the contribution of the larger domains over shorter timescales in a way based more firmly on the dynamics of the east model.

4.4 Summary

The first main result of this work is based on Monte Carlo simulations of the east Ising model; we can compute the dynamic heat capacity of the model and fit it to relaxation functions to extract relaxation time and form. The relaxation time is seen to fit the general form that it should from theoretical arguments from the literature.

Secondly, we make a connection between the rules of the east model

and its structure (domains of down spins with up spin on either side) to a Markov chain model of those domains to get a discrete set of relaxation times. These relaxation times explain the shape of the dynamic specific heat spectra at low temperature and high frequency. Also, recall that the Markov Chain model is essentially an expansion of the work of Sollich and Evans, which leads to $\tau \propto \exp(1/T^2 \ln 2)$ for low temperatures, the isolated domain limit. However, in our Monte Carlo simulations, we find that $T^2 \ln \tau \approx 1/1.3 \ln 2$ at the lowest temperatures, which is consistent with domain-domain interactions introducing faster dynamics.

A full description of the dynamics would require us to model the domain-domain interactions. Such a model would speed up the relaxation times based on the (probabilistic) size of the domain to the left. This would result in a gradual isolated/nonisolated domain transition, where timescales near the relaxation time of the median domain size would dominate the long time behavior. Since simply plugging in the mean (or median) domain size into $\tau_d \approx p^{-n}$ results in $\tau \propto \exp(1/T^2 \ln 2)$, a more general form of τ_d (perhaps derived from the isolated Markov Chain method used above) with correct coefficients and second order terms (effectively spreading out the domain relaxations across the relevant powers of 2) might need to be used to agree with $\tau \propto \exp(1/T^2 \ln 2)$. Note that the HN fits show $\alpha < 1$ especially for low temperatures, supporting these ideas.

In a broader sense, the whole purpose of the East model is to replicate a real system. For a remarkable number of real systems and experiments, we see relaxations that for at least certain timescales appears to be stretched

exponential, or in the frequency domain HN. For these functions to be exactly correct, this would require that there was a continuous distribution of relaxation times in the system; a claim that is not necessarily physical [39, 2]. Discrete models, such as the east model, also show relaxation behavior that, for certain timescales at least, is very similar to the KWW or HN forms, but since they are discrete we do not need to invoke a continuous distribution of relaxation times to generate them. It is not such a huge leap to suppose that a similar mechanism is at work in real systems as well. That is, certain jammed structures have certain (temperature dependent) times associated with them and the sum of all their relaxations give rise to the macro level experimental results. What exactly these are, and how they evolve with time is a much more complicated question.

APPENDIX A

RAW SIMULATION DATA

The following are plots of the results for C_V at all simulated frequencies and temperatures. All horizontal axes are the same, but the vertical axes for the dynamic heat capacity are set to the maximum real part measured (often the thermodynamic limit).

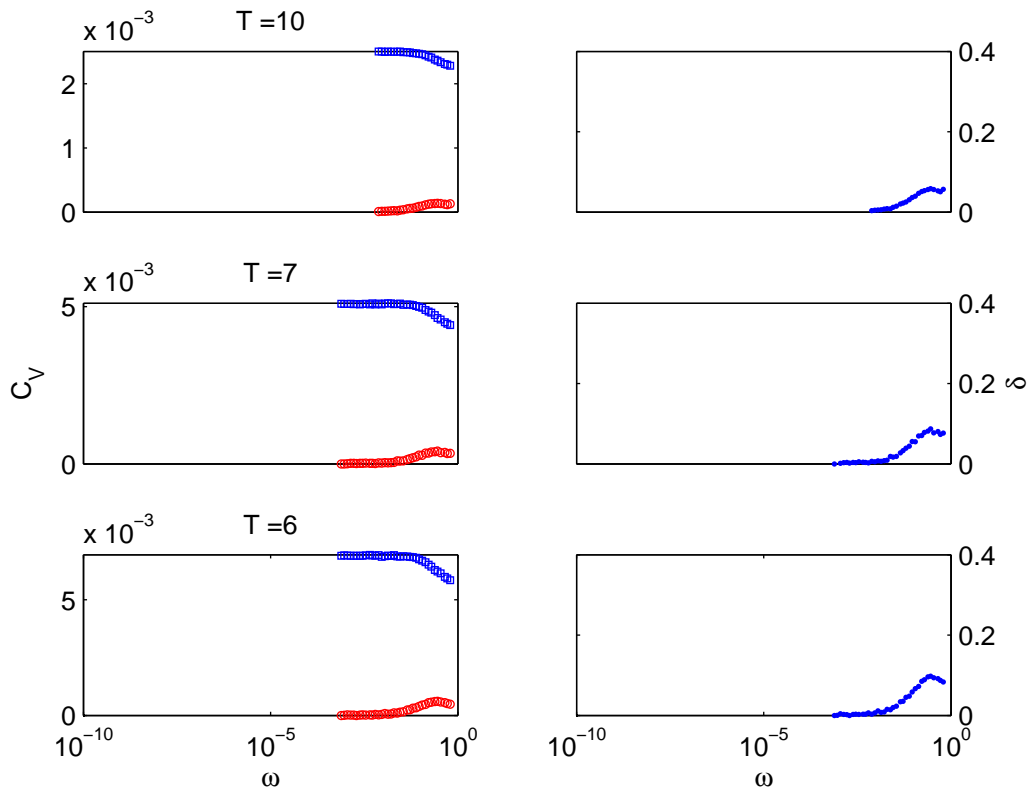


Figure A.1: C_V' (squares), C_V'' (circles), and δ (points) from simulations at the marked temperatures.

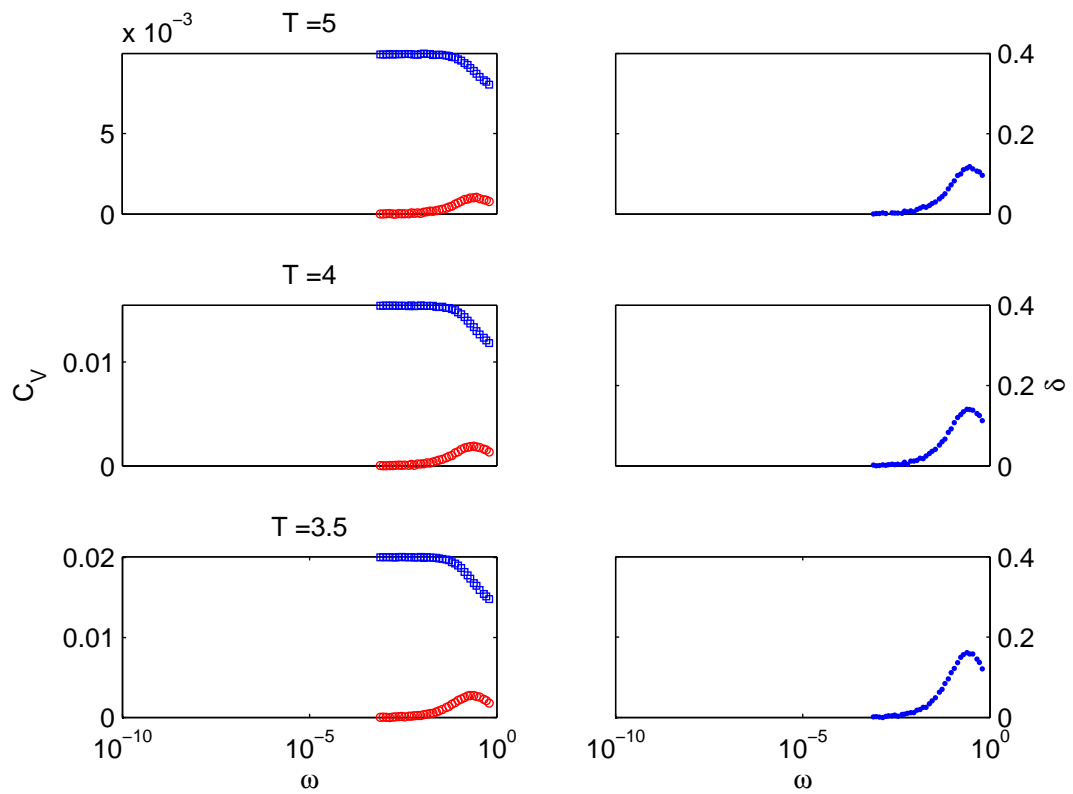


Figure A.2: C_V' (squares), C_V'' (circles), and δ (points) from simulations at the marked temperatures.

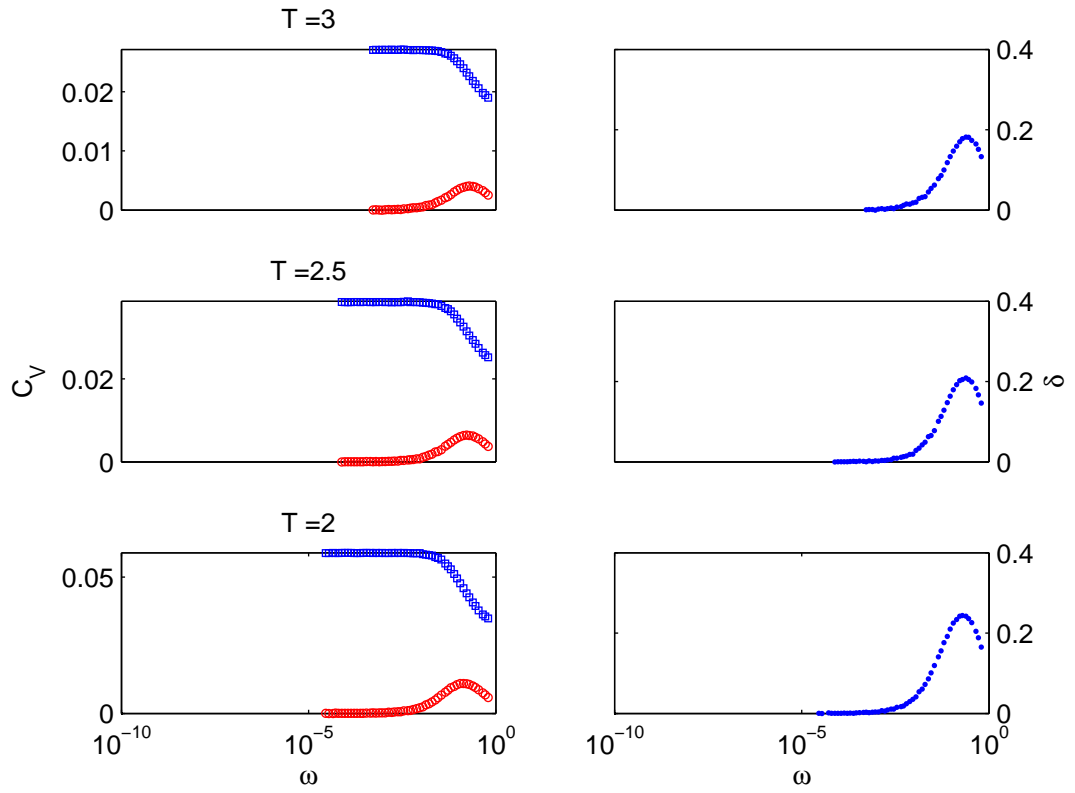


Figure A.3: C_V' (squares), C_V'' (circles), and δ (points) from simulations at the marked temperatures.

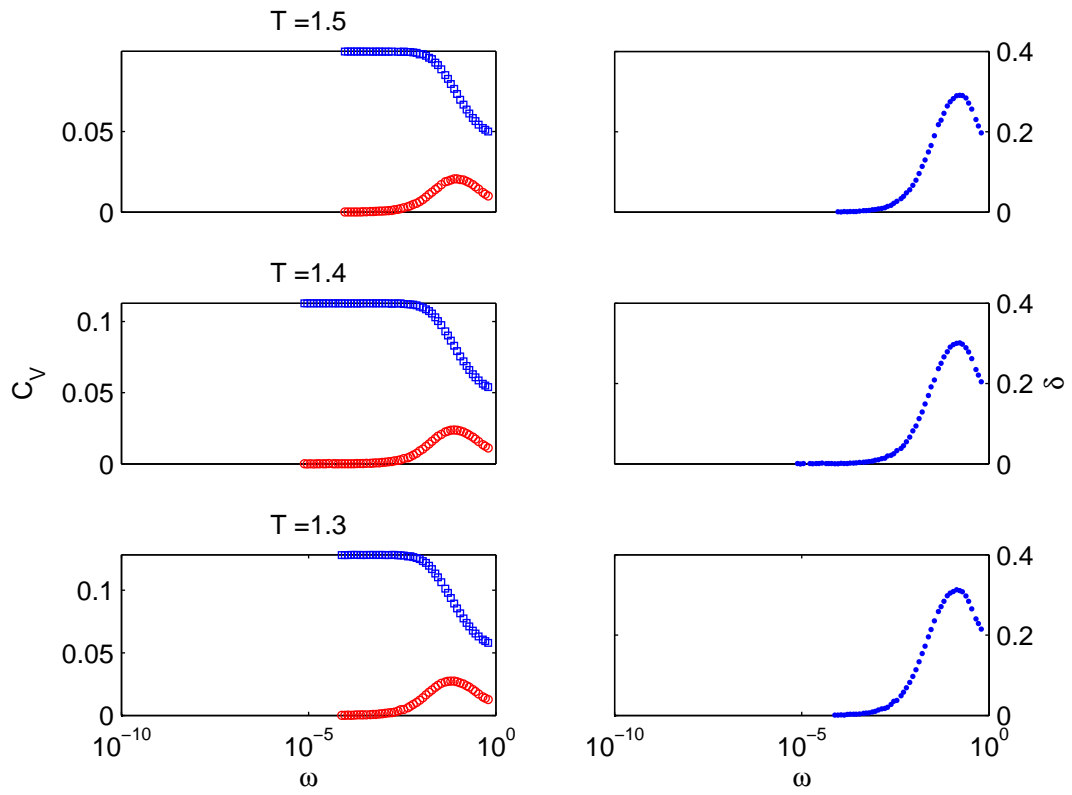


Figure A.4: C_V' (squares), C_V'' (circles), and δ (points) from simulations at the marked temperatures.

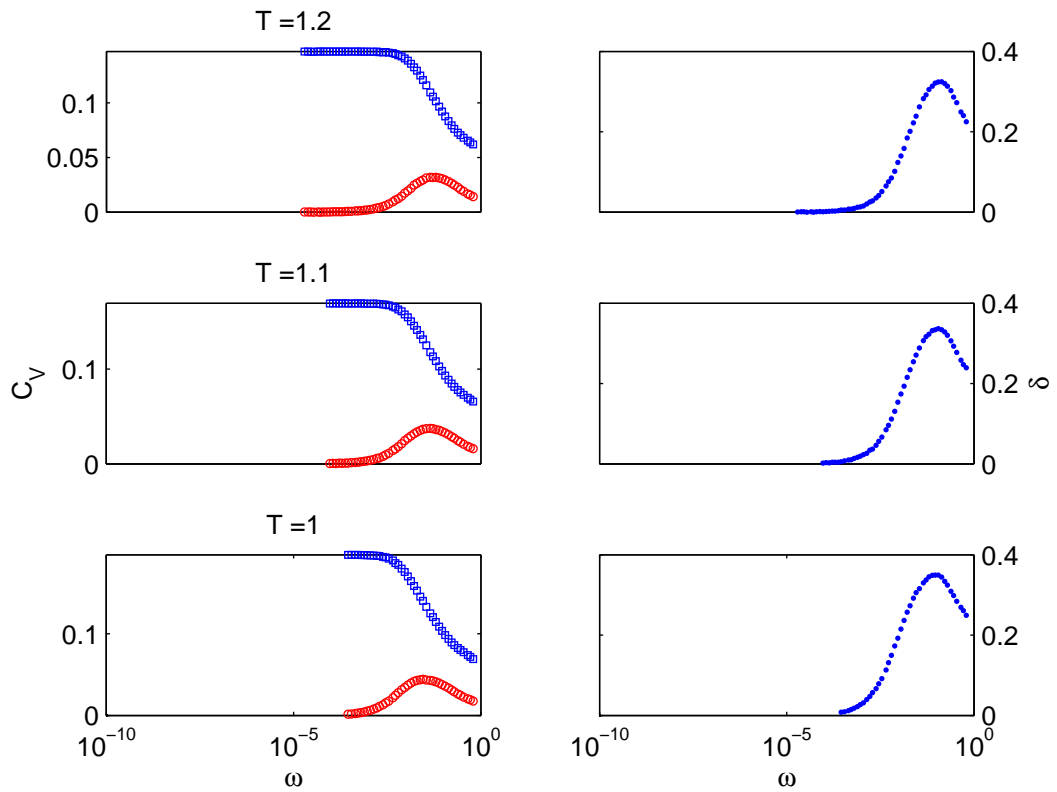


Figure A.5: C_V' (squares), C_V'' (circles), and δ (points) from simulations at the marked temperatures.

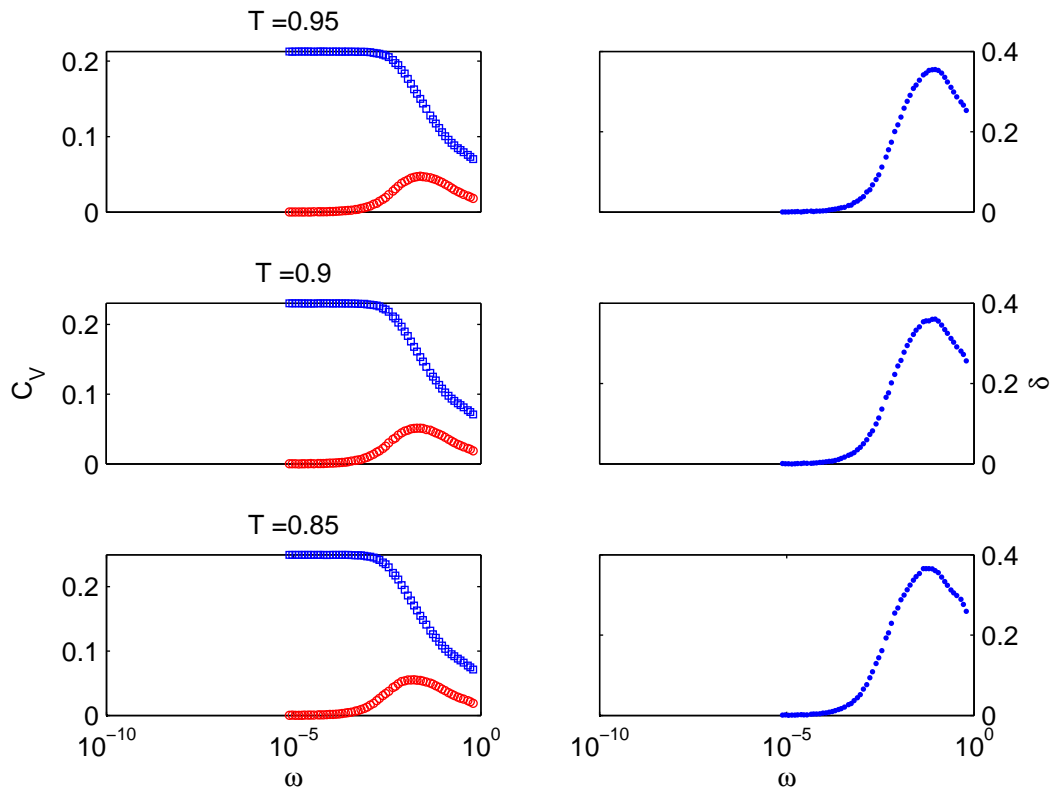


Figure A.6: C_V' (squares), C_V'' (circles), and δ (points) from simulations at the marked temperatures.

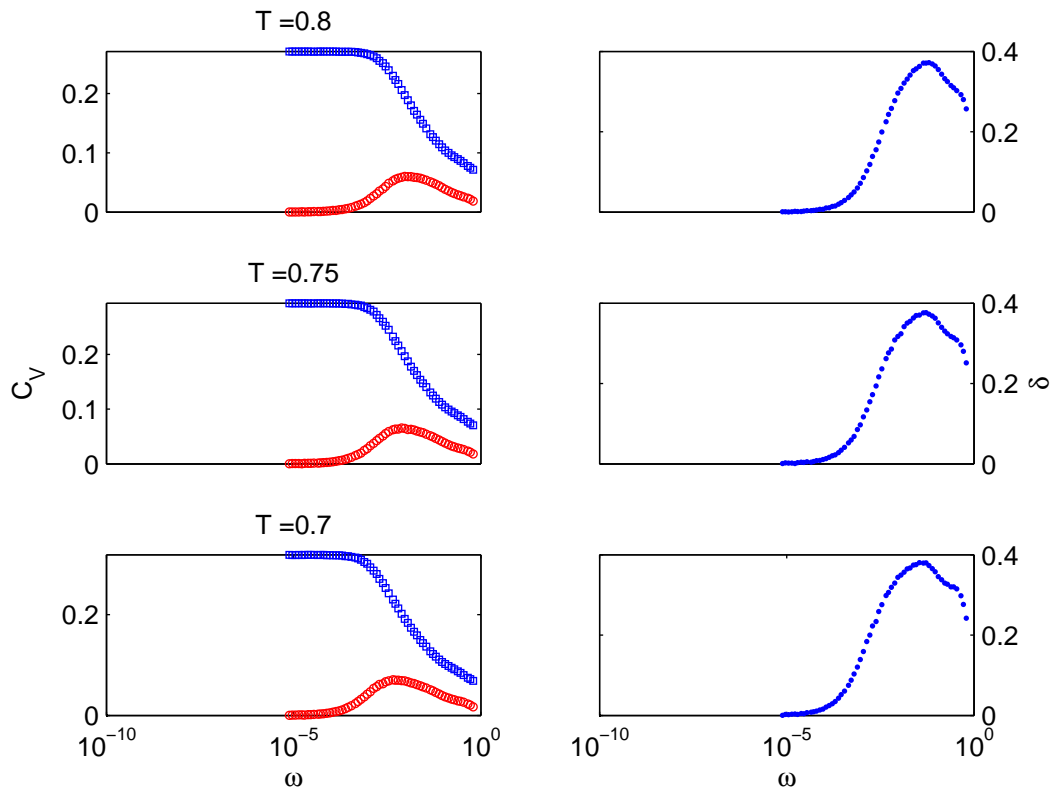


Figure A.7: C_V' (squares), C_V'' (circles), and δ (points) from simulations at the marked temperatures.

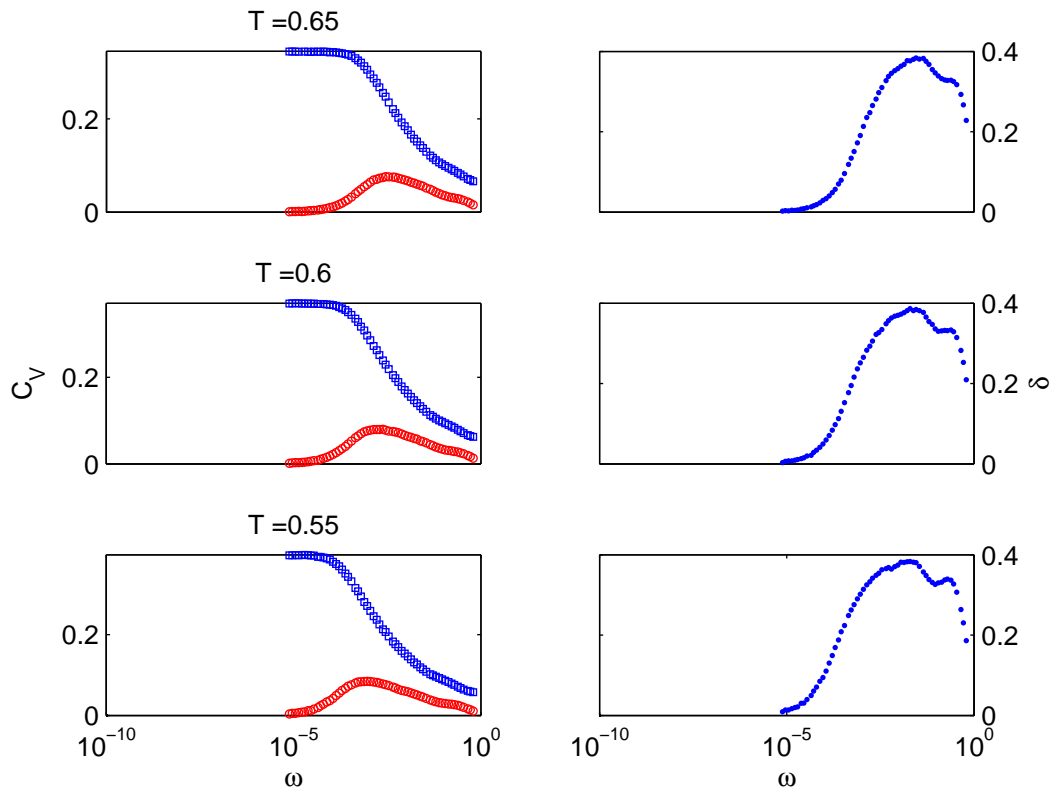


Figure A.8: C_V' (squares), C_V'' (circles), and δ (points) from simulations at the marked temperatures.

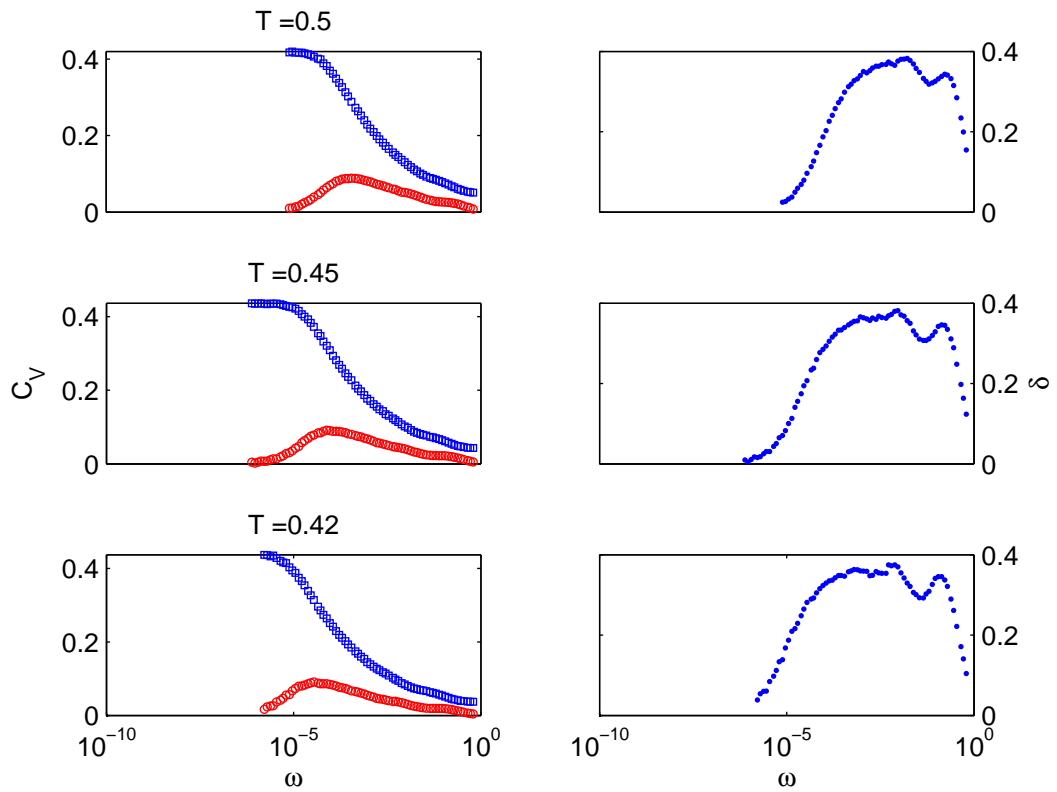


Figure A.9: C_V' (squares), C_V'' (circles), and δ (points) from simulations at the marked temperatures.

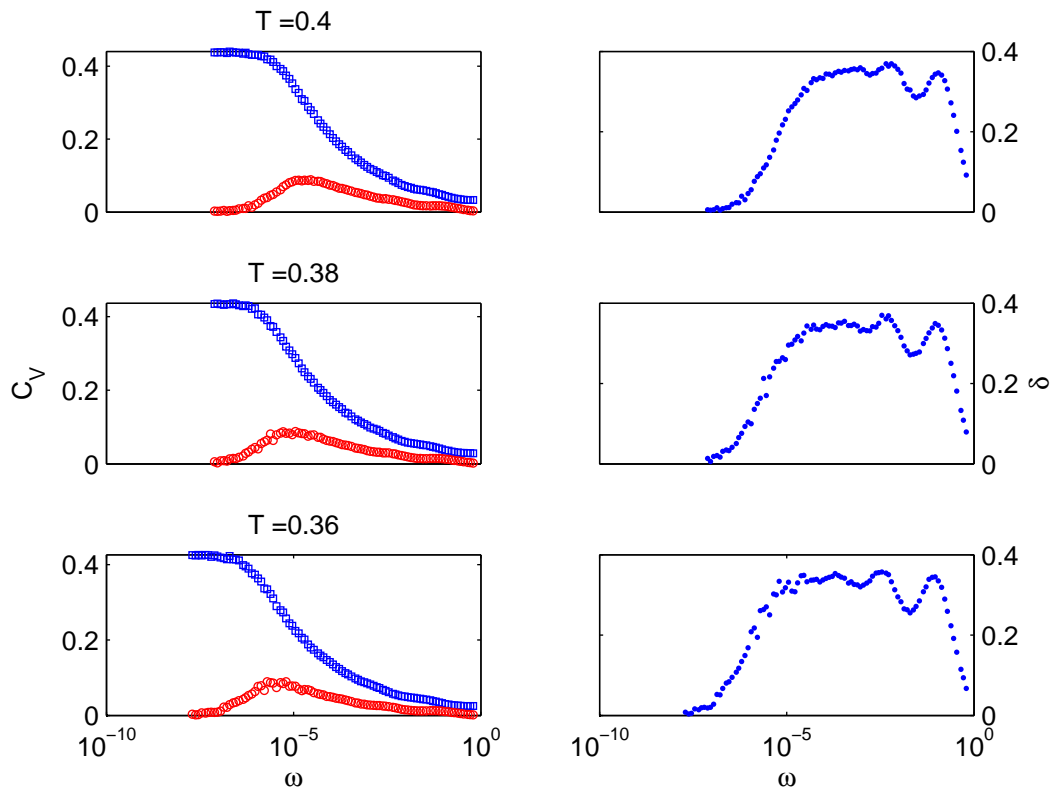


Figure A.10: C_V' (squares), C_V'' (circles), and δ (points) from simulations at the marked temperatures.

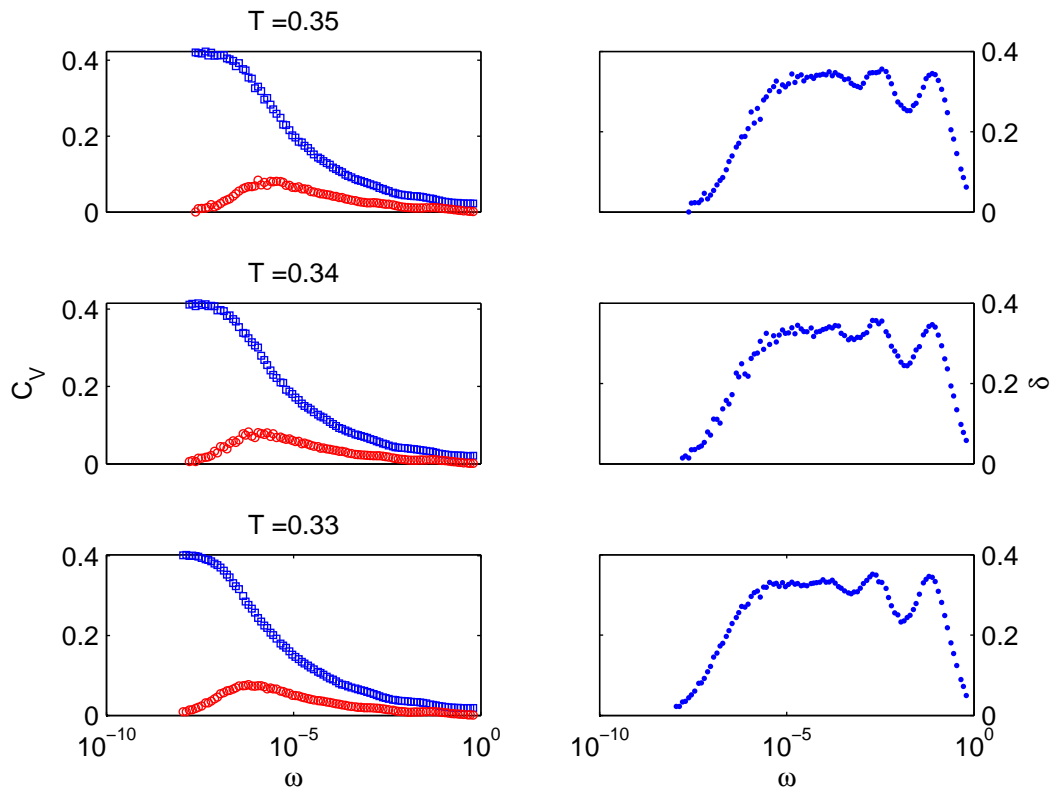


Figure A.11: C_V' (squares), C_V'' (circles), and δ (points) from simulations at the marked temperatures.

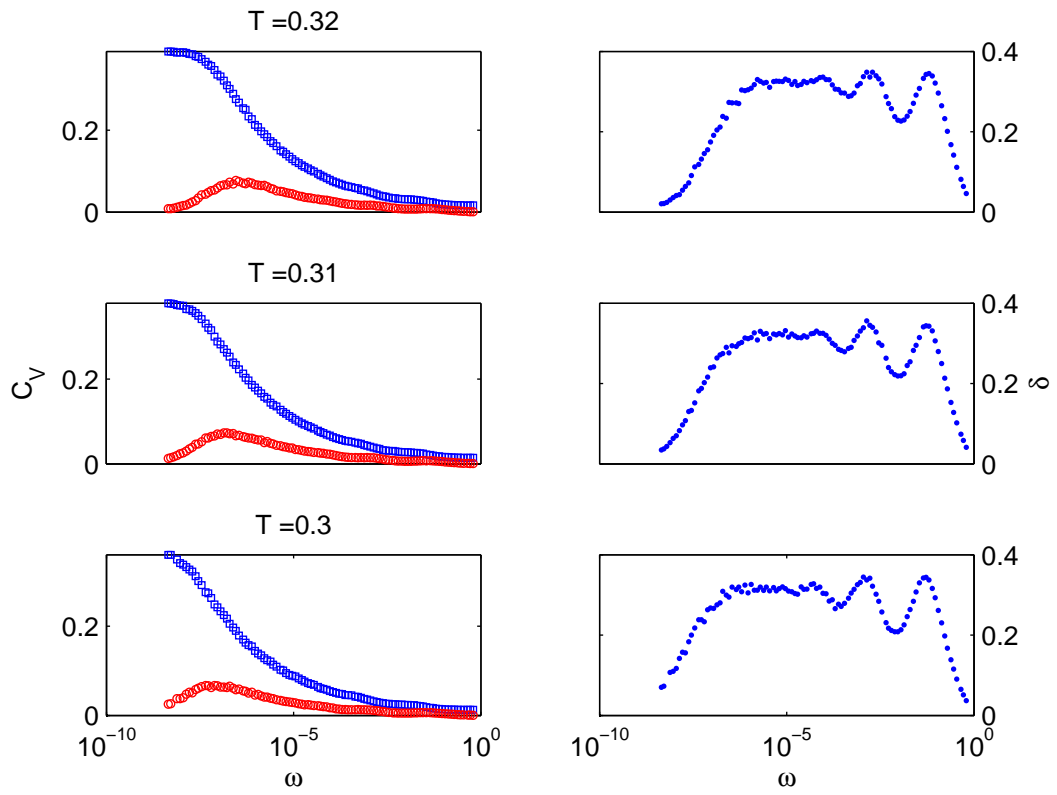


Figure A.12: C'_V (squares), C''_V (circles), and δ (points) from simulations at the marked temperatures.

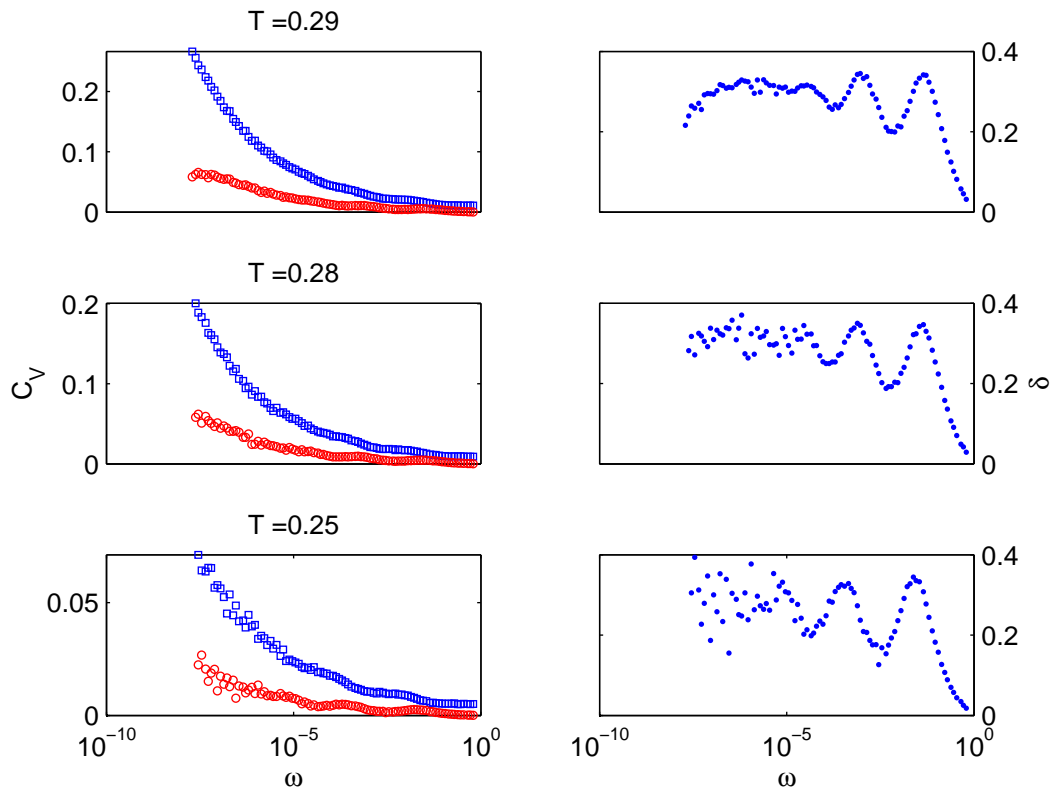


Figure A.13: C_V' (squares), C_V'' (circles), and δ (points) from simulations at the marked temperatures.

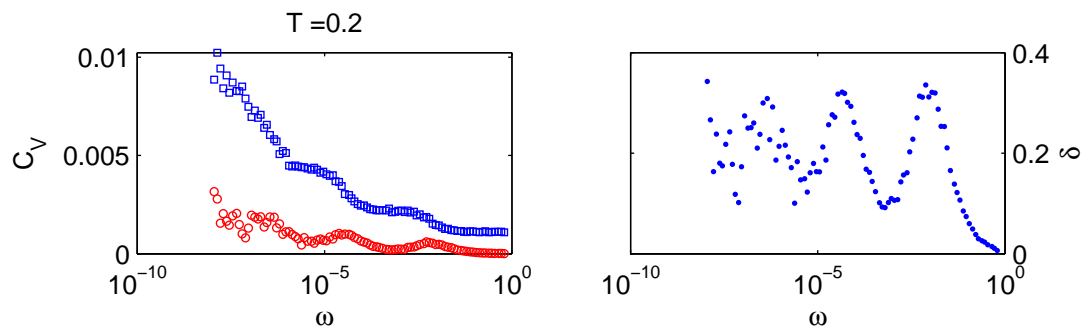


Figure A.14: C_V' (squares), C_V'' (circles), and δ (points) from simulations at the marked temperature.

Bibliography

- [1] David Aldous and Persi Diaconis. The asymmetric One-Dimensional constrained Ising model: Rigorous results. *Journal of Statistical Physics*, 107(5):945–975, June 2002.
- [2] F. Alvarez, A. Alegria, and J. Colmenero. Relationship between the time-domain Kohlrausch-Williams-Watts and frequency-domain Havriliak-Negami relaxation functions. *Physical Review B*, 44(14):7306, October 1991.
- [3] Richard C. Aster, Brian Borchers, and Clifford H. Thurber. *Parameter estimation and inverse problems*. Elsevier Academic Press, Burlington, MA, 2005.
- [4] R. Bergman. General susceptibility functions for relaxations in disordered systems. *Journal of Applied Physics*, 88(3):1356–1365, 2000.
- [5] Norman O. Birge and Sidney R. Nagel. Specific-Heat spectroscopy of the glass transition. *Physical Review Letters*, 54(25):2674, June 1985.
- [6] Jonathan R. Brown, John D. McCoy, and Douglas B. Adolf. Driven simulations of the dynamic heat capacity. *The Journal of Chemical Physics*, 131(10):104507, 2009.
- [7] Herbert B. Callen and Theodore A. Welton. Irreversibility and generalized noise. *Physical Review*, 83(1):34, July 1951.

- [8] N. Cancrini, F. Martinelli, C. Roberto, and C. Toninelli. Kinetically constrained spin models. *Probability Theory and Related Fields*, 140(3):459–504, March 2008.
- [9] D. Chakrabarti and B. Bagchi. Frequency dependent heat capacity within a kinetic model of glassy dynamics. *The Journal of Chemical Physics*, 122:014501, 2004.
- [10] T Christensen. The frequency dependence of the specific heat at the glass transition. *Journal de Physique Colloques*, 46:C8–635–C8–637, 1985.
- [11] Kenneth S. Cole and Robert H. Cole. Dispersion and absorption in dielectrics i. alternating current characteristics. *The Journal of Chemical Physics*, 9(4):341–351, April 1941.
- [12] D.W. Davidson and R.H. Cole. Dielectric relaxation in glycerol, propylene glycol, and n-Propanol. *The Journal of Chemical Physics*, 19:1484–1490, 1951.
- [13] S. Eisinger and J. Jckle. Analytical approximations for the hierarchically constrained kinetic Ising chain. *Journal of Statistical Physics*, 73(3):643–670, November 1993.
- [14] M. R. Evans. Anomalous coarsening and glassy dynamics. *Journal of Physics: Condensed Matter*, 14(7):1397–1422, 2002.
- [15] John D. Ferry. *Viscoelastic Properties of Polymers*. John Wiley & Sons, New York, 3rd edition, 1980.

- [16] Glenn H. Fredrickson and Hans C. Andersen. Kinetic Ising model of the glass transition. *Physical Review Letters*, 53(13):1244, 1984.
- [17] Glenn H. Fredrickson and Hans C. Andersen. Facilitated kinetic Ising models and the glass transition. *The Journal of Chemical Physics*, 83(11):5822–5831, December 1985.
- [18] Raymond M. Fuoss and John G. Kirkwood. Electrical properties of solids. VIII. dipole moments in polyvinyl Chloride-Diphenyl systems. *Journal of the American Chemical Society*, 63(2):385–394, February 1941.
- [19] Juan P. Garrahan and David Chandler. Geometrical explanation and scaling of dynamical heterogeneities in glass forming systems. *Physical Review Letters*, 89(3):035704, July 2002.
- [20] W. Gotze and L. Sjogren. Relaxation processes in supercooled liquids. *Reports on Progress in Physics*, 55(3):241–376, 1992.
- [21] Gary S. Grest and Kurt Kremer. Molecular dynamics simulation for polymers in the presence of a heat bath. *Physical Review A*, 33(5):3628, May 1986.
- [22] Gary S. Grest and Sidney R. Nagel. Frequency-dependent specific heat in a simulation of the glass transition. *Journal of Physical Chemistry*, 91(19):4916–4922, September 1987.
- [23] Charles M. Grinstead and J. Laurie Snell. *Introduction to Probability*. American Mathematical Society, 2nd edition, 2003.

- [24] S. Havriliak and S. Negami. A complex plane representation of dielectric and mechanical relaxation processes in some polymers. *Polymer*, 8:161–210, 1967.
- [25] H. G. E. Hentschel, Valery Ilyin, and Itamar Procaccia. Nonuniversality of the specific heat in glass forming systems. *Physical Review Letters*, 101(26):265701–4, December 2008.
- [26] H. G. E. Hentschel, Valery Ilyin, Itamar Procaccia, and Nurith Schupper. Theory of specific heat in glass-forming systems. *Physical Review E (Statistical, Nonlinear, and Soft Matter Physics)*, 78(6):061504–13, December 2008.
- [27] R. M. Hill and L. A. Dissado. Debye and non-Debye relaxation. *Journal of Physics C: Solid State Physics*, 18(19):3829–3836, 1985.
- [28] Yuji Ike, Yuichi Seshimo, and Seiji Kojima. Complex heat capacity of non-Debye process in glassy glucose and fructose. *Fluid Phase Equilibria*, 256(1-2):123–126, August 2007.
- [29] Ernst Ising. Beitrag zur theorie des ferromagnetismus. *Zeitschrift fr Physik A Hadrons and Nuclei*, 31(1):253–258, February 1925.
- [30] Robert L. Jack, Juan P. Garrahan, and David Chandler. Space-time thermodynamics and subsystem observables in a kinetically constrained model of glassy materials. *The Journal of Chemical Physics*, 125(18):184509–11, November 2006.

- [31] J. Jekle and S. Eisinger. A hierarchically constrained kinetic Ising model. *Zeitschrift fr Physik B Condensed Matter*, 84(1):115–124, February 1991.
- [32] A. Jonscher. A new model of dielectric loss in polymers. *Colloid & Polymer Science*, 253(3):231–250, March 1975.
- [33] Andrew K. Jonscher. Dielectric relaxation in solids. *Journal of Physics D: Applied Physics*, 32(14):R57–R70, 1999.
- [34] Walter Kauzmann. The nature of the glassy state and the behavior of liquids at low temperatures. *Chemical Reviews*, 43(2):219–256, October 1948.
- [35] R. Kohlrausch. Theorie des elektrischen rueckstandes in der leidner flasche. *Annalen der Physik*, 91:56–82,179–213, 1854.
- [36] F. Kremer and A. Schnhals. *Broadband Dielectric Spectroscopy*. Springer, 2003.
- [37] R. De L. Kronig. On the theory of dispersion of x-rays. *Journal of the Optical Society of America*, 12(6):547, November 1926.
- [38] Mai Suan Li, Tran Quang Hung, and Marek Cieplak. Reentrancy and dynamic specific heat of Ising spin glasses. *Journal de Physique I*, 6(2):257, 1996.
- [39] C. P. Lindsey and G. D. Patterson. Detailed comparison of the Williams–Watts and Cole–Davidson functions. *The Journal of Chemical Physics*, 73(7):3348–3357, October 1980.

- [40] John D. McCoy. *Statistical Mechanics of Ideal Gases and Other Simple Materials*. Cafe Press, 2nd edition, December 2008.
- [41] Donald A. McQuarrie. *Statistical Mechanics*. Harper & Row, New York, 1976.
- [42] Mauro Merolle, Juan P. Garrahan, and David Chandler. Spacetime thermodynamics of the glass transition. *Proceedings of the National Academy of Sciences of the United States of America*, 102(31):10837–10840, 2005.
- [43] Johannes K. Nielsen and Jeppe C. Dyre. Fluctuation-dissipation theorem for frequency-dependent specific heat. *Physical Review B*, 54(22):15754, December 1996.
- [44] Jorge Nocedal and Stephen J. Wright. *Numerical Optimization*. Springer, New York, NY, 2006.
- [45] Lars Onsager. Crystal statistics. I. a Two-Dimensional model with an Order-Disorder transition. *Physical Review*, 65(3-4):117, February 1944.
- [46] R. G. Palmer, D. L. Stein, E. Abrahams, and P. W. Anderson. Models of hierarchically constrained dynamics for glassy relaxation. *Physical Review Letters*, 53(10):958, 1984.
- [47] Steven J. Pitts and Hans C. Andersen. A diagrammatic theory of time correlation functions of facilitated kinetic Ising models. *The Journal of Chemical Physics*, 114(3):1101–1114, 2001.

- [48] Steven J. Pitts, Thomas Young, and Hans C. Andersen. Facilitated spin models, mode coupling theory, and ergodic–nonergodic transitions. *The Journal of Chemical Physics*, 113(19):8671–8679, November 2000.
- [49] J. Rault. Origin of the VogelFulcherTammann law in glass-forming materials: the a bifurcation. *Journal of Non-Crystalline Solids*, 271(3):177–217, 2000.
- [50] Y. Saad and M. H Schultz. GMRES: a generalized minimal residual algorithm for solving nonsymmetric linear systems. *SIAM Journal on Scientific and Statistical Computing*, 7(3):856869, 1986.
- [51] P. Scheidler, W. Kob, A. Latz, J. Horbach, and K. Binder. Frequency-dependent specific heat of viscous silica. *Physical Review B*, 63(10):104204, 2001.
- [52] R. J. Sheppard, B. P. Jordan, and E. H. Grant. Least squares analysis of complex data with applications to permittivity measurements. *Journal of Physics D: Applied Physics*, 3(11):1759–1764, 1970.
- [53] Peter Sollich and Martin R. Evans. Glassy Time-Scale divergence and anomalous coarsening in a kinetically constrained spin chain. *Physical Review Letters*, 83(16):3238, October 1999.
- [54] Mark Somoza. Plot of the Kohlrausch-Williams-Watts distribution function. http://en.wikipedia.org/wiki/Image:KWW_dist._function_linear.png, July 2006.

- [55] John S. Toll. Causality and the dispersion relation: Logical foundations. *Physical Review*, 104(6):1760, December 1956.
- [56] Graham Williams and David C. Watts. Non-symmetrical dielectric relaxation behaviour arising from a simple empirical decay function. *Transactions of the Faraday Society*, 66:80–85, 1970.
- [57] C. C. Yu and H. M. Carruzzo. Frequency dependence and equilibration of the specific heat of glass-forming liquids. *Physical Review E*, 69(5):51201, 2004.